KUOPION YLIOPISTON JULKAISUJA C. LUONNONTIETEET JA YMPÄRISTÖTIETEET 199
KUOPIO UNIVERSITY PUBLICATIONS C. NATURAL AND ENVIRONMENTAL SCIENCES 199

TANJA TARVAINEN

Computational Methods for Light Transport in Optical Tomography

Doctoral dissertation

To be presented by permission of the Faculty of Natural and Environmental Sciences
of the University of Kuopio for public examination in Auditorium L22,
Snellmania building, University of Kuopio,
on Friday 29th September 2006, at 12 noon

Department of Physics
University of Kuopio

KUOPION YLIOPISTO
KUOPIO 2006

Distributor:
Kuopio University Library
P.O. Box 1627
FI-70211 KUOPIO
FINLAND
Tel. +358 17 163 430
Fax +358 17 163 410
http://www.uku.fi/kirjasto/julkaisutoiminta/julkmyyn.html

Series editors:
Professor Pertti Pasanen, Ph.D.
Department of Environmental Sciences

Professor Jari Kaipio, Ph.D.
Department of Physics

Author's address:
Department of Physics
University of Kuopio
P.O. Box 1627
FI-70211 KUOPIO
FINLAND
Tel. +358 17 162 349
Fax +358 17 162 373
E-mail: Tanja.Tarvainen@uku.fi

Supervisors:
Docent Ville Kolehmainen, Ph.D.
Department of Physics
University of Kuopio

Docent Marko Vauhkonen, Ph.D.
Department of Physics
University of Kuopio

Professor Jari Kaipio, Ph.D.
Department of Physics
University of Kuopio

Reviewers:
Professor David Boas, Ph.D.
NMR Center, Massachusetts General Hospital
Harvard Medical School
Charlestown, MA, USA

Assistant Professor Oliver Dorn, Ph.D.
Department of Applied Mathematics
University Carlos III de Madrid
Leganes, Spain

Opponent:
Professor Samuli Siltanen, Ph.D.
Department of Mathematics
Tampere University of Technology
Finland

ISBN 951-27-0357-2
ISBN 951-27-0452-8 (PDF)
ISSN 1235-0486

Kopijyvä
Kuopio 2006
Finland

Tarvainen, Tanja. Computational Methods for Light Transport in Optical Tomography. Kuopio University Publications C. Natural and Environmental Sciences 199. 2006. 123 p.
ISBN 951-27-0357-2
ISBN 951-27-0452-8 (PDF)
ISSN 1235-0486

ABSTRACT

Optical tomography is a relatively new imaging modality in which images of the optical properties of the medium are estimated based on measurements of visible or near-infrared light on the surface of the object. The image reconstruction problem in optical tomography is a non-linear ill-posed inverse problem. Thus, even small errors in the measurements or modelling can cause large errors in the reconstructions. Therefore, computationally feasible forward models that describe light transport in the medium accurately are needed.

In this thesis, modelling approaches to the forward problem of optical tomography are developed. Light propagation within the object and in the optic fibres of optical tomography measurements are described through two approaches. Firstly, modelling light propagation in tissues through transport theory is investigated, and secondly, a computational method for calibration of optical tomography measurements is developed.

In the first approach, two new hybrid methods to describe light transport in tissues are proposed. The approaches utilize the radiative transfer equation, which is known to describe light propagation in tissues accurately but is computationally expensive, and the diffusion approximation, which is the most often used forward model in optical tomography but suffers from limitations in situations in which the assumptions of diffusion theory are not valid. The proposed hybrid methods are implemented with the finite element method. The methods are tested with simulations in different situations and the results are compared against the traditional light transport models. The results show that the hybrid methods can be used to describe light transport in various media almost as accurately as the radiative transfer equation and Monte Carlo and with less computation cost than either of the methods. Furthermore, the results show that the hybrid approaches give significantly better results than the diffusion approximation in situations in which the assumptions of the diffusion theory are not valid.

As the second approach, a computational method for calibration of optical tomography measurements is developed. Light attenuation in the optic fibres is modelled by complex valued coupling coefficients. Utilizing the rotation symmetry of source and detector positions in the measurement setup, a calibration model is developed and the coupling coefficients are estimated. The calibration method is tested with simulations and measurements. The results show that the coupling coefficients of the sources and detectors can be estimated with good accuracy. Furthermore, the results show that the method improves the quality of reconstructed images significantly.

AMS Classification: 78A46, 78M10
Universal Decimal Classification: 535.3
National Library of Medicine Classification: WN 206, QT 36
INSPEC Thesaurus: biomedical optical imaging; optical tomography; light propagation; radiative transfer; transport processes; light scattering; biological tissues; finite element analysis; computational physics; calibration; inverse problems

Acknowledgements

This work was carried out in the Department of Physics at the University of Kuopio during the years 2001–2006.

First, I would like to thank my main supervisor Docent Ville Kolehmainen, Ph.D., for his guidance during this work. I would like to express my deepest gratitude to my supervisor Professor Jari Kaipio, Ph.D., for giving me the opportunity to work in his excellent research group at the Department of Physics and for his ideas, guidance, and encouragement for this research. Especially, I would like to thank my supervisor Docent Marko Vauhkonen, Ph.D., for his excellent guidance and encouragement.

I wish to thank the official reviewers Professor David Boas, Ph.D., and Assistant Professor Oliver Dorn, Ph.D., for their valuable suggestions and comments for the thesis.

I wish to thank the staff of the Department of Physics for their support and for the pleasant working atmosphere. Many thanks to Perttu Ranta-aho, M.Sc., for the assistance with computers and to my former roommates Päivi Vauhkonen, Ph.D., and Tero Karjalainen, M.Sc., for their encouragement. Thanks to my co-author Antti Vanne, M.Sc., for providing a computer cluster environment and algorithms, and Eeva Boman, M.Sc., for many scientific and non-scientific discussions. I especially wish to thank Anna Ruuskanen, M.Sc., for her friendship and encouragement. I also wish to thank all my teachers, especially Professor Pasi Karjalainen, Ph.D., and Docent Jouko Tervo, Ph.D.

I would like to thank Professor Simon Arridge, Ph.D., from the University College London (UCL) for welcoming me to visit UCL and for his advice. Thanks also to my other co-authors Adam Gibson, Ph.D., for providing the real data, and Martin Schweiger, Ph.D. I wish to thank Jenni Heino, Ph.D., Ilkka Nissilä, Ph.D., Juha Heiskala, M.Sc., and Tommi Noponen, M.Sc., from the Helsinki University of Technology for the collaboration and for many valuable discussions. I also wish to thank Professor Markku Kataja, Ph.D., Markko Myllys, Ph.D., and Esa Rehn, M.Sc., from the University of Jyväskylä for the collaboration.

Finally, I would like to thank my parents Marja-Liisa and Erkki for their constant love and support and my sister Katja for her encouragement. I wish to thank my grandparents Meeri and Pertti for their encouragement. I thank my parents-in-law Helvi and Taito for their support. I wish to thank my friend Sari for her encouragement and friendship, and I thank Pirjo, Heli, and Marianne for their friendship. Especially, I would like to thank my husband Mika for all his love and support. I dedicate this thesis to Mika with all my love.

This thesis was supported by the National Technology Agency of Finland (TEKES), the Academy of Finland, the Jenny and Antti Wihuri Foundation, and the Finnish Cultural Foundation of Northern Savo.

Kuopio, 5th September 2006

Tanja Tarvainen

Abbreviations

2D	Two-dimensional
3D	Three-dimensional
CSF	Cerebrospinal fluid
DA	Diffusion approximation
FE	Finite element
FEM	Finite element method
MONSTIR	The multichannel optoelectronic near-infrared system for time-resolved image reconstruction
OT	Optical tomography
RTE	Radiative transfer equation
TOAST	Time-resolved optical absorption and scattering tomography
TPSF	Temporal point spread function

Notations

i	Imaginary unit
n	Dimension
$\mathbb{R}^n$	n-dimensional real space
S^{n-1}	Angular space
r	Position vector
$\hat{s}$	Unit vector in the direction of interest
$\hat{n}$	Outward unit normal
$\|\cdot\|$	Euclidean norm
$\|\cdot\|$	Absolute value
$\arg(\cdot)$	Phase angle
$\mathrm{Im}(\cdot)$	Imaginary part of a complex valued function
$\mathrm{Re}(\cdot)$	Real part of a complex valued function
c	Speed of light in the medium
t	Time
ω	Angular modulation frequency of the input signal
μ_a	Absorption coefficient
μ_s	Scattering coefficient
μ_s'	Reduced scattering coefficient
κ	Diffusion coefficient
g	Scattering shape parameter
$\Theta(\hat{s} \cdot \hat{s}')$	Scattering phase function
$\phi(r, \hat{s})$	Radiance
$\Phi(r)$	Photon density
$J(r)$	Photon current
$\Gamma(r)$	Exitance
γ_n	Dimension-dependent constant ($\gamma_2 = 1/\pi$, $\gamma_3 = 1/4$)
n_{in}	Refractive index of the medium

R	Reflection coefficient
A	Reflection parameter
Ω	Domain
$\partial\Omega$	Boundary of the domain
Ω_{rte}	RTE sub-domain
$\partial\Omega_{\text{rte}}$	Boundary of the RTE sub-domain
Ω_{da}	DA sub-domain
$\partial\Omega_{\text{da}}$	Boundary of the DA sub-domain
Γ	Interface between sub-domains
$v(r,\hat{s})$	Test function for the radiance
$\Psi(r)$	Test function for the photon density
N_n	Number of spatial nodes in the RTE discretization
N_a	Number of angular directions in the RTE discretization
N	Number of spatial nodes in the DA discretization
α	Radiance vector in the RTE discretization
a	Photon density vector in the DA discretization
$\psi(r)$	Spatial basis function for the radiance
$\psi(\hat{s})$	Angular basis function for the radiance
$\varphi(r)$	Basis function for the photon density
m	Number of sources and detectors
ε_j	Source
ζ_k	Detector
$\hat{s}_j$	Source coupling coefficient
s_j	Source amplitude loss coefficient
σ_j	Source phase shift
$\hat{d}_k$	Detector coupling coefficient
d_k	Detector amplitude loss coefficient
δ_k	Detector phase shift

Chapter I

Introduction

Tomographic images of the body are a valuable clinical diagnostic tool. Although efficient medical imaging modalities, such as x-ray computed tomography and magnetic resonance imaging, exist, new imaging systems are required. Especially noninvasive, relatively inexpensive, and portable imaging systems that could be used for ambulatory diagnoses and continuous bedside monitoring need to be developed. In addition, functional imaging modalities which provide information about physiologically relevant parameters, such as tissue oxygenation level, are required. Optical tomography (OT) is a potential application to meet these criteria. Furthermore, in addition to the biomedical applications, there has been growing interest towards the use of optical methods in industry [132, 239].

Optical tomography is a relatively new imaging modality in which images of the optical properties of the medium, which in most applications is biological tissue, are estimated based on measurements of visible or near-infrared light on the surface of the object. In the experimental setup, a set of light sources and detectors is attached on the boundary of the object [99]. Light from a near-infrared laser source is guided into the object using one of the source fibres and the amount of transmitted light is measured using light sensitive detectors. This measurement process is repeated for all source locations. Based on the measurements, absorption and scattering distributions within the object are reconstructed or other physiological quantities, such as amount of oxy-haemoglobin and deoxy-haemoglobin and water content, are estimated.

Optical tomography has many promising applications mainly in the field of medical imaging [89]. The applications of OT are based on different absorption and scattering properties of light within the target medium. There are a few issues that favour optical tomography as an imaging modality. Firstly, the optical methods can provide information about oxygenation and blood volume in tissues. Secondly, the measurement procedure is noninvasive and the radiation is non-ionizing, and therefore the technique is patient friendly and safe. Thirdly, the instrumentation is relatively inexpensive and easily portable. In addition, OT can provide functional information about the target tissue. A limiting factor in OT is the fast attenuation of light within the medium which results into restricted imaging of large target volumes. The potential medical applications of OT in-

clude detection and classification of breast cancer [57, 63, 70, 77, 187, 217, 242], functional brain studies [34, 42, 56, 58, 64, 69, 78, 120], and imaging newborn infant head [102, 103, 90]. In addition, imaging other tissues, such as bones and joints, have been investigated [114, 116, 198, 241]. Possible applications of OT in industry include process tomography where noninvasive measurement techniques to monitor both temporal and spatial behaviour of industrial processes are needed [132].

The image reconstruction problem in optical tomography is to estimate the optical properties within the object when the amount of guided light and the measured data on the boundary of the object are given [11, 14]. The image reconstruction problem in OT is a non-linear ill-posed inverse problem. Thus, even small errors in the measurements or modelling can cause large errors in the reconstructions. To overcome the difficulties due to the ill-posed nature of the problem, regularization techniques need to be used [11, 145]. Furthermore, computationally feasible forward models that describe light propagation within the medium accurately are needed.

Light propagation in biological materia is usually described through transport theory. The transport theory can be modelled through stochastic methods, such as Monte Carlo, and through deterministic methods which are based on describing light transport with partial differential equations [14]. A generally accepted model for light propagation in medium with scattering particles is the radiative transfer equation (RTE). However, in many cases, the RTE is computationally too expensive to be used in practical applications and approximate models are applied. In highly scattering medium, the transport equation is approximated by diffusion theory. The governing equation is the diffusion approximation (DA) to the RTE. Most of the tissue types are scattering dominated, and the DA can be regarded as a good model to describe light propagation within them. However, its approximations are not valid within low-scattering medium, such as the cerebrospinal fluid, and close to the highly collimated light sources that are often used in OT. To overcome the limitations of the diffusion theory close to the sources and within low-scattering and non-scattering regions, different hybrid methods and approximative models in which the DA is combined, for example, with Monte Carlo simulation or radiosity model have been developed [5, 13, 30, 98, 139, 236].

The analytical solutions of the RTE and the DA are often restricted to certain specific geometries [12, 53, 160], and therefore their exploitability in OT is limited. Therefore, the RTE and the DA are usually solved with numerical methods. The most often applied numerical methods in OT are the finite difference method and the finite element method (FEM). The FEM is generally regarded as more flexible in implementing different boundary conditions and in handling complex geometries, and therefore it is most often chosen as the method for solving the equations describing light transport in tissues.

In addition to target tissue, the light propagation in OT measurements is also affected by the optic fibres and by the coupling effects between the object and the optic fibres. These coupling effects cause unknown amplitude losses and phase delays to the measurement signal. Unless these losses are efficiently calibrated or

modelled, they can result in severe artefacts in the reconstructed images. Typically, the errors in optode modelling appear as absorption and scattering perturbations adjoint to the optodes. One way to compensate for the optode losses is to use difference imaging. Difference imaging is known to produce images with few artefacts. However, it can not be used when absolute baseline optical properties are required or when a reference measurement is not available. Therefore, in order to obtain absolute images, an efficient calibration protocol is needed. Methods for calibration of source and detector optode losses using calibration tools or other instrumentation based methods have been developed [115, 164, 169, 199]. However, accurate calibration of source and detector losses is difficult to implement on instrumentation level. Therefore, other model based methods have been investigated and developed [43, 125, 158, 165, 172, 221].

The aims and contents of the thesis

The aim of this thesis is to develop modelling approaches to the forward problem of OT. Light propagation within the object and in the optic fibres of OT measurements are described through two approaches. Firstly, modelling light propagation in tissues through transport theory is investigated. The purpose is to develop new light transport models which describe light propagation in tissues accurately and which are computationally less demanding than the RTE. In the thesis, FE-solution for the RTE is developed and the performance of the FE-solutions of the RTE and DA are tested. In addition, two new hybrid methods, namely the hybrid model and the coupled RTE–DA model, to describe light propagation in tissues are proposed. The hybrid methods are implemented with the FEM. Secondly, a computational calibration method for calibration of OT measurements is developed. Light attenuation in the optic fibres is modelled by complex valued coupling coefficients. Utilizing the rotation symmetry of source and detector positions in the measurement setup, a calibration model is developed and the coupling coefficients are estimated.

Some of the results of this thesis have already been published in [224, 225, 226, 227, 228, 234]. The aim of the thesis is not only to summarize the results of the publications but also to give a more detailed presentation of the methods and their theoretical background. The thesis contains also some unpublished results.

The thesis is divided into seven chapters. In Chapter 2, a short review of OT is given. The optical properties of tissue, the experimental devices used in OT, and the main applications of OT and their recent developments are reviewed. In addition, the modelling and reconstruction aspects of OT are reviewed. The OT forward problem is described, and the OT inverse problem and some special approaches in image reconstruction are discussed.

In Chapter 3, modelling of light propagation in tissues though transport theory is discussed. The radiative transfer equation is reviewed, and the diffusion approximation and its derivation are reviewed. In addition, some hybrid methods which have been developed to describe light propagation in tissues are reviewed. Two new hybrid methods, the hybrid model and the coupled RTE–DA model, are proposed for the forward problem of OT. The proposed hybrid methods utilize both

the RTE and the DA. In the hybrid model, light propagation is modelled with the RTE close to the light sources and the DA is used elsewhere in the domain. The hybrid model can be utilized in highly scattering medium and it corrects the inaccuracy of the diffusion theory close to the sources. In the coupled RTE–DA model, light propagation is modelled with the RTE in sub-domains in which the assumptions of the DA are not valid and the DA is used elsewhere in the domain. Compared to the hybrid model, the coupled RTE–DA model can also be used in other situations in which the assumptions of the DA are not valid such as within low-scattering regions and near the domain boundary.

In Chapter 4, the finite element implementations of the RTE, the DA, and the coupled RTE–DA model are given. In addition, Monte Carlo is presented as a reference method.

In Chapter 5, light propagation is simulated using the different light transport models described in Chapter 3. The RTE and the DA are solved with the FEM in different domains with various optical properties. Furthermore, the proposed hybrid model and the coupled RTE–DA model are tested with simulations in different situations.

In Chapter 6, a computational method for calibration of the frequency-domain OT measurements is proposed. The model of the calibration scheme is based on the rotation symmetry of source and detector positions in the measurement setup. The relative amplitude losses and phase shifts at the optic fibres are modelled by complex valued coupling coefficients which can be estimated when data from a homogeneous and isotropic object is given. Furthermore, an extended DA model which includes source and detector coupling coefficients is introduced. The calibration method is tested with simulations and measurements.

Finally, the overall conclusions of the thesis are given in Chapter 7.

CHAPTER II

Optical tomography

In this chapter, the basics of optical tomography (OT) are briefly reviewed. In Section 2.1, optical properties of tissue, experimental devices, and the applications of OT are reviewed. In Section 2.2, modelling and image reconstruction issues are briefly discussed. The purpose of this chapter is to give a context for the modelling aspects discussed in remaining chapters. Therefore, many of the issues are only briefly discussed. For more thorough review of OT and its latest developments, see e.g. the reviews [11, 38, 89, 99, 212].

2.1 On optical tomography

2.1.1 Tissue optical properties

In optical tomography, images of the optical properties of the medium are reconstructed based on measurements of near-infrared light on the boundary of the object. Light propagation in the medium is affected by absorption and scattering. In an absorption event, energy is transfered from the radiation to the surrounding medium. The quantity which describes absorption in the medium is the absorption coefficient μ_a which is the number of absorption events per unit length. Scattering is a phenomenon in which the direction of the radiation changes within the medium. The new radiation direction depends on the properties of the scatterer and the incoming direction of the radiation. The scattering properties of the medium are described by two quantities which are the scattering coefficient and the scattering phase function. The scattering coefficient μ_s describes the probability of a particle to scatter after proceeding a certain distance. The scattering phase function $\Theta(\hat{s} \cdot \hat{s}')$, where $\hat{s}'$ and $\hat{s}$ are the radiation directions before and after scattering event, describes the probability of a particle to scatter in a given direction by a particular scatterer. A third quantity which affects light propagation within the medium is the refractive index n_{in} which is the ratio between the speed of light in the vacuum and in the medium. Changes in the refractive index between different materia can cause reflection and refraction effects at the interfaces between the materia. In most of the OT applications, the refractive index is assumed to be constant within the medium.

In most of the tissues, light propagation is dominated by scattering. As a

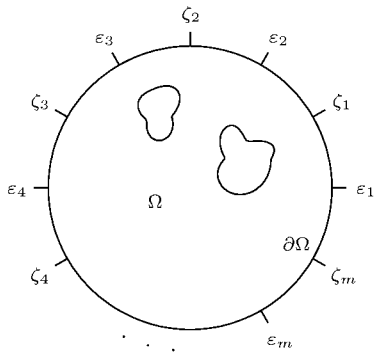

Figure 2.1: Illustration of the OT measurement setup. The sources ε_j and detectors ζ_k are attached on the boundary $\partial\Omega$ of the object Ω.

results of this, after traveling the length of a few millimeters, light propagation in tissues can be described as a diffusive process. Different tissue types have distinct scattering properties, and therefore this distinction can be imaged [38]. Although, in biological materia the scattering coefficient is generally larger than the absorption coefficient, most of the interesting information is related to the absorption. Especially the absorption spectra of haemoglobin, water, and lipids are of interest [38]. Reviews of the optical properties of different tissues can be found for example in [55, 178].

2.1.2 Experimental techniques

The experimental devices used in optical tomography can be divided into three classes which are the continuous wave systems, the frequency-domain systems, and the time-domain systems. In all of the systems, the basic idea of the data acquisition is the same. In the experimental setup, a set of light sources and detectors is attached on the boundary $\partial\Omega$ of the object Ω. A two-dimensional illustration of a typical OT measurement situation is shown in Figure 2.1, where m sources are attached at source locations ε_j, $j = 1, \ldots, m$ and m detectors are attached at detector locations ζ_k, $k = 1, \ldots, m$. First, light from a near-infrared laser source is guided into the object using one of the sources at ε_j and the amount of transmitted light is measured using light sensitive detectors at ζ_k, $k = 1, \ldots, m$. Then, this measurement process is repeated for all m source locations.

Continuous wave systems

The continuous wave instruments use constant intensity light sources and measure the intensity $\Gamma(\omega = 0)$ of the transmitted light at the measurement sites (DC-intensity). Many continuous wave systems have been developed for optical tomography [59, 182, 201, 202, 214]. However, some disadvantages are known to

be related with continuous wave imaging. Firstly, intensity measurements are sensitive to the optical properties of tissues close to the surface and to the coupling effects on the surface rather than the optical properties deeper within the tissue [89]. Secondly, the absorption and scattering effects can not be distinguished based on the intensity measurements only [16]. Therefore, the continuous wave measurements are usually used for difference imaging where the reconstruction is formed using the difference between the measured data and a data from a reference measurement. The strength of the continuous wave imaging devices is their speed in data acquisition which enables fast temporal resolution for imaging [182, 203, 214].

Two other measurement systems, i.e. frequency-domain and time-domain systems, are discussed next. Both of these measurement systems are able to produce more information than just one data type, and thus both absorption and scattering distributions can be distinguished from absolute measurements without using a reference measurement.

Frequency-domain systems

In the frequency-domain systems, a source which is amplitude modulated at high frequency (a few hundred MHz) is used and the amplitude attenuation and phase shift of the transmitted signal are measured. A diagram of the temporal behaviour of the transmitted light $\Gamma(\omega)$ during a frequency-domain measurement is illustrated on the top row of Figure 2.2. Figure shows an intensity modulated input signal in the left image and an attenuated and phase shifted measurement signal in the right image. Different frequency-domain systems have been developed and evaluated [52, 63, 78, 85, 164, 169, 170, 186]. Frequency-domain instruments are relatively inexpensive, easy to develop and use, and they can provide a relatively fast temporal sampling [89].

The data types that are obtained from a frequency-domain measurement are the amplitude $|\Gamma(\omega)|$ and phase shift $\arg(\Gamma(\omega))$ of a complex valued measurement $\Gamma(\omega)$. In many cases, the reconstructions are carried out using the logarithm of amplitude $\log|\Gamma(\omega)|$ and phase shift data. Alternatively, the real and imaginary parts of the measurement, $\mathrm{Re}(\Gamma(\omega))$ and $\mathrm{Im}(\Gamma(\omega))$, can also be used.

Time-domain systems

In the time-domain (time-resolved) systems, a short duration (a few picoseconds) light pulse is given as an input and the temporal distribution $\Gamma(t)$ of the transmitted photons is measured [89, 99, 199]. This temporal distribution is known as the temporal point spread function (TPSF) [68, 176]. A diagram of the temporal behaviour of the transmitted light signal $\Gamma(t)$ during a time-domain measurement is illustrated on the bottom row of Figure 2.2. Figure shows the input light pulse in the left image and the transmitted TPSF in the right image. Various time-domain systems have been developed and evaluated [32, 75, 95, 100, 171, 183, 199]. In time-domain systems, measuring times are usually longer than in the frequency-domain systems. On the other hand, the time-domain systems offer highly sensitive measurements even across large thicknesses of tissue [89].

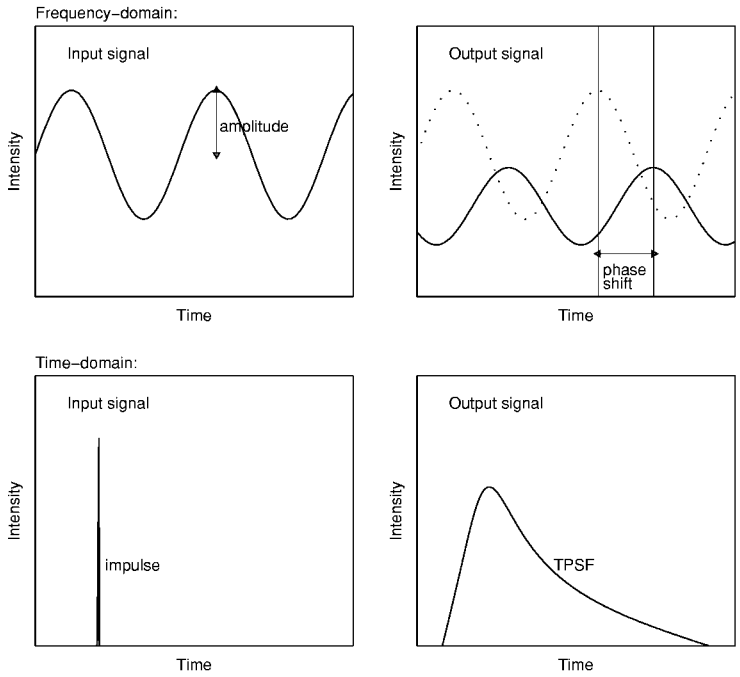

Figure 2.2: Diagram of the temporal behaviour of transmitted light during an optical tomography measurement. On the top row there are the input (left image) and output (right image) signals of the frequency-domain measurement, and on the bottom row there are the input (left image) and output (right image) signals of the time-domain measurement.

Although the TPSF could be used for reconstruction directly, commonly a few data types are derived from $\Gamma(t)$. Some examples of these data types are [205, 206]

$$\text{integrated intensity}: \quad E = \int_0^\infty \Gamma(t)\mathrm{d}t \tag{2.1}$$

$$\text{time}-\text{gated intensity}: \quad \bar{E}(T) = \int_0^T \Gamma(t)\mathrm{d}t \tag{2.2}$$

$$n\text{th temporal moment}: \quad \langle t^n \rangle = E^{-1} \int_0^\infty t^n \Gamma(t)\mathrm{d}t \tag{2.3}$$

$$n\text{th central moment}: \quad c_n = E^{-1} \int_0^\infty (t - \langle t \rangle)^n \, \Gamma(t)\mathrm{d}t \tag{2.4}$$

$$\text{normalized Laplace transform}: \quad L(s) = E^{-1} \int_0^\infty e^{-st} \Gamma(t)\mathrm{d}t \tag{2.5}$$

$$\text{Mellin} - \text{Laplace transform}: \qquad ML_n(s) = E^{-1} \int_0^\infty t^n e^{-st} \Gamma(t) \mathrm{d}t. \quad (2.6)$$

For example in [199], the mean flight time $\langle t \rangle$, variance c_2, and Laplace transform $L(s = 0.005\,\mathrm{ps}^{-1})$ were chosen for the experiments.

RELATIONS BETWEEN THE APPROACHES

Some relations are valid between the data types measured with different modalities. The most important relation is that the frequency-domain and time-domain measurements are related through the Fourier transform

$$\Gamma(\omega) = \int_0^\infty \Gamma(t) e^{-\mathrm{i}\omega t} \mathrm{d}t. \quad (2.7)$$

In fact, in some cases the time-domain measurement system is used for measurements and the frequency-domain data at some frequency obtained with the Fourier transform is used for reconstructions. This approach is also chosen in this study for the measurements and reconstructions of Chapter 6 in which a computational method for calibration of the frequency-domain OT measurements is proposed. It should also be noted that the measured DC-intensity corresponds to the integrated intensity defined in equation (2.1), that is $\Gamma(\omega = 0) = E$. The time-domain and frequency-domain parameters and their dependencies are discussed more detailed for example in [12].

The issues of sensitivity of different measurement schemes and selection of measurement data types suitable for image reconstruction have been under a thorough investigation. These issues are discussed for example in [10, 18, 204, 205, 206]. However, the performance of different measurement systems has not been investigated apart from few recent studies. In [168], the performance of the time-domain and frequency-domain devices was investigated by comparing both the quality of the amplitude and phase data and the performance in image reconstruction. In addition, a protocol for the performance assessment of photon migration instruments was proposed and eight time-domain and continuous wave systems were evaluated according to this protocol in [184].

2.1.3 Applications

During the last decade, optical tomography has quickly developed from an experimental laboratory technique into an imaging modality which is clinically tested for a variety of applications. Nowadays OT is under constant development and new experimental techniques as well as modelling approaches are constantly elaborated and evaluated. Methods are tested with fantom and small animal experiments in laboratories as well as with human patients in clinics.

There are many issues that favour optical tomography as an imaging modality. Firstly, the optical methods can produce information about oxygenation and blood volume in tissues, and thus they can differentiate between soft tissues. In addition, it is possible to provide functional information about the target tissue with OT. Secondly, the measurement procedure is noninvasive and the radiation

is non-ionizing, and therefore the technique is patient friendly and safe. Thirdly, the instrumentation is relatively inexpensive and easily portable which makes it possible to use the technique e.g. for ambulatory diagnoses and continuous bedside monitoring. A limiting factor in OT is the fast attenuation of light in the medium. This results into restricted imaging of large target volumes. More information about OT and its applications can be found for example from a recent review [89].

Breast imaging

Tumours are associated with increased vascularization, and therefore they have different absorption properties from the surrounding healthy tissue [38, 89]. Thus, optical tomography provides a natural method to localize tumours. In addition, pathological conditions are predicted to appear dissimilarities in OT which indicates that the method can also be applied in classification of different types of conditions [243]. The disadvantage of OT is that its spatial resolution is relatively poor compared with the x-ray mammography which is the most common method for breast imaging. However, OT has some advantages over x-ray tomography: firstly, the radiation is non-ionizing and therefore no doze is caused to the patient, and secondly, OT does not require compression of the breast which is uncomfortable and in many cases also painful to the patient. In addition, unlike in x-ray tomography, the sensitivity of OT for younger women is as good as for older women.

In OT, a number of approaches for breast imaging have been evaluated. Many of the clinical studies have been performed using instruments which compress the breast [74, 85, 95, 183]. This reduces attenuation of the transmitted light and ensures that the imaging geometry is well known. The disadvantage of the compression technique is that, although the compression is more gentle than in x-ray mammography, it causes changes in the optical properties of the breast tissue [89, 126]. The compressed breast geometry has been used to investigate bulk optical properties of the breast tissue [74]. The same geometry has also been used to scan through the breast to produce projection images [93, 223] and to determine tumour optical properties [80, 94, 215]. The compressed measurement geometry has also been applied to more refined approach in which three-dimensional (3D) images of the optical properties of the whole breast tissue volume have been reconstructed [63, 70]. The method has been used to monitor changes in tumour during neoadjuvant chemotherapy [57].

An ideal technique for generating 3D images of the breast is to surround the breast with sources and detectors [164, 186, 202, 242]. The disadvantage of the approach is that the length for light to travel through the breast is longer and the detected light intensities are lower than in the compressed geometry. The method has been applied to determine the bulk optical properties of the breast tissue [163, 218, 219]. Further, full 3D reconstructions of the breast optical properties of breast cancer patients have been obtained [187, 217, 242]. The method has also been used to monitor changes in the optical properties of the breast tissue after a laser surgery [101]. Breast measurements have also been performed with a hemispherical tank which is filled with tissue matching fluid with the sources and

detectors located on the boundaries of the tank [59, 244]. The breast tank which is filled with fluid has some benefits over the other approaches, for example, cups can accommodate a large range of breast sizes, the coupling of the sources and detectors is constant and independent of the subject, and the external geometry of the imaging volume is known exactly. The method has been tested with healthy human subjects [244] and with human patients with lesions [77].

Imaging brain function

Optical methods have been widely studied in imaging functional brain activities both with adults and with neonates. Optical imaging of brain function is based on the fact that the absorption and scattering properties for near-infrared light provide information about the brain activity. Although OT suffers from the low spatial resolution it has some advantages over the other brain imaging techniques of which the most often used is the functional magnetic resonance imaging. Firstly, OT can be used to distinguish between oxy-haemoglobin and deoxy-haemoglobin [44]. Secondly, it can acquire images very rapidly, and thus it has an excellent temporal resolution. Thirdly, an OT imaging device is easily portable and therefore it can be used in a natural, relaxed environment [42, 89]. A few reviews of optical brain imaging have been published, see e.g. [41, 42, 119, 222].

Most of the optical images of brain function have been produced by using simplifying assumptions of the tissue geometry and its optical properties. However, in recent years, more and more studies have been performed using tomographic approach in which the light transport in tissues is fully modelled. OT has been used to determine the optical properties of adult brain [58] and for bedside monitoring of premature infant brain [117]. In addition, the method has been widely studied with small animals, see e.g. [56, 64, 213]. Furthermore, to produce more accurate tomographic images, 3D imaging methods have been developed. The 3D imaging methods have been used to monitor haemodynamics of the human brain [34] and to reconstruct images of the activation of the motor cortex [78, 90]. In addition, 3D brain imaging has been applied in small animal studies [35, 36].

Recently, the state estimation techniques have been applied to the time varying reconstruction problem of OT [69, 148, 190]. The method provides a higher temporal resolution to the reconstruction and improves the estimates of functional haemodynamics. In addition, multi modality approaches which combine functional magnetic resonance imaging and optical tomography to brain imaging have been investigated [40, 247] and the state estimation techniques have been utilized in the integration of the multi modality data [120].

Neonatal brain imaging

Brain injury in pre-term and term infants is a major cause of permanent disability and death. The brain injury is caused when the supply of blood and oxygen to the certain parts of brain is disrupted. Currently, the infant brain injuries are diagnosed clinically by ultrasound, which gives only anatomical information, and by magnetic resonance imaging [89]. OT has been developed for imaging infant

brain since optical techniques can provide information about brain haemodynamic changes. Thus, OT may provide a bedside system to identify infants at risk, to diagnose injury, and to monitor treatment [89]. For a review of optical imaging of the neonatal brain, see e.g. [102].

After earlier approaches [33, 117], 3D imaging methods have been developed to produce accurate tomographic images of infant brain. A method to acquire 3D tomographic images from a newborn was introduced in [104]. The method has been used to monitor changes in blood volume and oxygenation in the newborn infant brain [103] and to image activation of the motor cortex [90]. The approach shows encouraging results.

Other tissues

In addition to the previous applications, imaging other tissues with optical tomography has also been investigated. However, the approach is restricted by the fast attenuation of the light across large thicknesses of tissue. Optical tomography has been used to image human forearm [116]. In addition, OT has been applied in imaging human fingers [114, 241]. The technique has been used for detection of rheumatoid arthritis joints [198].

Industrial applications

In addition to the biomedical applications, there has been growing interest towards the use of optical methods in industry [239]. Possible applications of OT in industry include process tomography where noninvasive measurement techniques to monitor both temporal and spatial behaviour of industrial processes are needed. Possible applications of OT in industrial process tomography include, for example, monitoring of pulp mixture flows in pipelines in paper industry [132].

2.2 Modelling and reconstruction

The image reconstruction problem in optical tomography is to estimate the optical properties within the object when the amount of guided light and the measured data on the boundary of the object are given. Image reconstruction problem in OT is a non-linear ill-posed inverse problem. There are no direct methods for the solution of this problem, and thus it is typically stated as a minimization problem such as regularized output least squares. The iterative solution of this problem requires repetitive solutions of the forward problem. Therefore, it is essential to have a computationally feasible forward model that describes light propagation in the medium accurately. Further, regularization techniques need to be used in image reconstruction of OT in order to overcome the difficulties due to the ill-posed nature of the problem.

2.2.1 Forward problem

The forward problem in optical tomography is to solve the measurable data when the optical properties of the medium and the input light sources are given. Light

propagation in biological materia is usually described through transport theory. In transport theory, the most often applied forward models to describe light propagation in tissues are the the radiative transfer equation and the diffusion approximation. In this thesis, modelling light propagation in tissues through transport theory is investigated. The light transport models are discussed in Chapter 3 and the finite element implementations of the models are given in Chapter 4.

2.2.2 Inverse problem

In the inverse problem of OT, absorption and scattering functions, or in some studies absorption and diffusion functions, within the object are reconstructed. If more than one wavelength of light is used, the haemoglobin concentration, oxygen saturation, and water distributions can be calculated from the absorption spectrum and some scattering characteristics from the scattering spectrum [74, 218]. Recently, there have also been studies in which the oxy-haemoglobin, deoxy-haemoglobin, water, scatter amplitude, and scatter power have been directly estimated from the measurements at many wavelengths [61, 62, 157, 220]. In this study, the reconstruction of the absorption and scattering coefficients (μ_a, μ_s), or absorption and reduced scattering coefficients (μ_a, μ_s'), are discussed.

The image reconstruction methods in OT can be divided into two classes which are the difference methods and the methods that are based on the regularized non-linear least squares approach. The theoretical uniqueness aspects of the OT problem have been discussed for example in [16, 62, 162, 197]. In [16] it was stated that the absorption and scattering effects can not be distinguished based on the intensity measurements only. More thorough reviews of the image reconstruction methods have been given for example in [11, 14, 145]. Here, a short review of the two reconstruction approaches is given following the presentation in [145].

Difference methods

The difference methods are based on the assumption that the absorption and scattering coefficients (μ_a, μ_s) do not differ much from the background values $(\mu_{a,\mathrm{ref}}, \mu_{s,\mathrm{ref}})$. The objective is to reconstruct a small perturbation

$$\begin{pmatrix} \delta\mu_a \\ \delta\mu_s \end{pmatrix} = \begin{pmatrix} \mu_a \\ \mu_s \end{pmatrix} - \begin{pmatrix} \mu_{a,\mathrm{ref}} \\ \mu_{s,\mathrm{ref}} \end{pmatrix}$$

based on a liner model

$$\delta\mathcal{Z} = K \begin{pmatrix} \delta\mu_a \\ \delta\mu_s \end{pmatrix} \tag{2.8}$$

where $\delta\mathcal{Z} = \mathcal{Z} - \mathcal{Z}_{\mathrm{ref}}$ is the difference between data which is measured with the optical properties (μ_a, μ_s) and the background optical properties $(\mu_{a,\mathrm{ref}}, \mu_{s,\mathrm{ref}})$, respectively. The matrix K can be constructed, for example, by assuming an infinite space or infinite half-space geometry in which an analytical expression can be written [88] or by utilizing Monte Carlo simulation [54]. The most typical approach for constructing the matrix K is through numerical methods in which case K is the Jacobian matrix for the forward model [11].

In OT, difference methods have been applied in functional brain studies [34, 64, 90, 103, 213] where the difference before and during the activation is monitored, and, in some extent, also in other studies such as breast imaging [202, 244]. Difference imaging is known to produce images with few artefacts. However, it can not be used when absolute baseline optical properties are required or when a reference measurement is not available.

Non-linear least squares approach

Most of the approaches to the OT inverse problem are based on the non-linear least squares approach. In the approach, a single data acquisition is used to estimate absolute values for the optical properties of the medium. The regularized non-linear least squares problem is to estimate absorption and scattering distributions (μ_a, μ_s) which minimize the functional

$$\Psi = \|L(\mathcal{Z} - \mathcal{F}(\mu_a, \mu_s))\|_2^2 + \mathcal{B}(\mu_a, \mu_s) \tag{2.9}$$

when the measured data, or data types which are derived from the measured data, $\mathcal{Z}$ are given. In functional (2.9), $\mathcal{F}$ is the forward model for light transport which maps the absorption and scattering parameters to the measurable data or data types. Further, term $\mathcal{B}(\mu_a, \mu_s) > 0$ is a regularizing penalty functional and the matrix L is a weight matrix which basically corresponds to the Cholesky factor of the inverse of the noise covariance matrix. The regularizing penalty functional is usually defined as

$$\mathcal{B}(\mu_a, \mu_s) = \alpha_{\mu_a}\mathcal{A}(\mu_a) + \alpha_{\mu_s}\mathcal{A}(\mu_s) \tag{2.10}$$

where $\mathcal{A}(\mu_a)$ and $\mathcal{A}(\mu_s)$ are the regularizing penalty functionals for the absorption coefficient and the scattering coefficient, respectively, and α_{μ_a} and α_{μ_s} are regularization parameters for absorption and scattering. Although it is possible to use different regularizing penalty functionals for the absorption and scattering, the most usual choice is to use the same penalty functional for both [145]. The different choices of the regularizing penalty functionals have been reviewed for example in [145].

The minimization problem (2.9) is usually solved using gradient methods such as the nonlinear conjugate gradient method [11, 19, 20, 113, 140] or Newton type methods [11, 19, 142, 145, 179, 180, 208]. In the Gauss-Newton method, the minimization problem can be solved iteratively as

$$\begin{aligned}\begin{pmatrix}\mu_a\\ \mu_s\end{pmatrix}_{(i+1)} &= \begin{pmatrix}\mu_a\\ \mu_s\end{pmatrix}_{(i)} \\ &+ c_{(i)}\left(J_{(i)}^T W J_{(i)} + \frac{1}{2}H_B^{(i)}\right)^{-1}\left(J_{(i)}^T W\left(\mathcal{Z} - \mathcal{F}(\mu_a^{(i)}, \mu_s^{(i)})\right) - \frac{1}{2}g_B^{(i)}\right)\end{aligned} \tag{2.11}$$

where i is the iteration index, $\mu_a = (\mu_{a,1}, \ldots, \mu_{a,M})^T \in \mathbb{R}^M$ and $\mu_s = (\mu_{s,1}, \ldots, \mu_{s,M})^T \in \mathbb{R}^M$ are the vectors of discretized absorption and scattering parameters, $W = L^T L$, $c_{(i)}$ is a step length parameter, $J_{(i)}$ is the Jacobian

for $\mathcal{F}(\mu_a^{(i)}, \mu_s^{(i)})$, and $g_B^{(i)}$ and $H_B^{(i)}$ are the gradient and Hessian of the penalty functional (2.10) [145].

In order to guarantee fast convergence in the image reconstruction, the initial values of the absorption and scattering need to be reasonably close to the actual (heterogeneous) optical properties. The initial guess for the optical properties is typically chosen to be constant if prior information about the internal structure of the domain is not available. Ways to obtain a constant initial guess have been discusses for example in [149, 165] as well as in Section 6.1.4 in which the initial estimation and final optode calibration are obtained as the final step of the proposed computational calibration procedure.

Some special approaches in image reconstruction

The inverse problem of OT has been widely studied and efficient reconstruction techniques are constantly developed in order to improve the quality of the image reconstruction. Next, some of the approaches to improved image reconstruction are briefly reviewed.

Use of anatomical and physiological prior information: One way to improve the quality of the image reconstruction is to utilize anatomical and physiological information of the target tissue acquired with other imaging methods. In [207] it was demonstrated that accuracy of OT reconstruction can be significantly improved if anatomical boundary information is used as a prior. One way to include anatomical information into the reconstruction problem is to use information obtained with other imaging modalities as the basis of the forward model. Within the approach, realistic finite element meshes that are based on magnetic resonance imaging have been built [40, 49, 185, 207, 212, 247]. In addition, patient-specific meshes have been generated using a set of sensors attached to the head surface and by fitting the mesh boundaries according to the sensor locations [91].

Alternatively, anatomical prior information can be utilized in the inverse problem of OT by using sophisticated regularizing penalty functionals. In the approach, x-ray tomography [156] and magnetic resonance imaging [46, 47, 96] have been utilized. Furthermore, utilizing both physiological and anatomical priors in the OT inverse problem have been investigated [48, 122, 155].

Recovery of object shape: In OT the reconstruction of the optical parameters is conventionally carried out in a pixel basis in which case the resulting number of unknowns makes the inverse problem severely ill-posed. Alternatively, the boundaries of piecewise constant tissue regions as well as the optical properties within them can be estimated. The method was first applied in estimating region boundaries when the optical properties of the regions were known *a priori* [146]. It was later extended to solve simultaneously the boundaries of tissue regions together with the optical parameters within them [147]. Further, a three stage approach to estimation of piecewise constant coefficients was introduced in [149]. In the approach, an initial image reconstruction was used to identify the number of regions and their approximate locations before finally solving for the boundaries and the optical properties of the regions. In addition, techniques in which the

recovery of the object shape and estimation of the optical properties are obtained simultaneously have been developed [135, 210].

State estimation approach: The state estimation techniques have been developed for the time varying reconstruction problem of OT [148]. In the state estimation approach, it is assumed that the optical properties are non-stationary in the sense that they may exhibit significant changes during the time that is needed to measure data for one traditional imaging frame. The objective is to estimate a sequence of states for the process when the state evolution model for the process, the light transport model for the OT experiments, and data on the boundary are given. The state estimates can be computed using Kalman filtering techniques. The state estimation approach has been successfully applied in OT in [69, 120, 190].

Approximation error approach: The OT inverse problem can be considered in the framework of Bayesian statistics. In the statistical approach, all parameters are modelled as random variables. The parameters depend on each other through a model and information about the parameters is expressed by probability distributions. In the inverse problem, the idea is to obtain information about the unknown parameters of interest based on all the knowledge of the measurements, the model, and the prior information about the parameters. The statistical inversion theory offers a natural way to deal with the prior information about the object. For more information about statistical inversion theory, see e.g. [127], and about the OT inverse problem in the framework of Bayesian statistics, see e.g. [145]. The Bayesian model of the OT problem has also been considered for example in [96, 150, 166, 245, 246].

In the approximation error approach, the error caused by representing the parameters through a discretized forward model is treated as noise. Then, an approximation error model is generated and it is taken into account when solving the inverse problem of OT. For the basics of the approximation error theory, see [127, 128]. The approach has been utilized in OT in the presence of anisotropies [107] and geometric mismodelling [108] utilizing Gaussian priors for the anisotropy parameters. Furthermore, the approximation error approach has been applied to inverse problem of OT in [22] where it was shown that the accuracy of the computational model for the forward problem can be relaxed if the approximation error model is used.

Chapter III

Light transport models

Wave propagation in random media, such as light propagation in biological materia, have been described through two theories, namely the analytical theory and the transport theory. The analytical theory starts with with basic differential equations, such as the Maxwell equations, and approximate equations to describe wave propagation in random media are derived [123]. However, in practice exact analytical models are difficult or even impossible to obtain.

Therefore, the transport theory is usually applied to describe transport of energy through a medium containing scattering particles. In transport theory, the particle conservation within a small volume element of phase space is investigated. The wave phenomenon of particles is ignored. Within the phase space element, the particles undergo scattering through elastic collisions and the energy of the particles is decreased through absorption and increased through radiation sources. The transport theory has successfully been applied in many areas of science such as neutron transport, transfer of charged particles, underwater visibility, marine biology, biomedical optics, and radiative transfer in planetary and stellar atmospheres [6, 50, 51, 53, 73, 123, 177].

The transport theory can be modelled through stochastic methods, such as Monte Carlo, and deterministic methods which are based on describing particle transport with partial differential equations. In the stochastic methods, individual particle interactions are modelled as the particles are scattered and absorbed within the medium. The two stochastic methods that have been used in optical tomography are the Monte Carlo method and the random walk theory [14]. The Monte Carlo is the most often used stochastic method in OT and it is usually chosen as the reference method to which other solutions are compared. For more information about Monte Carlo, see Section 4.4.

In deterministic approach, particle transport is described with partial differential equations which can be solved either analytically or numerically [14]. The basic equation of the transport theory is the transport equation which is a linear version of the Boltzmann equation. It can be derived from kinetic gas theory [51] or simply by investigating particle conservation within a small volume element of phase space [50, 53, 73]. In optical tomography, a generally used model for light transport is the radiative transfer equation which is a one-speed approximation of

the transport equation.

Analytical solutions for the transport equation are available only for few simple geometries and the numerical solutions often lead to computationally enormous problems. Thus, in many cases, the transport equation is too complicated to be used in practical applications and approximate models are applied. In highly scattering medium, such as biological tissue, the transport equation is approximated by diffusion theory. The governing equation is the diffusion approximation to the radiative transfer equation.

In this chapter, modelling light propagation in tissues through transport theory is discussed. The radiative transfer equation is reviewed in Section 3.1 and the diffusion approximation and its derivation are reviewed in Section 3.2. Further, two new hybrid methods to the forward problem of OT are proposed. A hybrid radiative transfer – diffusion model is proposed in Section 3.3 and a coupled radiative transfer equation and diffusion approximation model is proposed in Section 3.4. The finite element implementations of the light transport models are given later in Chapter 4.

3.1 Radiative transfer equation

A widely accepted model for light propagation in tissues is the radiative transfer equation (RTE). It has been used as the light transport model in a few applications of OT [24, 71, 111, 138, 144, 240]. Further, the inverse problem for the RTE has been discussed and the RTE has been used in the image reconstruction problem of OT for example in [1, 26, 27, 114, 141].

The RTE is a one-speed approximation of the transport equation, and it is obtained by integrating the transport equation over energy and by approximating the parameters by energy-averaged parameters [50, 73]. Thus, the RTE assumes that the energy (or speed) of the particles does not change in collisions and that the refractive index is constant within the medium. For discussion of photon transport in medium with spatially varying refractive index, see e.g. [83, 134, 161, 189].

Let $\Omega \subset \mathbb{R}^n$, $n = 2$ or 3 denote the physical domain which is considered isotropic in the sense that the probability of scattering between two directions depends only on the relative angle between those directions, not on an absolute direction. For discussion of light propagation in anisotropic medium, see e.g. [105, 106]. Furthermore, let $\partial\Omega$ denote the boundary of the domain and $\hat{s} \in S^{n-1}$ denote a unit vector in the direction of interest. The RTE is written in time-domain as

$$\begin{aligned} &\frac{1}{c}\frac{\partial\phi(r,\hat{s})}{\partial t} + \hat{s}\cdot\nabla\phi(r,\hat{s}) + (\mu_s+\mu_a)\phi(r,\hat{s}) \\ &\quad = \mu_s \int_{S^{n-1}} \Theta(\hat{s}\cdot\hat{s}')\phi(r,\hat{s}')\mathrm{d}\hat{s}' + q(r,\hat{s}) \end{aligned} \tag{3.1}$$

and in frequency-domain as

$$\frac{\mathrm{i}\omega}{c}\phi(r,\hat{s}) + \hat{s}\cdot\nabla\phi(r,\hat{s}) + (\mu_s+\mu_a)\phi(r,\hat{s}) = \mu_s\int_{S^{n-1}}\Theta(\hat{s}\cdot\hat{s}')\phi(r,\hat{s}')\mathrm{d}\hat{s}' + q(r,\hat{s}) \tag{3.2}$$

where c is the speed of light in the medium, i is the imaginary unit, ω is the angular modulation frequency of the input signal, and $\mu_s = \mu_s(r)$ and $\mu_a = \mu_a(r)$ are the scattering and absorption coefficients of the medium, respectively. The scattering coefficient represents the probability per unit length of a photon being scattered and the absorption coefficient represents the probability per unit length of a photon being absorbed. Furthermore, $\phi(r,\hat{s})$ is the radiance, $\Theta(\hat{s}\cdot\hat{s}')$ is the scattering phase function, and $q(r,\hat{s})$ is the source inside Ω. The radiance can be defined so that the amount of power transfer in the infinitesimal angle $\mathrm{d}\hat{s}$ in direction $\hat{s}$ at time t through an infinitesimal area $\mathrm{d}S$ is given by

$$\phi(r,\hat{s};t)\hat{s}\cdot\hat{n}\mathrm{d}S\mathrm{d}\hat{s}$$

where $\hat{n}$ is the normal to the surface $\mathrm{d}S$ [53, 123].

The scattering phase function $\Theta(\hat{s}\cdot\hat{s}')$ describes the probability that a photon with an initial direction $\hat{s}'$ will have a direction $\hat{s}$ after a scattering event. It can be regarded as a probability distribution function, and thus it is a non-negative function satisfying

$$\int_{S^{n-1}}\Theta(\hat{s}\cdot\hat{s}')\mathrm{d}\hat{s} = \int_{S^{n-1}}\Theta(\hat{s}\cdot\hat{s}')\mathrm{d}\hat{s}' = 1. \tag{3.3}$$

In OT, the most usual phase function for isotropic material is the Henyey–Greenstein scattering function [110] which in a three-dimensional case is of the form

$$\Theta(\hat{s}\cdot\hat{s}') = \frac{1}{4\pi}\frac{1-g^2}{(1+g^2-2g\hat{s}\cdot\hat{s}')^{3/2}} \tag{3.4}$$

and in a two-dimensional case is of the form

$$\Theta(\hat{s}\cdot\hat{s}') = \frac{1}{2\pi}\frac{1-g^2}{(1+g^2-2g\hat{s}\cdot\hat{s}')}. \tag{3.5}$$

The scattering shape parameter g defines the shape of the probability density and it gets values between $-1 < g < 1$. With the value $g = 0$, the scattering probability density is a uniform distribution. For forward dominated scattering $g > 0$ and for backward dominated scattering $g < 0$. Although the Henyey–Greenstein phase function is the most widely adopted phase function in biomedical optics, it shows discrepancies compared with the Mie theory, which gives an exact solution of the scattering of a plane electromagnetic wave by an isotropic and homogeneous sphere, especially when the scattering probability is highly forward peaked [24, 25]. The popularity of the Henyey–Greenstein phase function is due to the fact that

the mean of the cosine of the scattering angle, see forward for equation (3.22), is g. For more information about scattering theory and phase functions, see e.g. [123, 233].

The RTE is basically a balance equation for the change in the radiance. If we consider a small element in phase space, that is a small volume $\mathrm{d}V$ around a position r and a small solid angle around direction $\hat{s}$ at time t, the components of the time-domain RTE (3.1) can be interpreted by the following way [37, 50, 73, 177]. The first term on the left hand side is the time derivative of the radiance which equals to the change in the radiance, i.e. the number of photons entering the element minus the number of leaving. The second term represents the flux of photons along the direction $\hat{s}$, i.e. the loss of photons through the surfaces of the volume $\mathrm{d}V$. The third term accounts for the loss of photons due to the absorption and the loss of photons due to the scattering from direction $\hat{s}$ into other directions. On the right hand side, the first term represents the gain of photons due to the scattering from other directions into the direction $\hat{s}$ and the second term represents the gain of photons through radiation sources. The time-domain and frequency-domain representations of the RTE are related through Fourier transform, and thus they have the relation

$$\frac{\partial}{\partial t} \Leftrightarrow \mathrm{i}\omega.$$

3.1.1 Boundary and source conditions for the RTE

In order to obtain a unique solution for the RTE, the ingoing radiance distribution on the boundary $\partial\Omega$, that is, $\phi(r, \hat{s})$ for $\hat{s} \cdot \hat{n} < 0$, where $\hat{n}$ is outward unit normal, need to be known [50]. Several boundary conditions can be applied to the RTE [2, 73, 127]. In OT, we use the boundary condition which assumes that no photons travel in an inward direction at the boundary $\partial\Omega$, thus [11]

$$\phi(r, \hat{s}) = 0, \qquad r \in \partial\Omega, \quad \hat{s} \cdot \hat{n} < 0. \tag{3.6}$$

This boundary condition, also known as the free surface boundary condition and the vacuum boundary condition, implies that once a photon escapes the domain Ω it does not reenter it. The boundary condition (3.6) can be modified to include a boundary source $\phi_0(r, \hat{s})$ at the source position $\varepsilon_j \subset \partial\Omega$ and it can be written in the form [229]

$$\phi(r, \hat{s}) = \begin{cases} \phi_0(r, \hat{s}), & r \in \cup_j \varepsilon_j, \quad s \cdot \hat{n} < 0 \\ 0, & r \in \partial\Omega \backslash \cup_j \varepsilon_j, \quad s \cdot \hat{n} < 0. \end{cases} \tag{3.7}$$

In OT, the measurable quantity is the exitance $\Gamma(r)$ on the boundary of the domain. It is defined as [14]

$$\Gamma(r) = \int_{S^{n-1}} (\hat{s} \cdot \hat{n}) \phi(r, \hat{s}) \mathrm{d}\hat{s}, \qquad r \in \partial\Omega. \tag{3.8}$$

Furthermore, other quantities of interest are the photon density

$$\Phi(r) = \int_{S^{n-1}} \phi(r, \hat{s}) \mathrm{d}\hat{s} \tag{3.9}$$

and the photon current

$$J(r) = \int_{S^{n-1}} \hat{s}\phi(r,\hat{s})\mathrm{d}\hat{s}. \tag{3.10}$$

3.2 Diffusion approximation

In OT, light propagation in tissues is usually modelled with the diffusion approximation (DA) to the RTE. The most typical approach to derive the DA from the RTE is to expand the radiance, the source term, and the phase function into series using the spherical harmonics and truncate the series [6, 11, 37, 50, 73]. If the spherical harmonics series is truncated at the Nth moment, P_N approximation is obtained [11, 37, 73]. The first order spherical harmonics approximation is referred as the P_1 approximation and the DA can be regarded as a special case for that. An alternative to the P_N approximation is the Boltzmann hierarchy - approach in which moments of radiance are used to form a set of coupled equations that approximate the RTE [86, 130]. Furthermore, the DA can be derived using asymptotic techniques [29] or by using projection algebra [73, 106, 127].

Here a short review of the derivation of the DA is given according to [106, 123, 127]. First, the P_1 approximation is derived, and then, the DA is formed as a special case for that. In the derivation, the following integral rules are utilized

$$\int_{S^{n-1}} 1\mathrm{d}\hat{s} = \left|S^{n-1}\right| \tag{3.11}$$

$$\int_{S^{n-1}} \hat{s}\mathrm{d}\hat{s} = 0 \tag{3.12}$$

$$\int_{S^{n-1}} \hat{s}\cdot\mathcal{A}\mathrm{d}\hat{s} = 0 \tag{3.13}$$

$$\int_{S^{n-1}} (\hat{s}\cdot\mathcal{B})(\hat{s}\cdot\mathcal{C})\mathrm{d}\hat{s} = \frac{\left|S^{n-1}\right|}{n}(\mathcal{B}\cdot\mathcal{C}) \tag{3.14}$$

$$\int_{S^{n-1}} \hat{s}(\hat{s}\cdot\mathcal{D})\mathrm{d}\hat{s} = \frac{\left|S^{n-1}\right|}{n}\mathcal{D} \tag{3.15}$$

where $\mathcal{A}$, $\mathcal{B}$, $\mathcal{C}$, and $\mathcal{D}$ are vectors ($n = 2, 3$). In the P_1 approximation framework, it is assumed that the angular distribution of the radiance $\phi(r,\hat{s})$ is almost uniform [123]. This assumption can be achieved within highly scattering medium relatively far from the sources. The approximation that is used for the radiance is of the form

$$\phi(r,\hat{s}) \approx \frac{1}{\left|S^{n-1}\right|}\Phi(r) + \frac{n}{\left|S^{n-1}\right|}\hat{s}\cdot J(r) \tag{3.16}$$

where $\Phi(r)$ and $J(r)$ are the photon density and the photon current as in equations (3.9) and (3.10). The equation (3.16) may be regarded as the first two terms of Taylor's expansion of $\phi(r,\hat{s})$ in terms of powers of $\hat{s}\cdot\hat{s}'$, and therefore the second term in equation (3.16) should be considerably smaller than the first term, thus $|J(r)| \ll \Phi(r)$ [123]. A similar approximation can be written for the source term.

It is of the form

$$q(r,\hat{s}) \approx \frac{1}{|S^{n-1}|} q_0(r) + \frac{n}{|S^{n-1}|} \hat{s} \cdot q_1(r) \tag{3.17}$$

where $q_0(r)$ and $q_1(r)$ are the isotropic and dipole components of the source, respectively, thus

$$q_0(r) = \int_{S^{n-1}} q(r,\hat{s}) \mathrm{d}\hat{s} \tag{3.18}$$

$$q_1(r) = \int_{S^{n-1}} \hat{s} q(r,\hat{s}) \mathrm{d}\hat{s}. \tag{3.19}$$

For the phase function, we write an approximation

$$\Theta(\hat{s} \cdot \hat{s}') \approx \frac{1}{|S^{n-1}|} g_0 + \frac{n}{|S^{n-1}|} (\hat{s} \cdot \hat{s}') g_1 \tag{3.20}$$

where g_0 is, according to equation (3.3),

$$g_0 = \int_{S^{n-1}} \Theta(\hat{s} \cdot \hat{s}') \mathrm{d}\hat{s} = 1 \tag{3.21}$$

and g_1 is the mean of the cosine of the scattering angle

$$g_1 = \int_{S^{n-1}} (\hat{s} \cdot \hat{s}') \Theta(\hat{s} \cdot \hat{s}') \mathrm{d}\hat{s}. \tag{3.22}$$

In case of the Henyey–Greenstein scattering function, equations (3.4) and (3.5), we have $g_1 = g$.

To derive the P_1 approximation, let us first investigate the integral-term in the right side of the RTE (3.2). Substituting the approximation (3.20) into the integral-term and utilizing equations (3.9) and (3.10), we can write

$$\begin{aligned}
&\mu_s \int_{S^{n-1}} \Theta(\hat{s} \cdot \hat{s}') \phi(r,\hat{s}') \mathrm{d}\hat{s}' \\
=&\mu_s \frac{1}{|S^{n-1}|} \int_{S^{n-1}} \phi(r,\hat{s}') \mathrm{d}\hat{s}' + \mu_s \frac{n}{|S^{n-1}|} g_1 \int_{S^{n-1}} (\hat{s} \cdot \hat{s}') \phi(r,\hat{s}') \mathrm{d}\hat{s}' \\
=&\mu_s \frac{1}{|S^{n-1}|} \Phi(r) + \mu_s \frac{n}{|S^{n-1}|} g_1 \hat{s} \cdot J(r).
\end{aligned} \tag{3.23}$$

Inserting the above equation and approximations (3.16) and (3.17) into the RTE (3.2), the following equation is obtained

$$\begin{aligned}
&\left(\frac{\mathrm{i}\omega}{c} + \hat{s} \cdot \nabla + (\mu_s + \mu_a) \right) \left(\frac{1}{|S^{n-1}|} \Phi(r) + \frac{n}{|S^{n-1}|} \hat{s} \cdot J(r) \right) \\
=&\mu_s \frac{1}{|S^{n-1}|} \Phi(r) + \mu_s \frac{n}{|S^{n-1}|} g_1 \hat{s} \cdot J(r) + \frac{1}{|S^{n-1}|} q_0(r) + \frac{n}{|S^{n-1}|} \hat{s} \cdot q_1(r).
\end{aligned} \tag{3.24}$$

This can further be written as

$$\frac{1}{|S^{n-1}|}\left(\frac{\mathrm{i}\omega}{c}+\hat{s}\cdot\nabla+\mu_a\right)\Phi(r)+\frac{n}{|S^{n-1}|}\left(\frac{\mathrm{i}\omega}{c}+\hat{s}\cdot\nabla+\mu_a+\mu_s'\right)\hat{s}\cdot J(r)$$
$$=\frac{1}{|S^{n-1}|}q_0(r)+\frac{n}{|S^{n-1}|}\hat{s}\cdot q_1(r). \tag{3.25}$$

where $\mu_s'=\mu_s'(r)=\mu_s(1-g_1)$ is the reduced scattering coefficient. Integrating equation (3.25) over angular directions S^{n-1} and utilizing equations (3.11)–(3.15), the following equation is obtained

$$\left(\frac{\mathrm{i}\omega}{c}+\mu_a\right)\Phi(r)+\nabla\cdot J(r)=q_0(r). \tag{3.26}$$

Similarly, multiplying equation (3.25) with $\hat{s}$ and integrating over angular directions S^{n-1}, the following equation is obtained

$$\left(\frac{\mathrm{i}\omega}{c}+\mu_a+\mu_s'\right)J(r)+\frac{1}{n}\nabla\Phi(r)=q_1(r). \tag{3.27}$$

Equations (3.26) and (3.27) are known as the P_1 approximation.

To derive the diffusion approximation, it is further assumed that the light source is isotropic, thus $q_1(r)=0$, and that $\frac{\mathrm{i}\omega}{c}J(r)=0$. The latter assumption, which in time-domain case is of the form $\frac{1}{c}\frac{\partial J(r)}{\partial t}=0$, is usually justified by specifying the condition $\mu_a\ll\mu_s'$ [11]. Utilizing these approximations, equation (3.27) gives the Fick's law

$$J(r)=-\kappa\nabla\Phi(r) \tag{3.28}$$

where $\kappa=\kappa(r)=(n(\mu_a+\mu_s'))^{-1}$ is the diffusion coefficient. Substituting equation (3.28) into equation (3.26), the frequency-domain version of the DA is obtained. It is of the form

$$-\nabla\cdot\kappa\nabla\Phi(r)+\mu_a\Phi(r)+\frac{\mathrm{i}\omega}{c}\Phi(r)=q_0(r). \tag{3.29}$$

The DA has an analog in time-domain as well. It is of the form

$$-\nabla\cdot\kappa\nabla\Phi(r)+\mu_a\Phi(r)+\frac{1}{c}\frac{\partial\Phi(r)}{\partial t}=q_0(r). \tag{3.30}$$

The time-domain and frequency-domain representations of the DA are related through Fourier transform, similarly as in the case of the RTE.

3.2.1 Boundary conditions for the DA

The diffusion approximation can not satisfy the boundary condition (3.6) [11, 50]. Instead there are a few boundary conditions that have been applied to the DA. The simplest boundary condition is the Dirichlet boundary condition which is also referred as the zero-boundary condition. It sets the photon density to zero on the

boundary, thus $\Phi(r) = 0$, $r \in \partial\Omega$ [97, 112, 211]. Alternatively, an extrapolated boundary condition can be used [60, 73, 97, 112, 211]. In the approach, the photon density is set to zero on an extrapolated boundary which is a virtual boundary outside the medium located at a certain distance from the real boundary. Both the zero-boundary condition and the extrapolated boundary condition are physically incorrect and they have mostly been used because of their mathematical simplicity [97, 112].

The most often used boundary condition in OT is the Robin boundary condition which is also referred as the partial current boundary condition [8, 50, 60, 73, 82, 92, 97, 112, 123, 133, 211]. It can be derived as follows. Within the P_1 approximation framework (3.16), it can be shown that the total inward directed photon flux at a point r on the boundary $\partial\Omega$ is of the form

$$\Gamma_-(r) = -\int_{\hat{s}\cdot\hat{n}<0} (\hat{s}\cdot\hat{n})\phi(r,\hat{s})\mathrm{d}\hat{s} = \gamma_n\Phi(r) - \frac{1}{2}\hat{n}\cdot J(r) \tag{3.31}$$

where γ_n is a dimension-dependent constant which obtains values $\gamma_2 = 1/\pi$ and $\gamma_3 = 1/4$ [106, 127]. Similarly, for the outward directed photon flux at a point $r \in \partial\Omega$, it can be written [127]

$$\Gamma_+(r) = \int_{\hat{s}\cdot\hat{n}>0} (\hat{s}\cdot\hat{n})\phi(r,\hat{s})\mathrm{d}\hat{s} = \gamma_n\Phi(r) + \frac{1}{2}\hat{n}\cdot J(r). \tag{3.32}$$

To derive the Robin boundary condition for the DA, it is assumed that the total inward directed photon flux on the boundary is zero, thus

$$\Gamma_-(r) = 0, \qquad r \in \partial\Omega. \tag{3.33}$$

Utilizing equation (3.31) and the Fick's law (3.28), the Robin boundary condition can be derived. It is of the form

$$\Phi(r) + \frac{1}{2\gamma_n}\kappa\frac{\partial\Phi(r)}{\partial\hat{n}} = 0, \qquad r \in \partial\Omega. \tag{3.34}$$

The boundary condition (3.34) can be extended to include the reflection on the boundary that is caused by different refractive indices between the object and the surrounding medium. In that case, equation (3.33) is modified to the form

$$\Gamma_-(r) = R\Gamma_+(r), \qquad r \in \partial\Omega \tag{3.35}$$

where $R = R(x)$ is the reflection coefficient on the boundary $\partial\Omega$, with $0 \leq R \leq 1$ [127]. Thus, if $R = 0$, no boundary reflection occurs and equation (3.35) is reduced into equation (3.33). The parameter R can be derived from Fresnel's law [97, 133], or, if the refractive index of the surrounding medium is $n_{\mathrm{out}} = 1$, by an experimental fit

$$R \approx -1.4399n_{\mathrm{in}}^{-2} + 0.7099n_{\mathrm{in}}^{-1} + 0.6681 + 0.0636n_{\mathrm{in}} \tag{3.36}$$

where n_{in} is the refractive index of the medium [92, 211]. Utilizing equations (3.31) and (3.32), and the Fick's law (3.28), the Robin boundary condition with mismatched refractive indices can be derived. It takes the form

$$\Phi(r) + \frac{1}{2\gamma_n}\kappa A\frac{\partial\Phi(r)}{\partial\hat{n}} = 0, \qquad r \in \partial\Omega \tag{3.37}$$

where $A = (1 + R)/(1 - R)$, with $A = 1$ in the case of no surface reflection.

The boundary conditions of the DA for an interface between two highly scattering materials have been discussed for example in [8, 81, 194]. Furthermore, modelling photon diffusion in medium which consists of regions with different refractive indices has been discussed for example in [66, 153, 200].

The exitance, which is the measurable quantity on the boundary of the domain, equation (3.8), can be written utilizing equations (3.31), (3.32), the Fick's law (3.28), and the boundary condition (3.37). In the DA framework, the exitance is of the form

$$\begin{aligned}\Gamma(r) &= \Gamma_+(r) - \Gamma_-(r) = \hat{n}\cdot J(r)\\ &= -\kappa\frac{\partial\Phi(r)}{\partial\hat{n}} = \frac{2\gamma_n}{A}\Phi(r), \qquad r \in \partial\Omega.\end{aligned} \tag{3.38}$$

3.2.2 Source models for the DA

In the DA framework, light sources are usually modelled by two approximate models, namely the collimated source model and the diffuse source model. In case of the collimated source model, the source is modelled as an isotropic point source

$$q_0(r) = \delta(r - r_s) \tag{3.39}$$

where position r_s is located at a depth $1/\mu_s'$ below the source site [97, 112, 211]. In case of the diffuse source model, the source is modelled as an inward directed diffuse boundary current I_s at the source position $\varepsilon_j \subset \partial\Omega$ [211]. In case of the diffuse source model, equation (3.35) can be modified as

$$\Gamma_-(r) = R\Gamma_+(r) + (1 - R)I_s, \qquad r \in \cup_j\varepsilon_j. \tag{3.40}$$

Then, following the similar procedure as earlier, the Robin boundary condition with the diffuse source model is obtained. It is of the form

$$\Phi(r) + \frac{1}{2\gamma_n}\kappa A\frac{\partial\Phi(r)}{\partial\hat{n}} = \begin{cases}\frac{I_s}{\gamma_n}, & r \in \cup_j\varepsilon_j\\ 0, & r \in \partial\Omega \setminus \cup_j\varepsilon_j.\end{cases} \tag{3.41}$$

3.2.3 Validity of the DA

The basic condition for the validity of the DA is that the angular distribution of the radiance is almost uniform. In order to achieve this, the medium must be scattering dominated, thus $\mu_a \ll \mu_s$. Most of the tissue types are highly scattering and the DA can be regarded as a good approximation for modelling light propagation

within them. The DA has been found to describe light propagation with a good accuracy in situations in which its assumptions are valid [82, 92, 136, 175] and it has been successfully applied in many applications of OT, see e.g. [34, 41, 104, 116, 190, 217, 242].

However, the condition stating that the angular distribution of the radiance must be almost uniform is violated close to the highly collimated light sources that are used in OT. In addition, the condition can not be fulfilled in strongly absorbing or low-scattering tissues such as the cerebrospinal fluid (CSF) which surrounds the brain and fills the brain ventricles. Furthermore, in addition to above conditions, the DA can not accommodate realistic boundary conditions or discontinuities at interfaces. The diffusion theory has been found to fail in situations in which its approximations are not valid such as close to the sources [4, 79, 92, 211] and within low-scattering regions [84, 111, 174]. It has also been shown that these limitations in diffusion theory can lead to large errors in the reconstructed images [65].

Methods to improve the accuracy of the diffusion theory have been widely studied in cases of low-scattering and non-scattering regions [13, 98, 173, 195] and in correct modelling of boundaries, interfaces, and sources [5, 79, 87, 216, 236]. In addition, anisotropic scattering [105, 106, 109] and correct expression of the diffusion coefficient [9, 76, 87] have been investigated. In the following two sections, a few hybrid approaches that have been developed to overcome the limitations of the diffusion theory are briefly reviewed and two new hybrid approaches, the hybrid model and the coupled RTE–DA model, are proposed.

3.3 Hybrid radiative transfer – diffusion model

To overcome the limitations of the diffusion theory close to the sources, some hybrid methods have been developed. In this section, two hybrid approaches are briefly reviewed and a new hybrid radiative transfer – diffusion model for the forward problem of OT is proposed.

In order to overcome the limitations of the diffusion theory close to the light sources, some hybrid approaches have been reported. In the hybrid Monte Carlo – diffusion method, Monte Carlo simulation is combined with diffusion theory. The method was introduced in [236] to describe light reflectance in a semi-infinite turbid medium and it was extended for turbid slabs in [238]. Later, Monte Carlo – diffusion hybrid model was developed for a two-layer turbid medium in the frequency-domain [3, 5]. In the hybrid Monte Carlo – diffusion approach, Monte Carlo used to simulate light propagation close to the light source and the DA is analytically solved elsewhere in the domain. Monte Carlo is known to describe light propagation accurately. However, it has the disadvantage of requiring a long computation time. This has effects on computation times of the hybrid Monte Carlo approaches as well. As another approach, the Fokker–Planck equation has been used to describe light propagation close to the light sources [139]. The Fokker–Planck equation has been found to describe light propagation accurately when the scattering is strongly peaked in the forward direction. Therefore, it be can utilized at the small depths below highly collimated light sources. However, it does not

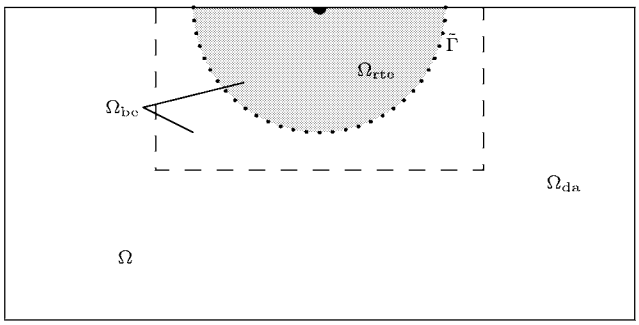

Figure 3.1: Domain Ω with a source at the centre of the upper edge. The RTE is solved in the sub-domain Ω_{be} (dashed line) and the RTE solution is used to construct a Dirichlet boundary condition for the DA on the fictitious interface $\tilde{\Gamma}$ (dotted line). The RTE is used as the forward model in the sub-domain Ω_{rte} (grey colour) and the DA is used as the forward model in the sub-domain Ω_{da} (white colour).

describe light propagation accurately at greater depths in biological tissues nor within low-scattering and non-scattering medium.

In this section, a hybrid radiative transfer – diffusion model to describe light propagation in highly scattering medium is proposed. In the hybrid radiative transfer – diffusion model, light propagation is modelled with the RTE in the proximity of the light sources and the DA is used elsewhere in the domain. The solution of the RTE is used to construct a Dirichlet boundary condition for the DA on a fictitious interface within the object. This boundary condition constitutes a distributed source model for the DA in the remaining area.

Let $\Omega \subset \mathbb{R}^n$, $n = 2 \text{ or } 3$ be the computational domain as in Figure 3.1 for the case $n = 2$. The source is located at the centre of the upper edge. The proposed hybrid model consists of two parts: solving the RTE based source model for the DA and solving the DA. The forward solution is obtained as follows. First, the RTE is solved in the sub-domain Ω_{be} close to the source using equation (3.2). The sub-domain Ω_{be} is marked in Figure 3.1 with dashed line. Then, the solution of the RTE is used to construct a Dirichlet boundary condition for the DA on the fictitious interface $\tilde{\Gamma}$ between the RTE and DA sub-domains Ω_{rte} and Ω_{da}. The interface $\tilde{\Gamma}$, which is marked in Figure 3.1 with dotted line, separates the domain Ω into two disjoint subsets Ω_{rte} (grey colour), in which the RTE is used as the forward model, and Ω_{da} (white colour), in which the DA is used as the forward model. The location of the interface $\tilde{\Gamma}$ should be chosen far enough from the source so that the angular distribution of the radiance $\phi(r, \hat{s})$ is well approximated by the first order approximation (3.16). This condition can be, for example, verified by monitoring the deviation of the radiance from the first order approximation. In

addition, the size of the domain Ω_{be} should be chosen somewhat larger than Ω_{rte}. This is due to the fact that the boundary condition specifying that no photons travel into inward directions at $\partial\Omega_{\text{be}}$ except at the source location is physically incorrect when the RTE is solved in the sub-domain Ω_{be}. Thus, the photons that are scattered back to the domain Ω_{be} from $\Omega \setminus \Omega_{\text{be}}$ are neglected. Finally, the DA is solved in the sub-domain Ω_{da} with equation (3.29). The RTE based Dirichlet boundary condition is used on $\tilde{\Gamma}$ and the Robin boundary condition (3.37) is used elsewhere on $\partial\Omega_{\text{da}}$. The RTE based Dirichlet boundary condition on the interface $\tilde{\Gamma}$ can be considered as a distributed source model for the DA.

The hybrid model utilizes the RTE in the proximity of the sources, and therefore it corrects the inaccuracy of the diffusion theory close to the sources. The DA is used as the forward model elsewhere in the domain where its approximations are valid. Thus, the hybrid model can be expected to describe light propagation accurately in highly scattering medium both close and farther from the source. One example of such highly scattering medium is the breast tissue. However, the hybrid model can not be utilized in situations in which the highly scattering medium contains low-scattering or non-scattering regions. A more general coupled RTE–DA model is discussed next. In the approach, the RTE and DA are coupled with boundary conditions and solved simultaneously. This more general coupled model can also be used in other situations in which the approximations of the diffusion theory are not valid.

3.4 Coupled radiative transfer equation and diffusion approximation

To overcome the limitations of the diffusion theory within low-scattering and non-scattering regions, different hybrid approaches and approximative models have been developed. In this section, some of these hybrid approaches are reviewed and a new coupled radiative transfer equation and diffusion approximation model for the forward problem of OT is proposed.

Different hybrid approaches and approximative models have been applied for highly scattering media with low-scattering and non-scattering regions. Methods that combine Monte Carlo simulation with diffusion theory have been applied for turbid media with low-scattering regions. The finite element approximation of the DA and the Monte Carlo simulation were combined in [98] to describe light propagation in a scattering medium with a low-scattering layer. However, also in this case, the approach suffers from the time consuming nature of the Monte Carlo methods. Moreover, the hybrid Monte Carlo – diffusion methods often require iterative mapping between the models which increases computation times even more. The radiosity–diffusion model [13, 84, 196] can be applied for highly scattering media with non-scattering regions. The method uses the DA to model light propagation within highly scattering regions and the radiosity model to model light propagation within non-scattering regions. The mathematical analysis of the problem was given in [121]. The radiosity–diffusion approach has been tested with reconstructions and it has been found to improve the quality of the reconstructed

images significantly compared to the traditional diffusion model [65, 67, 193]. A coupled transport and diffusion model was introduced in [30]. In the model, the transport and diffusion models are coupled and iterative mapping between the models is used for the forward solution. Further, a generalized diffusion model has been developed for photon migration within highly scattering medium with thin non-scattering layers and large non-diffusive inclusions [28, 29, 31]. Coupling the transport equations with diffusion theory in an infinite slab has also been discussed in [231, 232]. Further, utilizing the Fokker–Planck equation has also been studied in a simple geometry of scattering medium which contains an absorbing plate [137]. The method utilizes the Kirchhoff approximation in modelling light transport in an absorbing plate. Furthermore, utilizing higher order approximations to the RTE have been investigated [37, 124, 240]. The variable order approximations to the RTE method was proposed in [240]. The method is based on adaptive P_N approach in which the order of the angular basis is varied according the local optical properties of the domain. In addition, a simplified spherical harmonics method in which the RTE is approximated by a set of diffusion like equations was proposed in [143].

In this section, a coupled radiative transfer equation and diffusion approximation model for the forward problem of OT is proposed. In the approach, the RTE is used as the forward model in sub-domains in which the assumptions of the DA are not valid and the DA is used elsewhere in the domain. In the model, the RTE and DA are coupled through boundary conditions between the RTE and DA sub-domains. Compared to the previous hybrid model, the coupled RTE–DA model does not neglect the backscattering between the RTE and DA sub-domains. In addition, whereas the previously proposed hybrid model was developed to eliminate the inaccuracy of the diffusion theory in the proximity of the source, the coupled RTE–DA model can also be used in other situations in which the assumptions of the DA not valid, e.g. near the domain boundary and within low-scattering and non-scattering regions. One example of a low-scattering region is the cerebrospinal fluid which surrounds the brain and fills the brain ventricles.

Let $\Omega \subset \mathbb{R}^n$, $n = 2 \text{ or } 3$ be the computational domain with boundary $\partial\Omega$, as illustrated in Figure 3.2 for the case $n = 2$. In the coupled RTE–DA model, the domain Ω is separated into two disjoint subsets Ω_{rte} and Ω_{da}. The RTE is used as the forward model in the sub-domain Ω_{rte} in which the assumptions of the DA are not valid. The RTE sub-domain is illustrated in Figure 3.2 with grey colour. The DA is used as the forward model in the sub-domain Ω_{da} which includes the remaining domain and is illustrated in Figure 3.2 with white colour. Let $\partial\Omega_{\text{rte}}$ be the boundary of the sub-domain Ω_{rte} and $\partial\Omega_{\text{da}}$ be the boundary of the sub-domain Ω_{da}. Furthermore, let $\Gamma = \partial\Omega_{\text{rte}} \cap \partial\Omega_{\text{da}}$ denote the interface that separates the sub-domains Ω_{rte} and Ω_{da}. The RTE and the DA are coupled through boundary conditions on the interface Γ which is marked in Figure 3.2 with dashed line. It should be noted that the interface Γ should be located within the region in which the assumptions of the DA are valid. Thus, for example in case of a highly scattering medium which contains a low-scattering or non-scattering region, Γ should be located inside the highly scattering region. The location of the interface

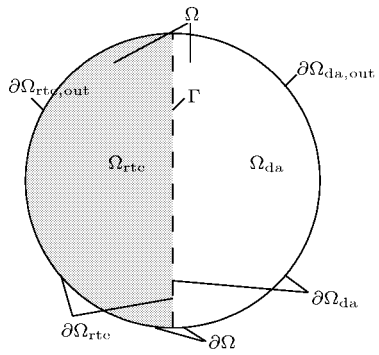

Figure 3.2: The domain Ω and the boundary $\partial\Omega$ (solid line). The RTE is used as the forward model in the sub-domain Ω_{rte} (grey colour) which has the boundary $\partial\Omega_{\mathrm{rte}}$. The DA is used as the forward model in the sub-domain Ω_{da} (white colour) which has the boundary $\partial\Omega_{\mathrm{da}}$. The sub-domains Ω_{rte} and Ω_{da} are separated by the interface Γ (dashed line) and they have the external boundaries $\partial\Omega_{\mathrm{rte,out}}$ and $\partial\Omega_{\mathrm{da,out}}$, respectively.

Γ can be, for example, determined by comparing the deviation of the angular distribution of the radiance from the first order approximation (3.16), similarly as in the case of the hybrid model. The location should be chosen such that the angular distribution of the radiance is "smooth" enough to be well approximated by the first order approximation. For the external boundaries we use the following notations $\partial\Omega_{\mathrm{rte,out}} = \partial\Omega_{\mathrm{rte}} \setminus \Gamma$ and $\partial\Omega_{\mathrm{da,out}} = \partial\Omega_{\mathrm{da}} \setminus \Gamma$.

The coupled RTE–DA model is derived by linking the RTE (3.2) and the DA (3.29) together with their boundary conditions (3.7) and (3.41). The two models are coupled on the interface Γ using the relations (3.9) and (3.16). The coupled RTE–DA model is of the form

$$\begin{aligned}
&\frac{\mathrm{i}\omega}{c}\phi(r,\hat{s}) + \hat{s}\cdot\nabla\phi(r,\hat{s}) + (\mu_s+\mu_a)\phi(r,\hat{s}) \\
&\quad = \mu_s \int_{S^{n-1}} \Theta(\hat{s}\cdot\hat{s}')\phi(r,\hat{s}')\mathrm{d}\hat{s}' + q(r,\hat{s}), \quad r\in\Omega_{\mathrm{rte}} \qquad (3.42)
\end{aligned}$$

$$\phi(r,\hat{s}) = \begin{cases} \phi_0(r,\hat{s}), & r\in\cup_j\varepsilon_j, \quad \hat{s}\cdot\hat{n}<0 \\ 0, & r\in\partial\Omega_{\mathrm{rte,out}}\setminus\cup_j\varepsilon_j, \quad \hat{s}\cdot\hat{n}<0 \end{cases} \qquad (3.43)$$

$$\phi(r,\hat{s}) = \frac{1}{|S^{n-1}|}\Phi(r) - \frac{n}{|S^{n-1}|}\hat{s}\cdot(\kappa\nabla\Phi(r)), \qquad r\in\Gamma \qquad (3.44)$$

$$-\nabla\cdot\kappa\nabla\Phi(r) + \mu_a\Phi(r) + \frac{\mathrm{i}\omega}{c}\Phi(r) = q_0(r), \qquad r\in\Omega_{\mathrm{da}} \qquad (3.45)$$

$$\Phi(r) + \frac{1}{2\gamma_n}\kappa A\frac{\partial\Phi(r)}{\partial\hat{n}} = \begin{cases} \frac{I_s}{\gamma_n}, & r\in\cup_j\varepsilon_j \\ 0, & r\in\partial\Omega_{\mathrm{da,out}}\setminus\cup_j\varepsilon_j \end{cases} \qquad (3.46)$$

$$\Phi(r) = \int_{S^{n-1}} \phi(r, \hat{s}) \mathrm{d}\hat{s}, \qquad r \in \Gamma. \tag{3.47}$$

In many cases it is logical to use the RTE as the forward model close to the sources and domain boundary and within low-scattering and non-scattering regions and the DA elsewhere in the domain. In that case, if the sources and the external boundary are modelled with the RTE, equation (3.46) vanishes and $\Gamma = \partial\Omega_{\mathrm{da}}$.

In the coupled RTE–DA model, the RTE and the DA are coupled though their boundary conditions and the equations are solved simultaneously. Thus, iterative mapping between the models is not required. The coupled RTE–DA model is a more general approach for light propagation than the hybrid approaches which are designed only to overcome the difficulties of the diffusion theory close to the sources or for media with non-scattering regions. The coupled RTE–DA model can be expected to describe light propagation accurately in various media with low-scattering and non-scattering regions. In addition, it can be expected to describe light transport accurately both close and farther from the source as well as close to the domain boundary.

Chapter IV

Numerical methods for light transport

The analytical solutions of the RTE and the DA are often restricted to certain specific geometries, see e.g. [12, 53, 160], and therefore their exploitability in optical tomography is limited. Therefore, in OT, the RTE and the DA are usually solved with numerical methods. The most often applied numerical methods are the finite difference method and the finite element method (FEM). The latter is generally regarded as more flexible when issues of implementing different boundary conditions and handling complex geometries are considered, and therefore it is most often chosen as the method for solving equations governing light transport in tissues. The FEM is also chosen as the numerical approach of this thesis. It is used to solve the RTE, the DA, and the proposed hybrid approaches.

Furthermore, in the thesis, Monte Carlo simulation is used as a reference method to verify the finite element (FE) calculations. Monte Carlo is a a statistical simulation method which is known to produce accurate estimates for light propagation in tissues. However, due to its statistical nature, it has the disadvantage of requiring long computation time. Therefore, Monte Carlo is usually used as a reference method for other approaches.

This chapter is organized as follows. First in Section 4.1, the variational formulation and the FE-approximation of the RTE are derived. Further, the FE-approximation of the RTE with the streamline diffusion modification is presented. In Section 4.2, the FE-approximation of the DA is derived. In Section 4.3, the variational formulation and the FE-approximation of the coupled RTE–DA model are derived and the FE-approximation of the coupled model with the streamline diffusion modification is presented. Finally in Section 4.4, Monte Carlo simulation is presented. The presentations in this chapter are based on the frequency-domain versions of the light transport models.

4.1 FE-approximation of the RTE

The numerical solution methods to the RTE can be divided into first order and second order techniques [2, 73]. In the second order techniques, an equivalent second order form of the RTE, of which the most well-known is the even-parity representation of the RTE, is derived [167]. In optical tomography, the first order

methods have been used for example in [71, 111, 144] and the second order methods have been used for example in [1, 24, 240].

In OT, a transport–backtransport algorithm to the time-domain RTE which uses the finite difference method for the spatial discretization and discrete ordinates for the angular discretization was developed in [71, 72]. A method to the steady-state RTE problem which uses the finite difference method for the spatial discretization and discrete ordinates for the angular discretization was introduced in [111] and the inverse problem was addressed in [140]. The forward and inverse problem were further investigated in [141, 144] and an algorithm using the finite element and discrete ordinates methods was developed in [1]. Further, a finite volume - discrete ordinates method was developed for the frequency-domain RTE in [191].

A method to the steady-state form of the RTE which uses the finite element method for the spatial discretization and the spherical harmonics approximation for the angular discretization was introduced in [24] and the approach was studied in media with different optical properties in [25]. The same method taken to P_3 approximation was studied in [124] and an adaptive P_N approach in which the order of the angular basis is varied according the local optical properties of the domain was introduced in [240].

In this study, the finite element method is used for the solution of RTE. Both the spatial and angular discretizations are implemented with the FEM. In the FEM, a variational formulation is derived for the original problem. Then, a finite dimensional approximation for the variational formulation is constructed using suitably chosen basis and test functions in the solution space. In this study, both the spatial and angular discretizations are implemented in piecewise linear bases. Similar approaches have been used for the discretization of the radiative transfer problem of ionizing radiation in [45, 229].

4.1.1 Variational formulation of the RTE

To obtain the variational formulation for the RTE, equation (3.2) is multiplied with a test function $v(r, \hat{s})$ and it is integrated over spatial domain Ω and angular directions S^{n-1}. This results into equation

$$\begin{aligned}
&\int_\Omega \int_{S^{n-1}} \frac{\mathrm{i}\omega}{c} \phi(r,\hat{s}) v(r,\hat{s}) \mathrm{d}\hat{s}\mathrm{d}r + \int_\Omega \int_{S^{n-1}} \hat{s}\cdot\nabla\phi(r,\hat{s}) v(r,\hat{s}) \mathrm{d}\hat{s}\mathrm{d}r \\
&+ \int_\Omega \int_{S^{n-1}} (\mu_s + \mu_a)\phi(r,\hat{s}) v(r,\hat{s}) \mathrm{d}\hat{s}\mathrm{d}r \\
&- \int_\Omega \int_{S^{n-1}} \mu_s \int_{S^{n-1}} \Theta(\hat{s}\cdot\hat{s}')\phi(r,\hat{s}') \mathrm{d}\hat{s}' v(r,\hat{s}) \mathrm{d}\hat{s}\mathrm{d}r \\
=&\int_\Omega \int_{S^{n-1}} q(r,\hat{s}) v(r,\hat{s}) \mathrm{d}\hat{s}\mathrm{d}r. \qquad (4.1)
\end{aligned}$$

Using the Green's formula [7], the second part on the left side of equation (4.1) can be written as

$$\begin{aligned}&\int_\Omega \int_{S^{n-1}} \hat{s}\cdot\nabla\phi(r,\hat{s})v(r,\hat{s})\mathrm{d}\hat{s}\mathrm{d}r\\ =&-\int_\Omega \int_{S^{n-1}} \hat{s}\cdot\nabla v(r,\hat{s})\phi(r,\hat{s})\mathrm{d}\hat{s}\mathrm{d}r+\int_{\partial\Omega}\int_{S^{n-1}}(\hat{s}\cdot\hat{n})\phi(r,\hat{s})v(r,\hat{s})\mathrm{d}\hat{s}\mathrm{d}S\end{aligned} \tag{4.2}$$

where the boundary integral term can further be written as [229]

$$\begin{aligned}&\int_{\partial\Omega}\int_{S^{n-1}}(\hat{s}\cdot\hat{n})\phi(r,\hat{s})v(r,\hat{s})\mathrm{d}\hat{s}\mathrm{d}S\\ =&\int_{\partial\Omega}\int_{S^{n-1}}\left((\hat{s}\cdot\hat{n})_+-(\hat{s}\cdot\hat{n})_-\right)\phi(r,\hat{s})v(r,\hat{s})\mathrm{d}\hat{s}\mathrm{d}S\end{aligned} \tag{4.3}$$

where $(\hat{s}\cdot\hat{n})_\pm$ denote the positive and negative parts of $(\hat{s}\cdot\hat{n})$, thus

$$(\hat{s}\cdot\hat{n})_+=\begin{cases}(\hat{s}\cdot\hat{n}), & (\hat{s}\cdot\hat{n})\geq 0\\ 0, & (\hat{s}\cdot\hat{n})<0\end{cases} \tag{4.4}$$

$$(\hat{s}\cdot\hat{n})_-=\begin{cases}0, & (\hat{s}\cdot\hat{n})\geq 0\\ -(\hat{s}\cdot\hat{n}), & (\hat{s}\cdot\hat{n})<0.\end{cases} \tag{4.5}$$

Using the boundary condition (3.7), equation (4.3) can further be written as

$$\begin{aligned}&\int_{\partial\Omega}\int_{S^{n-1}}\left((\hat{s}\cdot\hat{n})_+-(\hat{s}\cdot\hat{n})_-\right)\phi(r,\hat{s})v(r,\hat{s})\mathrm{d}\hat{s}\mathrm{d}S\\ =&\int_{\partial\Omega}\int_{S^{n-1}}(\hat{s}\cdot\hat{n})_+\phi(r,\hat{s})v(r,\hat{s})\mathrm{d}\hat{s}\mathrm{d}S\\ &-\int_{\partial\Omega}\int_{S^{n-1}}(\hat{s}\cdot\hat{n})_-\phi_0(r,\hat{s})v(r,\hat{s})\mathrm{d}\hat{s}\mathrm{d}S.\end{aligned} \tag{4.6}$$

Inserting equations (4.2)–(4.6) into equation (4.1), the variational formulation of the RTE is obtained. It is of the form

$$\begin{aligned}&\int_\Omega\int_{S^{n-1}}\frac{\mathrm{i}\omega}{c}\phi(r,\hat{s})v(r,\hat{s})\mathrm{d}\hat{s}\mathrm{d}r-\int_\Omega\int_{S^{n-1}}\hat{s}\cdot\nabla v(r,\hat{s})\phi(r,\hat{s})\mathrm{d}\hat{s}\mathrm{d}r\\ &+\int_{\partial\Omega}\int_{S^{n-1}}(\hat{s}\cdot\hat{n})_+\phi(r,\hat{s})v(r,\hat{s})\mathrm{d}\hat{s}\mathrm{d}S+\int_\Omega\int_{S^{n-1}}(\mu_s+\mu_a)\phi(r,\hat{s})v(r,\hat{s})\mathrm{d}\hat{s}\mathrm{d}r\\ &-\int_\Omega\int_{S^{n-1}}\mu_s\int_{S^{n-1}}\Theta(\hat{s}\cdot\hat{s}')\phi(r,\hat{s}')\mathrm{d}\hat{s}'v(r,\hat{s})\mathrm{d}\hat{s}\mathrm{d}r\\ =&\int_{\partial\Omega}\int_{S^{n-1}}(\hat{s}\cdot\hat{n})_-\phi_0(r,\hat{s})v(r,\hat{s})\mathrm{d}\hat{s}\mathrm{d}S+\int_\Omega\int_{S^{n-1}}q(r,\hat{s})v(r,\hat{s})\mathrm{d}\hat{s}\mathrm{d}r.\end{aligned} \tag{4.7}$$

4.1.2 FE-approximation of the RTE

To obtain the finite element approximation of the RTE, the solution $\phi(r,\hat{s})$ of the variational formulation (4.7) is approximated in a piecewise linear basis

$$\phi(r,\hat{s})\approx\phi^h(r,\hat{s})=\sum_{i=1}^{N_n}\sum_{\ell=1}^{N_a}\alpha_{i\ell}\psi_i(r)\psi_\ell(\hat{s}), \tag{4.8}$$

where $\psi_i(r)$ and $\psi_\ell(\hat{s})$ are the nodal basis functions of the spatial and angular finite element meshes, respectively, $\alpha_{i\ell}$ is the radiance in spatial nodal point i and "direction" ℓ, N_n is the number of spatial nodes, and N_a is the number of angular directions. The choice of the basis functions, equation (4.8), allows the separation of spatial and angular RTE discretizations, and thus the spatial and angular integrals can be calculated separately and connected using Kronecker product. Therefore, the approach is flexible, e.g. the amount of angular directions can be increased or decreased easily. Inserting approximation (4.8) into equation (4.7) and choosing the nodal basis functions $\psi_j(r)$ and $\psi_m(\hat{s})$ as the test functions, the following system of equations is obtained

$$
\begin{aligned}
&\int_\Omega \int_{S^{n-1}} \frac{\mathrm{i}\omega}{c} \sum_{i=1}^{N_n} \sum_{\ell=1}^{N_a} \alpha_{i\ell} \psi_i(r) \psi_\ell(\hat{s}) \psi_j(r) \psi_m(\hat{s}) \mathrm{d}\hat{s}\mathrm{d}r \\
&- \int_\Omega \int_{S^{n-1}} \hat{s} \cdot \nabla(\psi_j(r)\psi_m(\hat{s})) \sum_{i=1}^{N_n} \sum_{\ell=1}^{N_a} \alpha_{i\ell} \psi_i(r) \psi_\ell(\hat{s}) \mathrm{d}\hat{s}\mathrm{d}r \\
&+ \int_{\partial\Omega} \int_{S^{n-1}} (\hat{s} \cdot \hat{n})_+ \sum_{i=1}^{N_n} \sum_{\ell=1}^{N_a} \alpha_{i\ell} \psi_i(r) \psi_\ell(\hat{s}) \psi_j(r) \psi_m(\hat{s}) \mathrm{d}\hat{s}\mathrm{d}S \\
&+ \int_\Omega \int_{S^{n-1}} (\mu_s + \mu_a) \sum_{i=1}^{N_n} \sum_{\ell=1}^{N_a} \alpha_{i\ell} \psi_i(r) \psi_\ell(\hat{s}) \psi_j(r) \psi_m(\hat{s}) \mathrm{d}\hat{s}\mathrm{d}r \\
&- \int_\Omega \int_{S^{n-1}} \mu_s \int_{S^{n-1}} \Theta(\hat{s} \cdot \hat{s}') \sum_{i=1}^{N_n} \sum_{\ell=1}^{N_a} \alpha_{i\ell} \psi_i(r) \psi_\ell(\hat{s}') \mathrm{d}\hat{s}' \psi_j(r) \psi_m(\hat{s}) \mathrm{d}\hat{s}\mathrm{d}r \\
= &\int_{\partial\Omega} \int_{S^{n-1}} (\hat{s} \cdot \hat{n})_- \phi_0(r, \hat{s}) \psi_j(r) \psi_m(\hat{s}) \mathrm{d}\hat{s}\mathrm{d}S \\
&+ \int_\Omega \int_{S^{n-1}} q(r, \hat{s}) \psi_j(r) \psi_m(\hat{s}) \mathrm{d}\hat{s}\mathrm{d}r. \qquad (4.9)
\end{aligned}
$$

This can further be written in the form

$$
\begin{aligned}
&\frac{\mathrm{i}\omega}{c} \sum_{i=1}^{N_n} \sum_{\ell=1}^{N_a} \alpha_{i\ell} \int_\Omega \psi_i(r)\psi_j(r)\mathrm{d}r \int_{S^{n-1}} \psi_\ell(\hat{s})\psi_m(\hat{s})\mathrm{d}\hat{s} \\
&- \sum_{i=1}^{N_n} \sum_{\ell=1}^{N_a} \alpha_{i\ell} \int_\Omega \int_{S^{n-1}} \hat{s} \cdot \nabla\psi_j(r)\psi_m(\hat{s})\psi_\ell(\hat{s})\mathrm{d}\hat{s}\psi_i(r)\mathrm{d}r \\
&+ \sum_{i=1}^{N_n} \sum_{\ell=1}^{N_a} \alpha_{i\ell} \int_{\partial\Omega} \psi_i(r)\psi_j(r)\mathrm{d}S \int_{S^{n-1}} (\hat{s} \cdot \hat{n})_+ \psi_\ell(\hat{s})\psi_m(\hat{s})\mathrm{d}\hat{s} \\
&+ \sum_{i=1}^{N_n} \sum_{\ell=1}^{N_a} \alpha_{i\ell} \int_\Omega (\mu_s + \mu_a)\psi_i(r)\psi_j(r)\mathrm{d}r \int_{S^{n-1}} \psi_\ell(\hat{s})\psi_m(\hat{s})\mathrm{d}\hat{s}
\end{aligned}
$$

$$
\begin{aligned}
&- \sum_{i=1}^{N_n} \sum_{\ell=1}^{N_a} \alpha_{i\ell} \int_\Omega \mu_s \psi_i(r)\psi_j(r)\mathrm{d}r \int_{S^{n-1}} \int_{S^{n-1}} \Theta(\hat{s}\cdot\hat{s}')\psi_\ell(\hat{s}')\mathrm{d}\hat{s}'\psi_m(\hat{s})\mathrm{d}\hat{s} \\
&= \int_{\partial\Omega} \int_{S^{n-1}} (\hat{s}\cdot\hat{n})_- \phi_0(r,\hat{s})\psi_m(\hat{s})\mathrm{d}\hat{s}\psi_j(r)\mathrm{d}S \\
&\quad + \int_\Omega \int_{S^{n-1}} q(r,\hat{s})\psi_m(\hat{s})\mathrm{d}\hat{s}\psi_j(r)\mathrm{d}r
\end{aligned} \tag{4.10}
$$

The boundary source $\phi_0(r,\hat{s})$ can be approximated in the same basis as the solution and it is written as

$$
\phi_0(r,\hat{s}) \approx \sum_{i=1}^{N_n} \sum_{\ell=1}^{N_a} \psi^0_{i\ell}\psi_i(r)\psi_\ell(\hat{s}) \tag{4.11}
$$

where $\psi^0_{i\ell}$ is the source power in the node i in "direction" ℓ. Utilizing equations (4.10) and (4.11), the FE-approximation of the RTE can be written in the matrix form

$$
(A_0 + A_1 + A_2 + A_3 + A_4)\,\alpha = b_1\psi^0 + b_2 \tag{4.12}
$$

where $\alpha = (\alpha_{1,1},\ldots,\alpha_{1,N_a},\ldots,\alpha_{N_n,1}\ldots,\alpha_{N_n,N_a})^T \in \mathbb{C}^{N_nN_a}$ is the radiance in nodal points of the spatial and angular meshes. Vector $\psi^0 = (\psi^0_{1,1},\ldots,\psi^0_{N_n,N_a})^T \in \mathbb{R}^{N_nN_a}$ is the source strength vector having non-zero elements for spatial nodes $r_i \in \varepsilon_j \subset \partial\Omega$ such that $\psi^0_{i,\ell}$ is the source power at the node i in the "direction" ℓ. The components of the matrix equation (4.12) are of the form

$$
A_0(h,s) = \frac{\mathrm{i}\omega}{c} \int_\Omega \psi_i(r)\psi_j(r)\mathrm{d}r \int_{S^{n-1}} \psi_\ell(\hat{s})\psi_m(\hat{s})\mathrm{d}\hat{s} \tag{4.13}
$$

$$
A_1(h,s) = -\int_\Omega \int_{S^{n-1}} \hat{s}\cdot\nabla\psi_j(r)\psi_m(\hat{s})\psi_\ell(\hat{s})\mathrm{d}\hat{s}\psi_i(r)\mathrm{d}r \tag{4.14}
$$

$$
A_2(h,s) = \int_{\partial\Omega} \psi_i(r)\psi_j(r)\mathrm{d}S \int_{S^{n-1}} (\hat{s}\cdot\hat{n})_+\psi_\ell(\hat{s})\psi_m(\hat{s})\mathrm{d}\hat{s} \tag{4.15}
$$

$$
A_3(h,s) = \int_\Omega (\mu_s+\mu_a)\psi_i(r)\psi_j(r)\mathrm{d}r \int_{S^{n-1}} \psi_\ell(\hat{s})\psi_m(\hat{s})\mathrm{d}\hat{s} \tag{4.16}
$$

$$
A_4(h,s) = -\int_\Omega \mu_s\psi_i(r)\psi_j(r)\mathrm{d}r \int_{S^{n-1}} \int_{S^{n-1}} \Theta(\hat{s}\cdot\hat{s}')\psi_\ell(\hat{s}')\mathrm{d}\hat{s}'\psi_m(\hat{s})\mathrm{d}\hat{s} \tag{4.17}
$$

$$
b_1(h,s) = \int_{\partial\Omega} \psi_i(r)\psi_j(r)\mathrm{d}S \int_{S^{n-1}} (\hat{s}\cdot\hat{n})_-\psi_\ell(\hat{s})\psi_m(\hat{s})\mathrm{d}\hat{s} \tag{4.18}
$$

$$
b_2(h) = \int_\Omega \int_{S^{n-1}} q(r,\hat{s})\psi_m(\hat{s})\mathrm{d}\hat{s}\psi_j(r)\mathrm{d}r. \tag{4.19}
$$

where $h = N_a(j-1)+m$, $s = N_a(i-1)+\ell$ $(j,i = 1,\ldots,N_n,\ \ m,\ell = 1,\ldots,N_a,$ $h,s = 1,\ldots,N_nN_a)$.

4.1.3 FE-approximation of the RTE with the streamline diffusion modification

The ray effect may disturb the standard FE-techniques when solving the RTE [2, 151, 152, 154]. The ray effect can produce oscillating results [131] or it can visually be seen as "photon rays" radiating from the source into the direction of the discretization angels. To overcome these problems, the streamline diffusion modification can be utilized in the FE-solution of the RTE [131, 192]. In the streamline diffusion modification, the test function is of the form $(v + \delta\hat{s} \cdot \nabla v)$ instead of the standard method in which the test function is v. The parameter δ is the "smoothing" parameter which is a spatially varying constant that depends on the local absorption and scattering [131].

The FE-approximation of RTE with the streamline diffusion modification can be derived by following a similar procedure as described for the standard FE-method. The FE-approximation of the RTE with the streamline diffusion modification can be written in the form

$$(A_{0,\mathrm{sdm}} + A_{1,\mathrm{sdm}} + A_2 + A_{3,\mathrm{sdm}} + A_{4,\mathrm{sdm}})\,\alpha = b_1\psi^0 + b_2 \tag{4.20}$$

where A_2 is as in equation (4.15) and

$$\begin{aligned}
A_{0,\mathrm{sdm}}(h,s) =& \frac{\mathrm{i}\omega}{c}\left(\int_\Omega \psi_i(r)\psi_j(r)\mathrm{d}r \int_{S^{n-1}} \psi_\ell(\hat{s})\psi_m(\hat{s})\mathrm{d}\hat{s}\right. \\
&\left. + \int_\Omega \delta \int_{S^{n-1}} \hat{s}\cdot\nabla\psi_j(r)\psi_m(\hat{s})\psi_\ell(\hat{s})\mathrm{d}\hat{s}\psi_i(r)\mathrm{d}r\right) \qquad (4.21)\\
A_{1,\mathrm{sdm}}(h,s) =& -\int_\Omega \int_{S^{n-1}} \hat{s}\cdot\nabla\psi_j(r)\psi_m(\hat{s})\psi_\ell(\hat{s})\mathrm{d}\hat{s}\psi_i(r)\mathrm{d}r \\
&+ \int_\Omega \delta \int_{S^{n-1}} (\hat{s}\cdot\nabla\psi_j(r)\psi_m(\hat{s}))\,(\hat{s}\cdot\nabla\psi_i(r)\psi_\ell(\hat{s}))\,\mathrm{d}\hat{s}\mathrm{d}r \qquad (4.22)\\
A_{3,\mathrm{sdm}}(h,s) =& \int_\Omega (\mu_s+\mu_a)\psi_i(r)\psi_j(r)\mathrm{d}r \int_{S^{n-1}} \psi_\ell(\hat{s})\psi_m(\hat{s})\mathrm{d}\hat{s} \\
&+ \int_\Omega \delta(\mu_s+\mu_a) \int_{S^{n-1}} \hat{s}\cdot\nabla\psi_j(r)\psi_m(\hat{s})\psi_\ell(\hat{s})\mathrm{d}\hat{s}\psi_i(r)\mathrm{d}r \qquad (4.23)\\
A_{4,\mathrm{sdm}}(h,s) =& -\int_\Omega \mu_s\psi_i(r)\psi_j(r)\mathrm{d}r \int_{S^{n-1}}\int_{S^{n-1}} \Theta(\hat{s}\cdot\hat{s}')\psi_\ell(\hat{s}')\mathrm{d}\hat{s}'\psi_m(\hat{s})\mathrm{d}\hat{s} \\
&- \int_\Omega \delta\mu_s \int_{S^{n-1}} \hat{s}\cdot\nabla\psi_j(r)\psi_m(\hat{s}) \int_{S^{n-1}} \Theta(\hat{s}\cdot\hat{s}')\psi_\ell(\hat{s}')\mathrm{d}\hat{s}'\mathrm{d}\hat{s}\psi_i(r)\mathrm{d}r \\
& \qquad (4.24)
\end{aligned}$$

and b_1 and b_2 are as in equations (4.18) and (4.19), and ψ^0 is the source strength vector as in equation (4.12). Further, $h = N_a(j-1)+m$, $s = N_a(i-1)+\ell$ $(j,i = 1,\ldots,N_n,\ \ m,\ell = 1,\ldots,N_a,\ \ h,s = 1,\ldots,N_nN_a)$.

4.1.4 FE-solution of the RTE

The FE-solution of the RTE is obtained using equation (4.12), or when the streamline diffusion modification is applied, from equation (4.20). Thus, as a solution of the forward problem, the radiance α in nodal points of the spatial and angular discretizations is obtained. Furthermore, the photon density can be calculated from the radiance using equation (3.9), and the exitance, which is the measurable quantity on the boundary of the domain, can be calculated using equation (3.8).

The different data types in the frequency-domain can be computed from the exitance $\Gamma(r)$. As explained in Section 2.1.2, the data types in the frequency-domain are the amplitude $|\Gamma(r)|$ and phase shift $\arg(\Gamma(r))$, or the real $\mathrm{Re}(\Gamma(\mathrm{r}))$ and imaginary parts $\mathrm{Im}(\Gamma(\mathrm{r}))$, of the complex valued measurement $\Gamma(r)$. If the time-domain case is considered, various data types can be derived from the time-domain exitance $\Gamma(r)$ similarly as in equations (2.1)–(2.6). In that case, the time-dependent exitance $\Gamma(r)$ can be obtained from the FE-solution of the time-domain RTE (3.1).

4.2 FE-approximation of the DA

FE-model for the time-varying DA was introduced in [21]. It was later extended to address the topics of boundary conditions and source models [175, 211] and the frequency-domain case of the DA [209]. Since then, the FEM has been adopted by many groups [34, 106, 147, 179, 181] and nowadays it can be regarded as the most typical approach to numerically solve the DA.

Derivations of the FE-model for the DA have been presented in numerous papers, see e.g. [21, 145, 209]. Here, a short review in the frequency-domain is given according to [145]. First, a variational formulation is derived for the original problem, and then a finite dimensional approximation for the variational formulation is constructed.

To obtain the variational formulation for the DA, equation (3.29) is multiplied with test function $\Psi(r)$ and integrated over the domain Ω. This results into equation

$$\begin{aligned}&\int_\Omega -\Psi(r)\nabla\cdot\kappa\nabla\Phi(r)\mathrm{d}r+\int_\Omega \mu_a\Phi(r)\Psi(r)\mathrm{d}r+\int_\Omega \frac{\mathrm{i}\omega}{c}\Phi(r)\Psi(r)\mathrm{d}r\\ &=\int_\Omega q_0(r)\Psi(r)\mathrm{d}r.\end{aligned} \tag{4.25}$$

Using the Green's formula [7], we can write

$$\int_\Omega \Psi(r)\nabla\cdot\kappa\nabla\Phi(r)\mathrm{d}r=-\int_\Omega \kappa\nabla\Phi(r)\cdot\nabla\Psi(r)\mathrm{d}r+\int_{\partial\Omega}\kappa\left(\hat{n}\cdot\nabla\Phi(r)\right)\Psi(r)\mathrm{d}S \tag{4.26}$$

where the boundary integral term can be written, using the boundary condition (3.41), as

$$\int_{\partial\Omega}\kappa\left(\hat{n}\cdot\nabla\Phi(r)\right)\Psi(r)\mathrm{d}S=\int_{\partial\Omega}\frac{2I_s}{A}\Psi(r)\mathrm{d}S-\int_{\partial\Omega}\frac{2\gamma_n}{A}\Phi(r)\Psi(r)\mathrm{d}S. \tag{4.27}$$

Inserting equations (4.26) and (4.27) into equation (4.25), the variational formulation of the DA is obtained. It is of the form

$$\begin{aligned}&\int_\Omega \kappa\nabla\Phi(r)\cdot\nabla\Psi(r)\mathrm{d}r + \int_{\partial\Omega}\frac{2\gamma_n}{A}\Phi(r)\Psi(r)\mathrm{d}S + \int_\Omega \mu_a\Phi(r)\Psi(r)\mathrm{d}r\\ &+\int_\Omega \frac{\mathrm{i}\omega}{c}\Phi(r)\Psi(r)\mathrm{d}r\\ =&\int_\Omega q_0(r)\Psi(r)\mathrm{d}r + \int_{\partial\Omega}\frac{2I_s}{A}\Psi(r)\mathrm{d}S.\end{aligned} \tag{4.28}$$

To obtain the finite element approximation of the DA, the solution $\Phi(r)$ of the variational formulation (4.28) is approximated in a piecewise linear basis

$$\Phi(r)\approx\Phi^h(r)=\sum_{k=1}^{N}a_k\varphi_k(r) \tag{4.29}$$

where $\varphi_k(r)$ are the nodal basis functions, a_k is the photon density in nodal point k, and N is the number of nodal points. Inserting the approximation (4.29) into the variational formulation (4.28) and choosing the basis functions $\varphi_p(r)$ as test functions, the FE-approximation of the DA is obtained. It can be written in the matrix form

$$(K+C+R+Z)\,a=G+E \tag{4.30}$$

where

$$K(p,k)=\int_\Omega \kappa\nabla\varphi_k(r)\cdot\nabla\varphi_p(r)\mathrm{d}r \tag{4.31}$$

$$C(p,k)=\int_\Omega \mu_a\varphi_k(r)\varphi_p(r)\mathrm{d}r \tag{4.32}$$

$$R(p,k)=\int_{\partial\Omega}\frac{2\gamma_n}{A}\varphi_k(r)\varphi_p(r)\mathrm{d}S \tag{4.33}$$

$$Z(p,k)=\frac{\mathrm{i}\omega}{c}\int_\Omega \varphi_k(r)\varphi_p(r)\mathrm{d}r \tag{4.34}$$

where $k,p=1,\ldots,N$. The source vectors G and E depend on the source model that is used. Thus, in case of the collimated source model

$$G=0 \tag{4.35}$$

$$E(p)=\int_\Omega q_0\varphi_p(r)\mathrm{d}r \tag{4.36}$$

and in case of the diffuse source model

$$G(p)=\int_{\partial\Omega}\frac{2I_s}{A}\varphi_p(r)\mathrm{d}S \tag{4.37}$$

$$E=0. \tag{4.38}$$

The FE-solution of the DA is obtained using equation (4.30). Thus, as a solution of the forward problem, the photon density a in the nodal points of the FE-discretization is obtained. The exitance can be calculated in the measurement locations using equation (3.38).

Different data types can be computed from the exitance $\Gamma(r)$ in the frequency-domain similarly as described in Section 4.1.4 for the RTE. If the time-domain version of the DA is considered, different methods for solving the various data types without needing the evaluate the whole time-domain function $\Gamma(r)$ have been developed. These issues are discussed more detailed in [17, 204].

4.3 FE-approximation of the coupled RTE–DA model

In this thesis, the coupled RTE–DA model is numerically solved using the FEM. To obtain the FE-formulation of the coupled model, a variational formulation of the model is derived following the similar procedure as earlier for the RTE and the DA. Then, a finite dimensional approximation for the variational formulation is constructed using suitably chosen basis and test functions in the solution space.

4.3.1 Variational formulation of the coupled model

To obtain the variational formulation of the coupled model (3.42)–(3.47), equation (3.42) is multiplied with test function $v(r,\hat{s})$ and integrated over the RTE sub-domain Ω_{rte} and angular directions S^{n-1}, and equation (3.45) is multiplied with test function $\Psi(r)$ and integrated over the DA sub-domain Ω_{da}. The equations are coupled which results into equation

$$\begin{aligned}
&\int_{\Omega_{\text{rte}}}\int_{S^{n-1}} \frac{\mathrm{i}\omega}{c}\phi(r,\hat{s})v(r,\hat{s})\mathrm{d}\hat{s}\mathrm{d}r + \int_{\Omega_{\text{rte}}}\int_{S^{n-1}} \hat{s}\cdot\nabla\phi(r,\hat{s})v(r,\hat{s})\mathrm{d}\hat{s}\mathrm{d}r \\
&+ \int_{\Omega_{\text{rte}}}\int_{S^{n-1}} (\mu_s+\mu_a)\phi(r,\hat{s})v(r,\hat{s})\mathrm{d}\hat{s}\mathrm{d}r \\
&- \int_{\Omega_{\text{rte}}}\int_{S^{n-1}} \mu_s\int_{S^{n-1}} \Theta(\hat{s}\cdot\hat{s}')\phi(r,\hat{s}')\mathrm{d}\hat{s}'v(r,\hat{s})\mathrm{d}\hat{s}\mathrm{d}r \\
&- \int_{\Omega_{\text{da}}} \Psi(r)\nabla\cdot\kappa\nabla\Phi(r)\mathrm{d}r + \int_{\Omega_{\text{da}}} \mu_a\Phi(r)\Psi(r)\mathrm{d}r + \int_{\Omega_{\text{da}}} \frac{\mathrm{i}\omega}{c}\Phi(r)\Psi(r)\mathrm{d}r \\
=&\int_{\Omega_{\text{rte}}}\int_{S^{n-1}} q(r,\hat{s})v(r,\hat{s})\mathrm{d}\hat{s}\mathrm{d}r + \int_{\Omega_{\text{da}}} q_0(r)\Psi(r)\mathrm{d}r
\end{aligned} \tag{4.39}$$

Using the Green's formula, we obtain

$$\begin{aligned}
\int_{\Omega_{\text{rte}}}\int_{S^{n-1}} \hat{s}\cdot\nabla\phi(r,\hat{s})v(r,\hat{s})\mathrm{d}\hat{s}\mathrm{d}r &= -\int_{\Omega_{\text{rte}}}\int_{S^{n-1}} \hat{s}\cdot\nabla v(r,\hat{s})\phi(r,\hat{s})\mathrm{d}\hat{s}\mathrm{d}r \\
&+ \int_{\partial\Omega_{\text{rte}}}\int_{S^{n-1}} (\hat{s}\cdot\hat{n})\phi(r,\hat{s})v(r,\hat{s})\mathrm{d}\hat{s}\mathrm{d}S
\end{aligned} \tag{4.40}$$

and

$$\begin{aligned}&\int_{\Omega_{\mathrm{da}}} \Psi(r)\nabla\cdot\kappa\nabla\Phi(r)\mathrm{d}r\\ &= -\int_{\Omega_{\mathrm{da}}} \kappa\nabla\Phi(r)\cdot\nabla\Psi(r)\mathrm{d}r + \int_{\partial\Omega_{\mathrm{da}}} \kappa\left(\hat{n}\cdot\nabla\Phi(r)\right)\Psi(r)\mathrm{d}S. \end{aligned} \tag{4.41}$$

The boundary integral term in equation (4.40) can be written as

$$\begin{aligned}&\int_{\partial\Omega_{\mathrm{rte}}}\int_{S^{n-1}} (\hat{s}\cdot\hat{n})\phi(r,\hat{s})v(r,\hat{s})\mathrm{d}\hat{s}\mathrm{d}S\\ &= \int_{\partial\Omega_{\mathrm{rte}}}\int_{S^{n-1}} \left((\hat{s}\cdot\hat{n})_+ - (\hat{s}\cdot\hat{n})_-\right)\phi(r,\hat{s})v(r,\hat{s})\mathrm{d}\hat{s}\mathrm{d}S. \end{aligned} \tag{4.42}$$

It can further be separated into integrals over the external boundary $\partial\Omega_{\mathrm{rte,out}}$ and the interface boundary Γ, and utilizing the boundary conditions (3.43) and (3.44), equation (4.42) can further be written as

$$\begin{aligned}&\int_{\partial\Omega_{\mathrm{rte}}}\int_{S^{n-1}} \left((\hat{s}\cdot\hat{n})_+ - (\hat{s}\cdot\hat{n})_-\right)\phi(r,\hat{s})v(r,\hat{s})\mathrm{d}\hat{s}\mathrm{d}S\\ &= \int_{\partial\Omega_{\mathrm{rte}}}\int_{S^{n-1}} (\hat{s}\cdot\hat{n})_+\phi(r,\hat{s})v(r,\hat{s})\mathrm{d}\hat{s}\mathrm{d}S\\ &\quad - \int_{\partial\Omega_{\mathrm{rte,out}}}\int_{S^{n-1}} (\hat{s}\cdot\hat{n})_-\phi_0(r,\hat{s})v(r,\hat{s})\mathrm{d}\hat{s}\mathrm{d}S\\ &\quad - \int_{\Gamma}\int_{S^{n-1}} (\hat{s}\cdot\hat{n})_-\left(\frac{1}{|S^{n-1}|}\Phi(r) - \frac{n}{|S^{n-1}|}\hat{s}\cdot(\kappa\nabla\Phi(r))\right)v(r,\hat{s})\mathrm{d}\hat{s}\mathrm{d}S. \end{aligned} \tag{4.43}$$

Similarly, the boundary integral term in equation (4.41) can be separated into the integrals over the external boundary $\partial\Omega_{\mathrm{da,out}}$ and the interface boundary Γ, and utilizing the boundary conditions (3.46) and (3.47), it can be written as

$$\begin{aligned}&\int_{\partial\Omega_{\mathrm{da}}} \kappa\left(\hat{n}\cdot\nabla\Phi(r)\right)\Psi(r)\mathrm{d}S\\ &= \int_{\partial\Omega_{\mathrm{da,out}}} \kappa\left(\hat{n}\cdot\nabla\Phi(r)\right)\Psi(r)\mathrm{d}S + \int_{\Gamma} \kappa\left(\hat{n}\cdot\nabla\Phi(r)\right)\Psi(r)\mathrm{d}S\\ &= \int_{\partial\Omega_{\mathrm{da,out}}} \frac{2I_s}{A}\Psi(r)\mathrm{d}S - \int_{\partial\Omega_{\mathrm{da,out}}} \frac{2\gamma_n}{A}\Phi(r)\Psi(r)\mathrm{d}S\\ &\quad + \int_{\Gamma}\kappa\left(\hat{n}\cdot\nabla\int_{S^{n-1}}\phi(r,\hat{s})\mathrm{d}\hat{s}\right)\Psi(r)\mathrm{d}S. \end{aligned} \tag{4.44}$$

Inserting equations (4.40)–(4.44) into equation (4.39), the variational formulation is obtained. The variational formulation of the coupled RTE–DA model, equations (3.42)–(3.47), is of the form

$$\int_{\Omega_{\mathrm{rte}}}\int_{S^{n-1}} \frac{\mathrm{i}\omega}{c}\phi(r,\hat{s})v(r,\hat{s})\mathrm{d}\hat{s}\mathrm{d}r - \int_{\Omega_{\mathrm{rte}}}\int_{S^{n-1}} \hat{s}\cdot\nabla v(r,\hat{s})\phi(r,\hat{s})\mathrm{d}\hat{s}\mathrm{d}r$$

$$
\begin{aligned}
&+\int_{\partial\Omega_{\mathrm{rtc}}}\int_{S^{n-1}}(\hat{s}\cdot\hat{n})_{+}\phi(r,\hat{s})v(r,\hat{s})\mathrm{d}\hat{s}\mathrm{d}S\\
&-\int_{\Gamma}\int_{S^{n-1}}\frac{1}{|S^{n-1}|}(\hat{s}\cdot\hat{n})_{-}\Phi(r)v(r,\hat{s})\mathrm{d}\hat{s}\mathrm{d}S\\
&+\int_{\Gamma}\int_{S^{n-1}}\frac{n}{|S^{n-1}|}(\hat{s}\cdot\hat{n})_{-}\left(\hat{s}\cdot(\kappa\nabla\Phi(r))\right)v(r,\hat{s})\mathrm{d}\hat{s}\mathrm{d}S\\
&+\int_{\Omega_{\mathrm{rtc}}}\int_{S^{n-1}}(\mu_s+\mu_a)\phi(r,\hat{s})v(r,\hat{s})\mathrm{d}\hat{s}\mathrm{d}r\\
&-\int_{\Omega_{\mathrm{rtc}}}\int_{S^{n-1}}\mu_s\int_{S^{n-1}}\Theta(\hat{s}\cdot\hat{s}')\phi(r,\hat{s}')\mathrm{d}\hat{s}'v(r,\hat{s})\mathrm{d}\hat{s}\mathrm{d}r\\
&+\int_{\Omega_{\mathrm{da}}}\kappa\nabla\Phi(r)\cdot\nabla\Psi(r)\mathrm{d}r+\int_{\partial\Omega_{\mathrm{da,out}}}\frac{2\gamma_n}{A}\Phi(r)\Psi(r)\mathrm{d}S\\
&-\int_{\Gamma}\kappa\left(\hat{n}\cdot\nabla\left(\int_{S^{n-1}}\phi(r,\hat{s})\mathrm{d}\hat{s}\right)\right)\Psi(r)\mathrm{d}S+\int_{\Omega_{\mathrm{da}}}\mu_a\Phi(r)\Psi(r)\mathrm{d}r\\
&+\int_{\Omega_{\mathrm{da}}}\frac{\mathrm{i}\omega}{c}\Phi(r)\Psi(r)\mathrm{d}r\\
=&\int_{\partial\Omega_{\mathrm{rtc,out}}}\int_{S^{n-1}}(\hat{s}\cdot\hat{n})_{-}\phi_0(r,\hat{s})v(r,\hat{s})\mathrm{d}\hat{s}\mathrm{d}S+\int_{\Omega_{\mathrm{rtc}}}\int_{S^{n-1}}q(r,\hat{s})v(r,\hat{s})\mathrm{d}\hat{s}\mathrm{d}r\\
&+\int_{\partial\Omega_{\mathrm{da,out}}}\frac{2I_s}{A}\Psi(r)\mathrm{d}S+\int_{\Omega_{\mathrm{da}}}q_0(r)\Psi(r)\mathrm{d}r. \qquad (4.45)
\end{aligned}
$$

4.3.2 FE-approximation of the coupled model

To obtain the finite element approximation of the coupled RTE–DA model, the solutions $\phi(r,\hat{s})$ and $\Phi(r)$ of the variational formulation (4.45) are approximated in piecewise linear bases

$$\phi(r,\hat{s})\approx\phi^h(r,\hat{s})=\sum_{i=1}^{N_n}\sum_{\ell=1}^{N_a}\alpha_{i\ell}\psi_i(r)\psi_\ell(\hat{s}) \qquad (4.46)$$

$$\Phi(r)\approx\Phi^h(r)=\sum_{k=1}^{N}a_k\varphi_k(r), \qquad (4.47)$$

where $\psi_i(r)$ and $\psi_\ell(\hat{s})$ are the nodal basis functions of the spatial and angular FE-discretizations of the RTE, $\alpha_{i\ell}$ is the radiance in spatial nodal point i and "direction" ℓ, N_n is the number of spatial nodes, and N_a is the number of angular directions. Further, $\varphi_k(r)$ are the nodal basis functions of the FE-discretization of the DA, a_k is the photon density in nodal point k, and N is the number of nodal points. We note that the RTE and DA discretizations do not need to have the same nodal points on Γ but they can have if that is desirable. Inserting the approximations (4.46) and (4.47) into the variational formulation (4.45) and choosing the basis functions $\psi_j(r)$, $\psi_m(\hat{s})$, and $\varphi_p(r)$ as test functions, the following

system of equations in obtained

$$
\begin{aligned}
&\int_{\Omega_{\mathrm{rte}}}\int_{S^{n-1}}\frac{\mathrm{i}\omega}{c}\sum_{i=1}^{N_n}\sum_{\ell=1}^{N_a}\alpha_{i\ell}\psi_i(r)\psi_\ell(\hat{s})\psi_j(r)\psi_m(\hat{s})\mathrm{d}\hat{s}\mathrm{d}r\\
&-\int_{\Omega_{\mathrm{rte}}}\int_{S^{n-1}}\hat{s}\cdot\nabla(\psi_j(r)\psi_m(\hat{s}))\sum_{i=1}^{N_n}\sum_{\ell=1}^{N_a}\alpha_{i\ell}\psi_i(r)\psi_\ell(\hat{s})\mathrm{d}\hat{s}\mathrm{d}r\\
&+\int_{\partial\Omega_{\mathrm{rte}}}\int_{S^{n-1}}(\hat{s}\cdot\hat{n})_+\sum_{i=1}^{N_n}\sum_{\ell=1}^{N_a}\alpha_{i\ell}\psi_i(r)\psi_\ell(\hat{s})\psi_j(r)\psi_m(\hat{s})\mathrm{d}\hat{s}\mathrm{d}S\\
&-\int_{\Gamma}\int_{S^{n-1}}\frac{1}{|S^{n-1}|}(\hat{s}\cdot\hat{n})_-\sum_{k=1}^{N}a_k\varphi_k(r)\psi_j(r)\psi_m(\hat{s})\mathrm{d}\hat{s}\mathrm{d}S\\
&+\int_{\Gamma}\int_{S^{n-1}}\frac{n}{|S^{n-1}|}(\hat{s}\cdot\hat{n})_-\left(\hat{s}\cdot\left(\kappa\nabla\left(\sum_{k=1}^{N}a_k\varphi_k(r)\right)\right)\right)\psi_j(r)\psi_m(\hat{s})\mathrm{d}\hat{s}\mathrm{d}S\\
&+\int_{\Omega_{\mathrm{rte}}}\int_{S^{n-1}}(\mu_s+\mu_a)\sum_{i=1}^{N_n}\sum_{\ell=1}^{N_a}\alpha_{i\ell}\psi_i(r)\psi_\ell(\hat{s})\psi_j(r)\psi_m(\hat{s})\mathrm{d}\hat{s}\mathrm{d}r\\
&-\int_{\Omega_{\mathrm{rte}}}\int_{S^{n-1}}\mu_s\int_{S^{n-1}}\Theta(\hat{s}\cdot\hat{s}')\sum_{i=1}^{N_n}\sum_{\ell=1}^{N_a}\alpha_{i\ell}\psi_i(r)\psi_\ell(\hat{s}')\mathrm{d}\hat{s}'\psi_j(r)\psi_m(\hat{s})\mathrm{d}\hat{s}\mathrm{d}r\\
&+\int_{\Omega_{\mathrm{da}}}\kappa\nabla(\sum_{k=1}^{N}a_k\varphi_k(r))\cdot\nabla\varphi_p(r)\mathrm{d}r+\int_{\partial\Omega_{\mathrm{da,out}}}\frac{2\gamma_n}{A}\sum_{k=1}^{N}a_k\varphi_k(r)\varphi_p(r)\mathrm{d}S\\
&-\int_{\Gamma}\kappa\left(\hat{n}\cdot\nabla\left(\int_{S^{n-1}}\sum_{i=1}^{N_n}\sum_{\ell=1}^{N_a}\alpha_{i\ell}\psi_i(r)\psi_\ell(\hat{s})\mathrm{d}\hat{s}\right)\right)\varphi_p(r)\mathrm{d}S\\
&+\int_{\Omega_{\mathrm{da}}}\mu_a\sum_{k=1}^{N}a_k\varphi_k(r)\varphi_p(r)\mathrm{d}r+\int_{\Omega_{\mathrm{da}}}\frac{\mathrm{i}\omega}{c}\sum_{k=1}^{N}a_k\varphi_k(r)\varphi_p(r)\mathrm{d}r\\
=&\int_{\partial\Omega_{\mathrm{rte,out}}}\int_{S^{n-1}}(\hat{s}\cdot\hat{n})_-\phi_0(r,\hat{s})\psi_j(r)\psi_m(\hat{s})\mathrm{d}\hat{s}\mathrm{d}S\\
&+\int_{\Omega_{\mathrm{rte}}}\int_{S^{n-1}}q(r,\hat{s})\psi_j(r)\psi_m(\hat{s})\mathrm{d}\hat{s}\mathrm{d}r\\
&+\int_{\partial\Omega_{\mathrm{da,out}}}\frac{2I_s}{A}\varphi_p(r)\mathrm{d}S+\int_{\Omega_{\mathrm{da}}}q_0(r)\varphi_p(r)\mathrm{d}r.
\end{aligned}
\tag{4.48}
$$

This can further be written in the form

$$
\begin{aligned}
&\frac{\mathrm{i}\omega}{c}\sum_{i=1}^{N_n}\sum_{\ell=1}^{N_a}\alpha_{i\ell}\int_{\Omega_{\mathrm{rte}}}\psi_i(r)\psi_j(r)\mathrm{d}r\int_{S^{n-1}}\psi_\ell(\hat{s})\psi_m(\hat{s})\mathrm{d}\hat{s}\\
&-\sum_{i=1}^{N_n}\sum_{\ell=1}^{N_a}\alpha_{i\ell}\int_{\Omega_{\mathrm{rte}}}\int_{S^{n-1}}\hat{s}\cdot\nabla\psi_j(r)\psi_m(\hat{s})\psi_\ell(\hat{s})\mathrm{d}\hat{s}\psi_i(r)\mathrm{d}r
\end{aligned}
$$

$$
\begin{aligned}
&+\sum_{i=1}^{N_n}\sum_{\ell=1}^{N_a}\alpha_{i\ell}\int_{\partial\Omega_{\mathrm{rte}}}\psi_i(r)\psi_j(r)\mathrm{d}S\int_{S^{n-1}}(\hat{s}\cdot\hat{n})_+\psi_\ell(\hat{s})\psi_m(\hat{s})\mathrm{d}\hat{s}\\
&-\frac{1}{|S^{n-1}|}\sum_{k=1}^{N}a_k\int_\Gamma\varphi_k(r)\psi_j(r)\mathrm{d}S\int_{S^{n-1}}(\hat{s}\cdot\hat{n})_-\psi_m(\hat{s})\mathrm{d}\hat{s}\\
&+\frac{n}{|S^{n-1}|}\sum_{k=1}^{N}a_k\int_\Gamma\kappa\int_{S^{n-1}}(\hat{s}\cdot\hat{n})_-\left(\hat{s}\cdot\nabla\varphi_k(r)\right)\psi_m(\hat{s})\mathrm{d}\hat{s}\psi_j(r)\mathrm{d}S\\
&+\sum_{i=1}^{N_n}\sum_{\ell=1}^{N_a}\alpha_{i\ell}\int_{\Omega_{\mathrm{rte}}}(\mu_s+\mu_a)\psi_i(r)\psi_j(r)\mathrm{d}r\int_{S^{n-1}}\psi_\ell(\hat{s})\psi_m(\hat{s})\mathrm{d}\hat{s}\\
&-\sum_{i=1}^{N_n}\sum_{\ell=1}^{N_a}\alpha_{i\ell}\int_{\Omega_{\mathrm{rte}}}\mu_s\psi_i(r)\psi_j(r)\mathrm{d}r\int_{S^{n-1}}\int_{S^{n-1}}\Theta(\hat{s}\cdot\hat{s}')\psi_\ell(\hat{s}')\mathrm{d}\hat{s}'\psi_m(\hat{s})\mathrm{d}\hat{s}\\
&+\sum_{k=1}^{N}a_k\int_{\Omega_{\mathrm{da}}}\kappa\nabla\varphi_k(r)\cdot\nabla\varphi_p(r)\mathrm{d}r+\sum_{k=1}^{N}a_k\int_{\partial\Omega_{\mathrm{da,out}}}\frac{2\gamma_n}{A}\varphi_k(r)\varphi_p(r)\mathrm{d}S\\
&-\sum_{i=1}^{N_n}\sum_{\ell=1}^{N_a}\alpha_{i\ell}\int_\Gamma\kappa\left(\hat{n}\cdot\nabla\psi_i(r)\right)\varphi_p(r)\mathrm{d}S\int_{S^{n-1}}\psi_\ell(\hat{s})\mathrm{d}\hat{s}\\
&+\sum_{k=1}^{N}a_k\int_{\Omega_{\mathrm{da}}}\mu_a\varphi_k(r)\varphi_p(r)\mathrm{d}r+\frac{\mathrm{i}\omega}{c}\sum_{k=1}^{N}a_k\int_{\Omega_{\mathrm{da}}}\varphi_k(r)\varphi_p(r)\mathrm{d}r\\
=&\int_{\partial\Omega_{\mathrm{rte,out}}}\int_{S^{n-1}}(\hat{s}\cdot\hat{n})_-\phi_0(r,\hat{s})\psi_j(r)\psi_m(\hat{s})\mathrm{d}\hat{s}\mathrm{d}S\\
&+\int_{\Omega_{\mathrm{rte}}}\int_{S^{n-1}}q(r,\hat{s})\psi_m(\hat{s})\mathrm{d}\hat{s}\psi_j(r)\mathrm{d}r\\
&+\int_{\partial\Omega_{\mathrm{da,out}}}\frac{2I_s}{A}\varphi_p(r)\mathrm{d}S+\int_{\Omega_{\mathrm{da}}}q_0(r)\varphi_p(r)\mathrm{d}r.
\end{aligned}
\tag{4.49}
$$

The RTE boundary source $\phi_0(r,\hat{s})$ can be approximated in the same basis as the solution and it is written as in equation (4.11). The FE-approximation of the coupled RTE–DA model can be written in the block-matrix form

$$
\begin{pmatrix} A_{\mathrm{rte}} & D \\ F & A_{\mathrm{da}} \end{pmatrix}\begin{pmatrix}\alpha\\ a\end{pmatrix}=\begin{pmatrix} b_{\mathrm{rte}}\\ b_{\mathrm{da}}\end{pmatrix}, \tag{4.50}
$$

where $\alpha=(\alpha_{1,1},\ldots,\alpha_{1,N_a},\ldots,\alpha_{N_n,1}\ldots,\alpha_{N_n,N_a})^T\in\mathbb{C}^{N_nN_a}$ is the radiance in nodal points of the FE-mesh in Ω_{rte} and $a=(a_1,\ldots,a_N)^T\in\mathbb{C}^N$ is the photon density in nodal points of the FE-mesh in Ω_{da}. Further, A_{rte} is a block which contains the FE-approximation of the RTE, A_{da} is a block which contains the FE-approximation of the DA, and D and F are matrices which contain the coupling connections on the interface Γ. The components of the matrix equation (4.50) are of the following form. The block A_{rte} is of the form

$$
A_{\mathrm{rte}}=A_0+A_1+A_2+A_3+A_4, \tag{4.51}
$$

where A_0, A_1, A_2, A_3, and A_4 are as in equations (4.13)–(4.17), where $\Omega = \Omega_{\text{rte}}$ and $\partial\Omega = \partial\Omega_{\text{rte}}$. The block A_{da} is of the form

$$A_{\text{da}} = K + C + R + Z, \tag{4.52}$$

where K, C, R, and Z are as in equations (4.31)–(4.34) where $\Omega = \Omega_{\text{da}}$ and $\partial\Omega = \partial\Omega_{\text{da,out}}$. Furthermore, the matrix D which contains the boundary conditions for the RTE on the interface Γ is of the form

$$\begin{aligned} D(h,k) = &- \frac{1}{|S^{n-1}|} \int_\Gamma \varphi_k(r)\psi_j(r)\mathrm{d}S \int_{S^{n-1}} (\hat{s}\cdot\hat{n})_- \psi_m(\hat{s})\mathrm{d}\hat{s} \\ &+ \frac{n}{|S^{n-1}|} \int_\Gamma \kappa \int_{S^{n-1}} (\hat{s}\cdot\hat{n})_- \left(\hat{s}\cdot\nabla\varphi_k(r)\right) \psi_m(\hat{s})\mathrm{d}\hat{s}\psi_j(r)\mathrm{d}S, \end{aligned} \tag{4.53}$$

where $h = N_a(j-1)+m$, $(j = 1,\ldots,N_n, m = 1,\ldots,N_a)$ and $k = 1,\ldots,N$. The matrix F which contains the boundary conditions for the DA on the interface Γ is of the form

$$F(p,s) = -\int_\Gamma \kappa\left(\hat{n}\cdot\nabla\psi_i(r)\right)\varphi_p(r)\mathrm{d}S \int_{S^{n-1}} \psi_\ell(\hat{s})\mathrm{d}\hat{s}, \tag{4.54}$$

where $s = N_a(i-1)+\ell$, $(i = 1,\ldots,N_n, \ell = 1,\ldots,N_a)$ and $p = 1,\ldots,N$. If the source is located in the RTE sub-domain Ω_{rte}, the source vector $b_{\text{rte}} \in \mathbb{R}^{N_n N_a}$ is of the form

$$b_{\text{rte}} = b_1\psi^0 + b_2, \tag{4.55}$$

where $\psi^0 = (\psi^0_{1,1},\ldots,\psi^0_{N_n,N_a})^T \in \mathbb{R}^{N_n N_a}$ is the source strength vector having non-zero elements for spatial nodes $r_i \in \varepsilon_j \subset \partial\Omega_{\text{rte,out}}$ such that $\psi^0_{i,\ell}$ is the source power at the node i in the "direction" ℓ. Further the matrix b_1 and the vector b_2 are as in equations (4.18) and (4.19), where $\Omega = \Omega_{\text{rte}}$ and $\partial\Omega = \partial\Omega_{\text{rte,out}}$. On the other hand, if the source is located in the DA sub-domain Ω_{da}, the DA source vector $b_{\text{da}} \in \mathbb{R}^N$ is of the form

$$b_{\text{da}} = G + E \tag{4.56}$$

where the source vectors G and E depend on the source model that is used. Thus, they are either of the form (4.35)–(4.36) or of the form (4.37)–(4.38) where $\Omega = \Omega_{\text{da}}$ and $\partial\Omega = \partial\Omega_{\text{da,out}}$. In many cases, the sources are modelled with the RTE, and thus $b_{\text{da}} = 0$.

4.3.3 FE-approximation of the coupled model with the streamline diffusion modification

The FE-solution of the coupled model can suffer from the ray effect similarly as the FE-solution of the RTE in whole domain. To overcome the ray effect problem, the streamline diffusion modification can be utilized in the FE-solution of the coupled model as well. The FE-approximation of coupled RTE–DA model with the streamline diffusion modification can be derived to have the matrix form

$$\begin{pmatrix} A_{\text{rte,sdm}} & D \\ F & A_{\text{da}} \end{pmatrix} \begin{pmatrix} \alpha \\ a \end{pmatrix} = \begin{pmatrix} b_{\text{rte}} \\ b_{\text{da}} \end{pmatrix}, \tag{4.57}$$

where α is the radiance in nodal points of the FE-mesh in Ω_{rte} and a is the photon density in nodal points of the FE-mesh in Ω_{da} as in equation (4.50). The matrix $A_{\text{rte,sdm}}$ is of the form

$$A_{\text{rte,sdm}} = A_{0,\text{sdm}} + A_{1,\text{sdm}} + A_2 + A_{3,\text{sdm}} + A_{4,\text{sdm}} \tag{4.58}$$

where A_2, $A_{0,\text{sdm}}$, $A_{1,\text{sdm}}$, $A_{3,\text{sdm}}$, and $A_{4,\text{sdm}}$ are as in equations (4.15) and (4.21)–(4.24) where $\Omega = \Omega_{\text{rte}}$ and $\partial\Omega = \partial\Omega_{\text{rte}}$. Further, the matrix A_{da} is as in equation (4.52), and the matrices D and F, which contain the coupling connections on Γ, are as in equations (4.53) and (4.54). The source vectors b_{rte} and b_{da} are as in equations (4.55) and (4.56).

4.3.4 FE-solution of the coupled model

The FE-solution of the coupled RTE–DA model is obtained using equation (4.50), or when the streamline diffusion modification is applied, using equation (4.57). Thus, as a solution of the forward problem, the radiance α in the nodal points of the spatial and angular discretizations of the RTE and the photon density a in the nodal points of the FE-discretization of the DA are obtained.

The photon density in the RTE sub-domain Ω_{rte} can be calculated from the radiance using equation (3.9). The exitance can be calculated using equation (3.8) or (3.38) depending whether the measurement position is located in the RTE or DA sub-domain.

4.4 Comparison of numerical solutions

An alternative to the deterministic methods, the stochastic (or statistical) modelling techniques can be used to model light transport is medium. The two statistical approaches that have been applied in OT are the random walk theory and Monte Carlo simulation [14, 89]. Monte Carlo is the most often used statistical technique in OT. It is often used as a reference method and other solutions are compared against it. The accuracy of the Monte Carlo simulation depends on the number of simulated photons. In this thesis, the FE-solutions of the light transport models are compared with the results of Monte Carlo simulations.

4.4.1 Monte Carlo simulation

Monte Carlo is a statistical simulation method in which paths of photons are traced as the photons are scattered and absorbed within the medium [15, 129]. Monte Carlo is known to produce accurate estimates for light propagation in tissues and many Monte Carlo codes simulating light transport in tissues have been published, see e.g. [39, 109, 118, 188, 230, 237]. However, due to its statistical nature, Monte Carlo has the disadvantage of requiring long computation time. Therefore, Monte Carlo is usually used as a reference method for other approaches.

The Monte Carlo code used here is a similar to the anisotropic codes described in [105, 109]. In this study, a two-dimensional (2D) situation is considered and the medium is isotropic. The photon packet method [188] is used. The Monte

Carlo code proceeds in the following way. First, a photon packet is launched into the domain at the source position with an initial weight w. The step size L of the photon packet is calculated using exponential probability density function. If the scattering coefficient changes during the step size, (i.e. the photon packet crosses an internal boundary between regions with different scattering properties) the remainder of the step size is renormalized by $\mu_s^{\text{old}}/\mu_s^{\text{new}}$ where μ_s^{old} and μ_s^{new} are the old and new scattering coefficients, respectively. At each step, a part of the packet is absorbed. The absorption is handled by reducing the weight of the photon packet by

$$w' = we^{-\mu_a l} \tag{4.59}$$

where w and w' is the weight of the photon packet before and after absorption, respectively, and l is the length travelled by the photon in a medium with an absorption coefficient μ_a. After a scattering event, a new direction is drawn using the Henyey–Greenstein scattering function. Thus, in 2D case, if the photon direction before the scattering event is $\hat{s}' = (\cos\theta', \sin\theta')$, the new direction $\hat{s} = (\cos\theta, \sin\theta)$ is obtained by

$$\theta = \theta' + \tilde{\theta} \tag{4.60}$$

where

$$\tilde{\theta} = 2\tan^{-1}\left(\frac{1-g}{1+g}\tan(\pi\xi)\right) \tag{4.61}$$

where g is the scattering shape parameter as in equation (3.5), and ξ is a random variable uniformly distributed between zero and one. Thus, if $g = 0$ the scattering angle $\tilde{\theta}$ is obtained from a uniform distribution from 0 to 2π. The photon packet propagation is continued until the packet either escapes the domain or the weight falls below a predefined minimum.

In this thesis, two types of Monte Carlo simulations are used. In the other approach, the medium is discretized and the weight of the photon packet is saved in each pixel which it crosses. In the other approach, the weight of the photon packet is only saved if the photon packet escapes the domain. Thus it contributes to the boundary data (exitance).

Chapter V

Light transport simulations

In this chapter, light propagation is simulated using the different light transport models described in Chapter 3. The RTE and DA are solved with the finite element method in different domains with various optical properties. Furthermore, the two proposed hybrid approaches, namely the hybrid model and the coupled RTE–DA model, are tested with simulations in different situations. The FE-computations are performed as described in Chapter 4.

The FE-solutions of the DA and the proposed hybrid approaches are compared against the FE-solution of the RTE. The RTE is widely accepted as an accurate model for light propagation in tissues and therefore it is chosen as a reference. The results are also compared with the results of the Monte Carlo simulations. The Monte Carlo simulations are performed as described in Section 4.4.

This chapter is organized as follows. The FE-solutions of the RTE and the DA are investigated in different media with various optical properties in Section 5.1. Further, the hybrid model is tested with simulations in highly scattering medium in Section 5.2. Finally, the performance of the coupled RTE–DA model is investigated in highly scattering medium, in highly scattering media with low-scattering and non-scattering regions, and in a realistic head geometry with tissue-like optical properties in Section 5.3.

5.1 FE-solutions of the RTE and the DA

5.1.1 FE-solution of the RTE in a slab

The performance of the FE-solution of the RTE was tested with simulations in a 2D slab with different scattering properties. The size of the slab was $15\,\mathrm{mm} \times 50\,\mathrm{mm}$ and the source was located at the centre of the upper long edge. The absorption coefficient of the slab was $\mu_a = 0.1\,\mathrm{mm}^{-1}$ and three different scattering values were $\mu_s = 5\,\mathrm{mm}^{-1}$, $\mu_s = 0.5\,\mathrm{mm}^{-1}$, and $\mu_s = 0.05\,\mathrm{mm}^{-1}$. The scattering shape parameter of the Henyey–Greenstein phase function (3.5) was $g = 0.558$. The continuous wave situation was considered, and thus $\omega = 0$. The refractive indices of the medium and the surrounding medium were chosen as $n_{\mathrm{in}} = 1.4$.

Models

The RTE was solved with the FEM with and without the streamline diffusion modification. The standard FE-solution of the RTE was computed as described in Section 4.1.2 using equation (4.12), and the FE-solution with the streamline diffusion modification was computed as described in Section 4.1.3 using equation (4.20). The "smoothing" parameter in the streamline diffusion modification was chosen as $\delta = \min\{\frac{1}{(\mu_a+\mu_s)}, \frac{25}{(\mu_a+\mu_s)r_j}\}$, where r_j is the distance from the source to the jth element. The FE-mesh for the spatial discretization of the RTE contained 1778 nodal points and 3435 triangular elements. In angular discretization, 32 directions were used. As a solution of the forward problem, the radiance in the nodal points of the FE-mesh was obtained. The photon density was computed from the radiance using equation (3.9). Moreover, the exitance was solved on the boundary locations on the opposite side to the source using equation (3.8).

The FE-solutions were compared with the results of Monte Carlo simulation. The Monte Carlo simulation was performed as described in Section 4.4.1 with the weight of the photon packet saved in each pixel which is crossed. Thus, as a result of the Monte Carlo simulation, the photon density inside the discretized domain and the exitance on the boundary of the domain were obtained.

Results and discussion

The logarithms of photon densities within the slab are shown in Figure 5.1 in which the FE-solutions without the streamline diffusion modification are shown on the left and the FE-solutions with the streamline diffusion modification are shown on the right. The exitances on the boundary opposite to the source are shown in Figure 5.2 which shows the FE-solutions of the RTE with and without the streamline diffusion modification and the results of Monte Carlo simulation. The results in Figure 5.2 were scaled according to maximum exitance value on the boundary.

The results show that the FE-solutions of the RTE with the streamline diffusion modification correspond well with the results of the Monte Carlo simulation in all of the tests. Thus, the FEM can be used to accurately solve the RTE with different optical properties. The FE-solutions of the RTE without the streamline diffusion modification, however, show oscillating results in cases of highly scattering and low-scattering medium. Within the low-scattering medium, the oscillations seem to follow the directions of the angular FE-discretization. This effect is known as the ray effect. The results indicate that the FE-solution of the RTE is sensitive to the mesh density, and without the streamline diffusion modification, too coarse or too dense discretizations can give unstable results.

5.1.2 Validity of the DA

The validity of the DA was tested with simulations in a medium with different scattering properties. The simulations were carried out in a 2D circular domain with the radius of 25 mm. The centre of the circle was located at the origin and the light source was located at $\begin{pmatrix}-25 & 0\end{pmatrix}$. Different scattering properties were

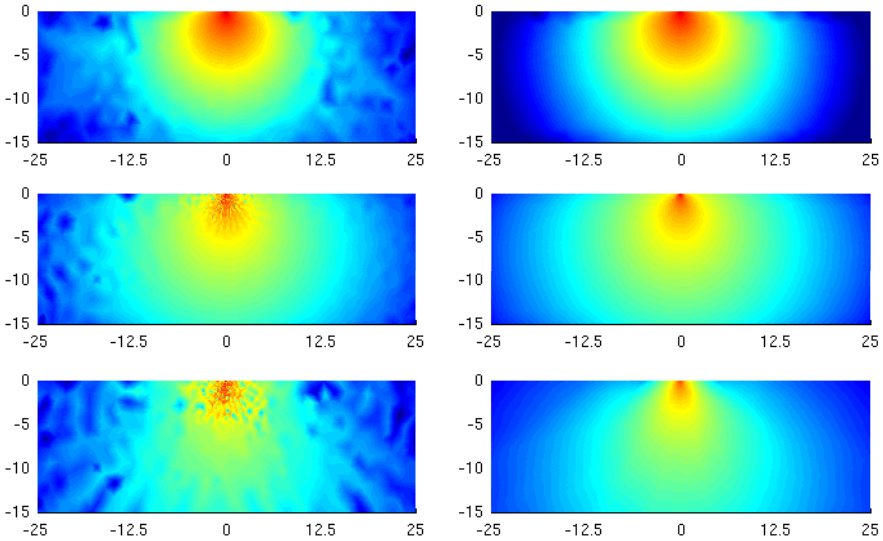

Figure 5.1: Logarithms of photon densities within a slab. On the left, there are the FE-solutions of the RTE without the streamline diffusion modification, and on the right, the same with the streamline diffusion modification. The scattering coefficients were $\mu_s = 5\,\mathrm{mm}^{-1}$, $\mu_s = 0.5\,\mathrm{mm}^{-1}$, $\mu_s = 0.05\,\mathrm{mm}^{-1}$ (images from top to bottom in the respective order).

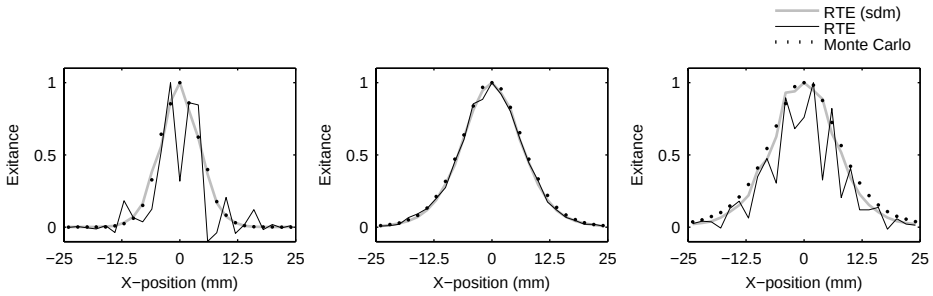

Figure 5.2: Exitances on the slab boundary opposite to the source. Figure shows the FE-solutions of the RTE with and without the streamline diffusion modification and the results of Monte Carlo simulation. The scattering coefficients were $\mu_s = 5\,\mathrm{mm}^{-1}$, $\mu_s = 0.5\,\mathrm{mm}^{-1}$, and $\mu_s = 0.05\,\mathrm{mm}^{-1}$ (images from left to right in the respective order).

Table 5.1: The absorption coefficient μ_a, the scattering coefficient μ_s, the scattering shape parameter g, and the reduced scattering coefficient μ_s' used in the simulations.

	$\mu_a(\text{mm}^{-1})$	$\mu_s(\text{mm}^{-1})$	g	$\mu_s'(\text{mm}^{-1})$
1.A:	0.025	2	0	2
1.B:	0.025	1	0	1
1.C:	0.025	0.2	0	0.2
2.A:	0.025	2	0.2	1.6
2.B:	0.025	2	0.5	1
2.C:	0.025	2	0.8	0.4

investigated. The absorption and scattering coefficients of the medium and the scattering shape parameter of the Henyey–Greenstein phase function (3.5) used in simulations are given in Table 5.1. In simulations 1.A–1.C, the scattering coefficient μ_s was changed and the scattering probability was a uniform distribution ($g = 0$). In simulations 2.A–2.C, the scattering coefficient was constant and the shape of the scattering probability was varied from almost a uniform distribution into forward peaked by changing the value of the scattering shape parameter g. The continuous wave situation was considered, thus $\omega = 0$. The refractive indices of the medium and the surrounding medium were chosen as $n_{\text{in}} = 1.4$. Thus, it was assumed that no reflection effects occurred on the boundary and the reflection parameter was $A = 1$ when solving the DA.

MODELS

The FE-solution of the DA was computed as described in Section 4.2 using equation (4.30). The light source was modelled with the diffuse source model (4.37). The FE-discretization consisted of 3703 nodal points and 7230 triangular elements. As a solution of the forward problem, the photon density in the nodal points of the FE-discretization was obtained. The exitance was solved on the domain boundary using equation (3.38).

For comparison, the FE-solution of the RTE was computed. The FE-calculations were performed as described in Section 4.1 with the streamline diffusion modification being applied. The FE-solutions of the RTE were computed in the same spatial mesh as the FE-solutions of the DA. The angular discretization of the RTE consisted of 16 (simulations 1.A–1.C and 2.A), 32 (simulation 2.B), and 48 (simulation 2.C) angular directions. The FE-solutions of the DA and the RTE were compared with the results of Monte Carlo simulation. The Monte Carlo simulations were performed as described in Section 4.4.1 with the weight of the photon packet saved on the boundary of the domain.

The quantities that were investigated were the photon density inside the domain and the exitance, equations (3.8) and (3.38), on the boundary of the domain.

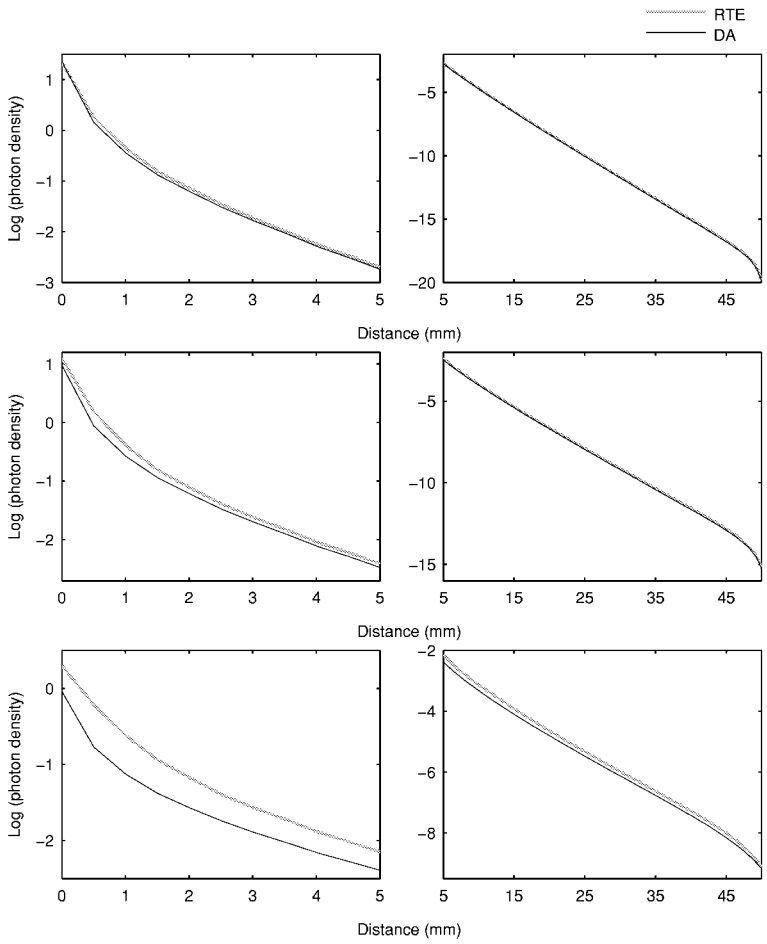

Figure 5.3: Logarithm of photon density against the distance from the source in a circular domain. On the left, there are the distances from the source site to 5 mm, and on the right, there are the distances from 5 mm to 50 mm. The scattering coefficients were $\mu_s = 2\,\mathrm{mm}^{-1}$ (case 1.A), $\mu_s = 1\,\mathrm{mm}^{-1}$ (case 1.B), and $\mu_s = 0.2\,\mathrm{mm}^{-1}$ (case 1.C) (images from top to bottom in the respective order).

Both the photon density within the domain and exitance on the boundary of the domain were obtained from the results of the FE-calculations. As the result of the Monte Carlo simulation, the exitance on the boundary of the domain was obtained.

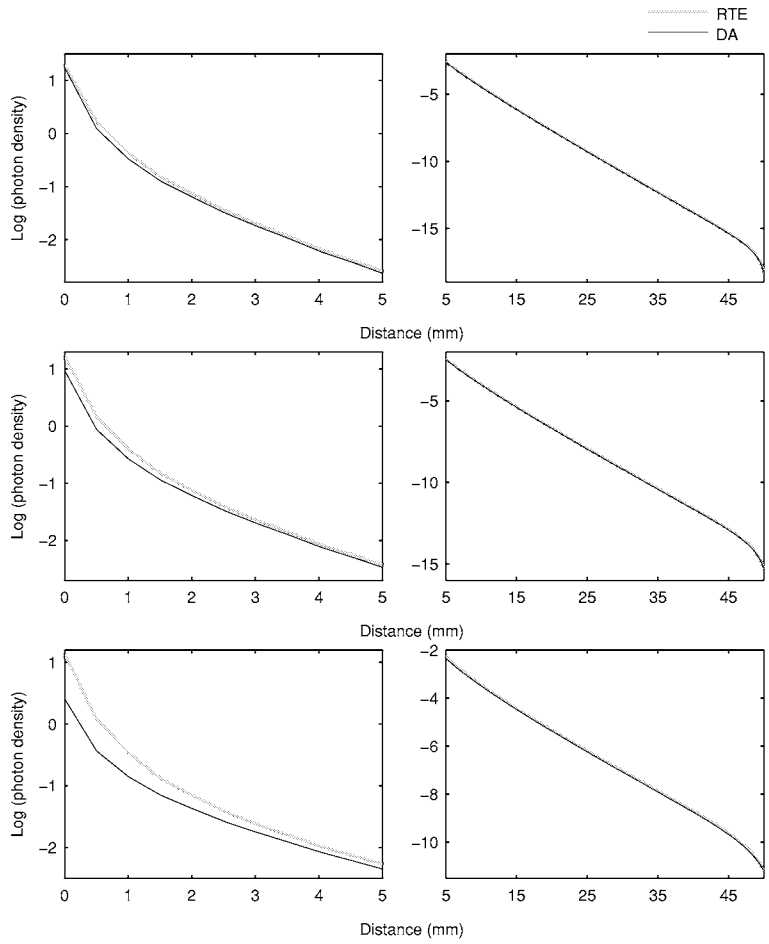

Figure 5.4: Logarithm of photon density against the distance from the source in a circular domain. On the left, there are the distances from the source site to 5 mm, and on the right, there are the distances from 5 mm to 50 mm. The scattering shape parameters were $g = 0.2$ (case 2.A), $g = 0.5$ (case 2.B), and $g = 0.8$ (case 2.C) (images from top to bottom in the respective order).

Results and discussion

The photon densities that were calculated with different scattering coefficients (simulations 1.A–1.C) are shown in Figure 5.3 and the photon densities calculated with different scattering shape parameter values (simulations 2.A–2.C) are shown in Figure 5.4. The figures show the logarithms of photon densities along the source

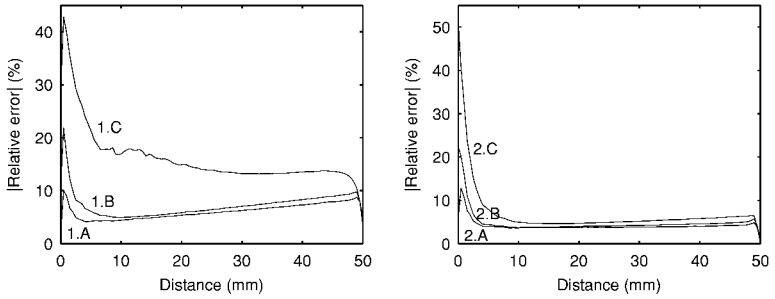

Figure 5.5: Absolute value of relative error of the DA photon density with respect to the RTE solution against the distance from the source. On the left, the scattering coefficients were $\mu_s = 2\,\mathrm{mm}^{-1}$ (case 1.A), $\mu_s = 1\,\mathrm{mm}^{-1}$ (case 1.B), and $\mu_s = 0.2\,\mathrm{mm}^{-1}$ (case 1.C). On the right, the scattering shape parameters were $g = 0.2$ (case 2.A), $g = 0.5$ (case 2.B), and $g = 0.8$ (case 2.C).

direction solved with the RTE and the DA. The RTE and DA results are in the same scale and they were scaled with respect to the source strength. The solutions were also compared by calculating the relative errors of the DA photon densities with respect to the RTE solution. The absolute values of relative errors against the distance from the source are shown in Figure 5.5 in which the simulations 1.A–1.C are shown on the left and the simulations 2.A–2.C are shown on the right.

The exitances that were calculated with different scattering coefficients are shown in Figure 5.6 and the exitances that were calculated with different values of scattering shape parameter are shown in Figure 5.7. The figures show the logarithms of exitances against the detection angle solved with the RTE, the DA, and Monte Carlo. The results are in the same scale and they were scaled with respect to the exitance in the measurement position closest to the source.

The results show that the DA gives almost the same results as the RTE within the highly scattering medium. As it can be seen from Figures 5.3 and 5.5, the photon densities solved with the RTE and the DA are almost equal within the highly scattering medium (simulation 1.A). As the scattering decreases, the difference between the RTE and DA solution increases (simulations 1.B and 1.C). Furthermore, as it can be seen from Figures 5.4 and 5.5, when the shape of the scattering probability distribution changes from uniform to forward peaked, the distance from the source in which the RTE and the DA give equal results increases.

Comparing the results with the Monte Carlo simulation reveals more clearly the limitations of the DA. The RTE solution and the Monte Carlo solution correspond well in all of the simulations. However, as it can be seen from Figure 5.6, the low scattering simulations 1.B and 1.C (middle and right images in Figure 5.6), show clear differences between the DA solution and the Monte Carlo solution. Moreover, as it can be seen from Figure 5.7, the DA solution differs from Monte Carlo also

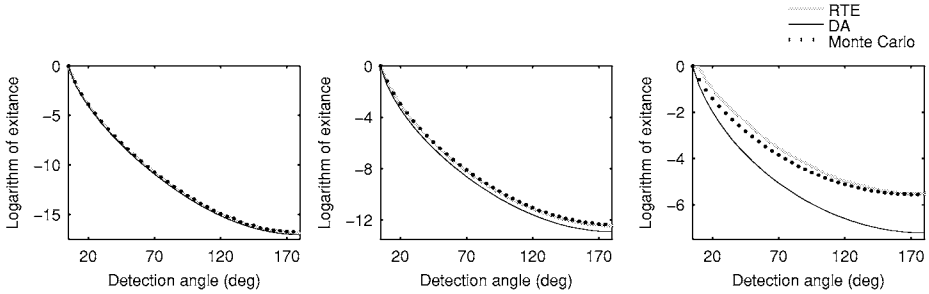

Figure 5.6: Logarithm of exitance against the detection angle in a circular domain. The scattering coefficients were $\mu_s = 2\,\mathrm{mm}^{-1}$ (case 1.A), $\mu_s = 1\,\mathrm{mm}^{-1}$ (case 1.B), and $\mu_s = 0.2\,\mathrm{mm}^{-1}$ (case 1.C) (images from left to right in the respective order).

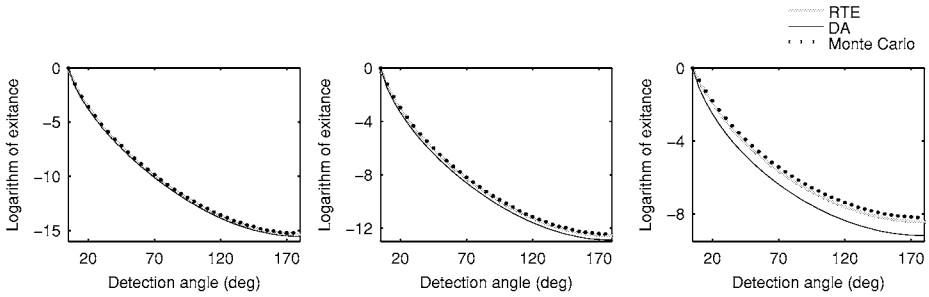

Figure 5.7: Logarithm of exitance against the detection angle in a circular domain. The scattering shape parameters were $g = 0.2$ (case 2.A), $g = 0.5$ (case 2.B), and $g = 0.8$ (case 2.C) (images from left to right in the respective order).

when the shape of the scattering probability distribution is forward peaked.

As explained in Section 3.2, one of the assumptions behind the DA is that the medium is strongly scattering. In simulations 1.B and 1.C this condition is violated, and therefore the DA fails to produce accurate estimates for light propagation. Furthermore, the first order approximation for the radiance, equation (3.16), which assumes that the angular distribution of the radiance is almost uniform, is violated close to the source. The distance from the source, in which the approximation (3.16) is valid, is longer when the scattering probability is forward peaked.

5.2 Hybrid model simulations

The performance of the proposed hybrid model approach was tested with 2D simulations. The simulations were carried out in a rectangular domain Ω similar to one illustrated in Figure 3.1. The size of the domain was $35\,\mathrm{mm} \times 70\,\mathrm{mm}$ and the light source was located at the centre of the upper edge. The absorption coefficient of the medium was $\mu_a = 0.025\,\mathrm{mm}^{-1}$ and the scattering coefficient was $\mu_s = 2\,\mathrm{mm}^{-1}$. The scattering shape parameter in the Henyey–Greenstein phase function was $g = 0$. Thus, the scattering probability was equal to all directions and the reduced scattering coefficient was $\mu_s' = 2\,\mathrm{mm}^{-1}$. The modulation frequency of the input signal was chosen as 50 MHz and the refractive indices of the medium and the surrounding medium were chosen as $n_{\mathrm{in}} = 1.4$. The results of the hybrid model were compared with the FE-solutions of the RTE and the DA and with the results of the Monte Carlo simulation.

Models

Hybrid model approach: The photon density was calculated with the proposed approach as follows. First, the RTE was solved in a rectangular sub-domain Ω_{be} with the FEM using equation (4.12). The size of of the sub-domain Ω_{be} was $20\,\mathrm{mm} \times 40\,\mathrm{mm}$. The spatial FE-discretization of the RTE contained 6328 nodal points and 12430 triangular elements. In angular discretization, 16 angular directions were used. As a solution of the RTE, the radiance in the nodal points of the FE-mesh in Ω_{be} was obtained.

The solution of the RTE was used to construct the distributed source model for the DA at the interface $\tilde{\Gamma}$ which was an arc with the centre at the source site, see Figure 3.1. The photon density at the interface $\tilde{\Gamma}$ was solved from the radiance using equation (3.9). Different subdivisions of the RTE and DA sub-domains were tested by changing the radius of the arc by varying it between $\tilde{r} = 1\,\mathrm{mm}$ and $\tilde{r} = 19\,\mathrm{mm}$. The arc radii of different tests are given in Table 5.2.

Finally, the DA was solved in the sub-domain Ω_{da} with the FEM using equation (4.30). The light source was modelled with the Dirichlet boundary condition that was derived from the solution of the RTE at the interface $\tilde{\Gamma}$. The sizes of the FE-discretizations of the DA sub-domains in different tests are given in Table 5.2. As a solution of the DA, the photon density in the nodal points of the FE-discretization in Ω_{da} was obtained.

Comparison results: For comparison, the FE-solution of the RTE and the FE-solution of the DA were computed in the whole domain Ω as described in Sections 4.1 and 4.2. The FE-discretization of the RTE contained 10204 nodal points and 20096 triangular elements, and 16 angular directions. The FE-discretization of the DA contained 8548 nodal points and 16800 triangular elements. In the FE-solution of the DA, the source was modelled as an isotropic point source which located at the depth $1/\mu_s'$ below the source site. The results were also compared with the results of the Monte Carlo simulation. The Monte Carlo simulation was performed as described in Section 4.4.1 with the weight of the photon packet saved in each pixel which is crossed.

Table 5.2: The source–interface distance $\tilde{r}$ and the number of the DA discretization nodal points N and elements El in different tests.

	$\tilde{r}$(mm)	N	El		$\tilde{r}$(mm)	N	El
1:	1	4401	8576	11:	11	3971	7716
2:	2	4318	8414	12:	12	3944	7662
3:	3	4323	8428	13:	13	3916	7604
4:	4	4300	8382	14:	14	3844	7460
5:	5	4234	8250	15:	15	3711	7192
6:	6	4189	8158	16:	16	3651	7072
7:	7	4182	8144	17:	17	3552	6872
8:	8	4129	8036	18:	18	3466	6698
9:	9	4127	8032	19:	19	3366	6498
10:	10	4060	7896				

Choice of the interface boundary location

The effect of interface boundary location on the hybrid model results was investigated. Therefore, the location of the interface boundary $\tilde{\Gamma}$ was changed by changing the radius of the arc. The radius of the arc was varied between $\tilde{r} = 1\,\text{mm}$ and $\tilde{r} = 19\,\text{mm}$. As explained in Section 3.3, the interface location can be chosen from the hybrid model results by monitoring the deviation of the angular distribution of the radiance from the first order approximation (3.16). Therefore, the norm of the difference between the radiances obtained as the solution of the RTE in Ω_{be} and through the DA in Ω_{da} in three points of the interface $\tilde{\Gamma}$ was computed for all of the source–interface distances. The obtained norms against the source–interface distance are shown in Figure 5.8. As it can be seen from Figure 5.8, the norm is large if the interface is located too close to the source. As explained in Section 3.3, this is due to the fact that the DA is not a valid approximation close to the source. Furthermore, the norm decreases when the distance from the source increases.

The interface location was also investigated by comparing the hybrid model results with the solution of the RTE in the whole domain. For each source–interface distance, the norm of the difference between the photon densities obtained with the RTE and with the hybrid model in 100 points along the source direction through the domain was calculated. The norm against the source–interface distance is shown in Figure 5.9. Similarly as in Figure 5.8, the norm is large if the interface is located too near to the light source and the norm decreases when the distance from the source increases. On the other hand, the norm also increases when the interface location approaches the boundaries of the domain Ω_{be}. This results from the fact that when the RTE is solved in Ω_{be}, wrong boundary condition is used and the photons that are scattered back to the domain Ω_{be} from $\Omega \setminus \Omega_{\text{be}}$ are neglected.

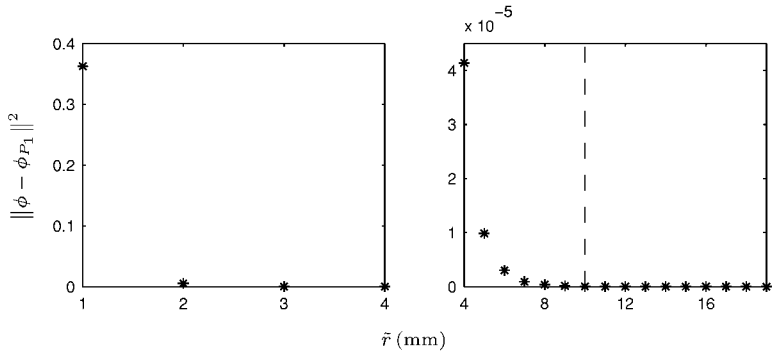

Figure 5.8: Norm of the difference between the radiances obtained with the hybrid model as the solution of the RTE and through the DA $\|\phi - \phi_{P_1}\|^2$ against the source–interface distance $\tilde{r}$. On the left, there are the distances from 1 mm to 4 mm, and on the right, there are the distances from 4 mm to 19 mm. The dashed line indicates the interface location that was used in the simulations.

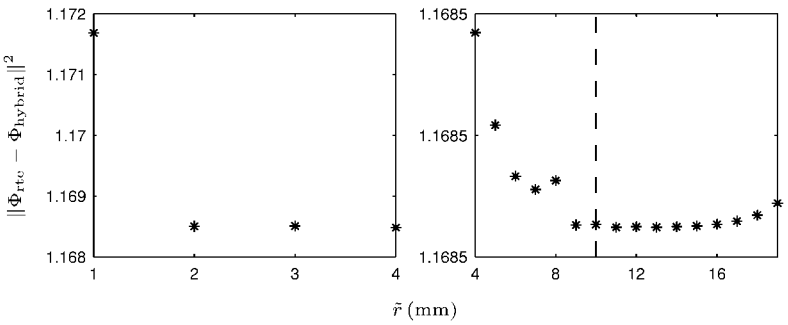

Figure 5.9: Norm of the difference between the photon densities obtained with the RTE and with the hybrid model $\|\Phi_{\mathrm{rte}} - \Phi_{\mathrm{hybrid}}\|^2$ against the source–interface distance $\tilde{r}$. On the left, there are the distances from 1 mm to 4 mm, and on the right, there are the distances from 4 mm to 19 mm. The dashed line indicates the interface location that was used in the simulations.

Comparison and discussion

The hybrid model solution with the source–interface distance $\tilde{r} = 10$ mm (the test 10) was chosen for further investigation. The solution was compared with the FE-solutions of the RTE and the DA, and with the results of the Monte Carlo simulation. The photon densities that were calculated with the different approaches are shown in Figure 5.10. The logarithms of amplitudes against the distance from the

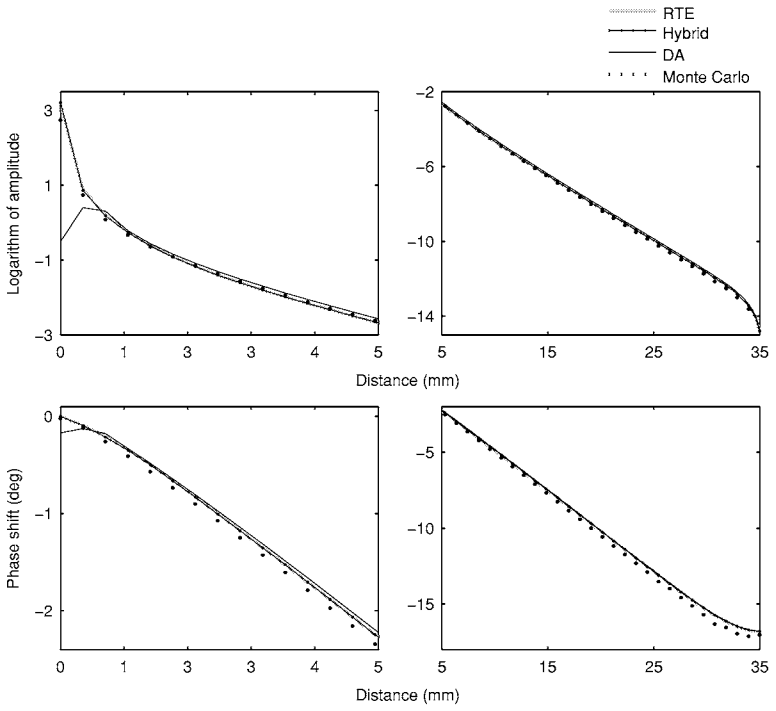

Figure 5.10: Logarithm of amplitude (top row) and phase shift (bottom row) of photon density against the distance from source. On the left, there are the distances from the source site to 5 mm, and on the right, there are the distances from 5 mm to 35 mm.

source are shown on the top row and the phase shifts against the distance from the source are shown on the bottom row. The results are in the same scale and they were scaled with respect to the source strength. The finite element solutions were compared with the Monte Carlo solution by computing the relative errors. The obtained absolute values of relative errors of photon densities along the source direction are shown in Figure 5.11 in which the relative errors of amplitudes are shown on the left and the relative errors of phase shifts are shown on the right.

The simulations show that the proposed hybrid model gives almost as accurate results as the FE-solution of the RTE in the whole domain. This can be seen from Figure 5.10 in which the photon densities obtained with the two approaches are almost equal. Both of the solutions differ from the FE-solution of the DA close to the source. This is due to the fact that the collimated light source cannot be modelled accurately with the DA. Comparing the results with the Monte Carlo simulation supports the results. As it can be seen from Figure 5.11, the deviations

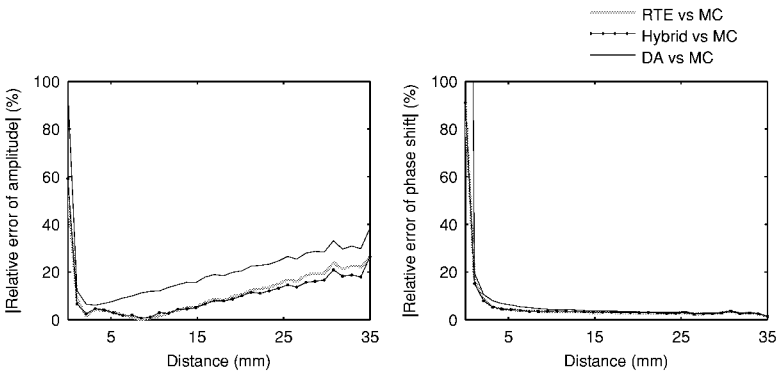

Figure 5.11: Absolute value of relative error of photon density amplitude (on the left) and phase shift (on the right) with respect to the Monte Carlo solution against the distance from the source. The right image vertical axis is cut at 100 %.

of the hybrid model approach and the RTE with respect to the Monte Carlo solution are similar, and the deviations are smaller than the deviation of the DA from the Monte Carlo solution. Thus, the proposed hybrid model gives an improved accuracy with respect to the conventional DA formulation.

The sizes of the FE-discretizations were also compared since the computational load is proportional to the mesh size. In optical tomography, the FE-discretization has to be very dense close to the light sources due to the fast attenuation of the solution near the sources. However, when the smooth RTE based distributed source model is used at the interface $\tilde{\Gamma}$, the mesh can be coarser in the domain Ω_{da} where the DA is solved. In simulations, the FE-mesh of the hybrid model was distinctly coarser in Ω_{da} than the mesh that was used to solve the DA in the entire domain Ω. This indicates that the computational times can be reduced significantly if a smooth distributed source model is utilized in the DA formulation.

5.3 Coupled RTE–DA model simulations

The validity of the coupled RTE–DA model was tested with simulations. Light propagation was simulated in a homogeneous highly scattering medium, in highly scattering media with low-scattering and a non-scattering regions, and in a realistic head geometry with tissue-like optical properties. The coupled RTE–DA model was numerically solved with the FEM. The solutions of the coupled model were compared with the FE-solutions of the RTE and the DA. In addition, the results in highly scattering medium were compared with the results of the hybrid model. Further, the simulations in highly scattering media with low-scattering and non-scattering regions and in the head geometry were compared with the results of Monte Carlo simulation.

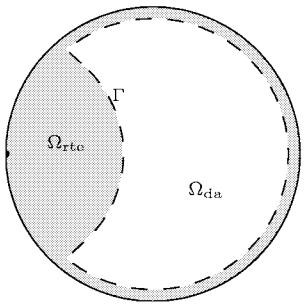

Figure 5.12: Circular domain with source on the left. The RTE is used as the forward model in the sub-domain Ω_{rte} (grey colour), the DA is used as the forward model in the sub-domain Ω_{da} (white colour), and the interface Γ separates the RTE and DA sub-domains (dashed line).

This section is organized as follows: the simulations in a homogeneous highly scattering medium are presented in Section 5.3.1, the simulations in highly scattering media with low-scattering and non-scattering regions are presented in Section 5.3.2, and finally, the simulations in a realistic head geometry are presented in Section 5.3.3.

5.3.1 Coupled model in highly scattering medium

The performance of the proposed coupled RTE–DA approach was tested with 2D simulations in a circular domain Ω similar to the one illustrated in Figure 5.12. The radius of the circle was $r = 25\,\mathrm{mm}$ and the centre was located at the origin. The collimated light source was located at $\begin{pmatrix} -25 & 0 \end{pmatrix}$ with direction perpendicular to $\partial\Omega$. The absorption and scattering coefficients of the medium were $\mu_a = 0.025\,\mathrm{mm}^{-1}$ and $\mu_s = 2\,\mathrm{mm}^{-1}$, respectively. The scattering shape parameter of the Henyey–Greenstein scattering function was $g = 0$, and thus the reduced scattering coefficient was $\mu_s' = 2\,\mathrm{mm}^{-1}$. The modulation frequency of the input signal was chosen as 50 MHz, and the refractive indices of the medium and the surrounding medium were chosen as $n_{\mathrm{in}} = 1.4$.

The proposed coupled RTE–DA model was solved using the FEM. For comparison, the FE-solution of the RTE and the FE-solution of the DA were computed. In addition, the FE-solution of the hybrid model was computed. The other FE-solutions were compared to the RTE solution. The quantities that were investigated were the photon density inside the domain and the exitance on the boundary of the domain. The spatial FE-element discretizations for the different models were different but of the same order. In addition, the discretizations were very dense. By this, it was assured that the methods could be compared equally without favoring the RTE based approaches.

Table 5.3: The source–interface distance r, the number of RTE discretization nodal points N_n and elements $\mathrm{El}_{\mathrm{rte}}$, and the number of DA discretization nodal points N and elements $\mathrm{El}_{\mathrm{da}}$ in different tests.

	r(mm)	N_n	$\mathrm{El}_{\mathrm{rte}}$	N	$\mathrm{El}_{\mathrm{da}}$
1:	2	3863	7032	12308	24284
2:	3	3700	6716	12074	23828
3:	4	3748	6824	11682	23050
4:	5	4120	7557	11630	22940
5:	10	4720	8773	11024	21744
6:	15	5679	10691	9989	19674
7:	20	7086	13511	8658	17018
8:	25	8601	16549	7125	13962
9:	30	10308	19979	5307	10342

MODELS

Coupled RTE–DA model: The forward problem was solved with the coupled RTE–DA model as follows. The domain Ω was divided into two sub-domains Ω_{rte}, in which the RTE was used as the forward model, and Ω_{da}, in which the DA was used as the forward model. The RTE sub-domain Ω_{rte} included the domains close to the source and boundary and it is illustrated in Figure 5.12 with grey colour. The DA sub-domain Ω_{da} covered the remaining area and it is illustrated in Figure 5.12 with white colour. The coupled RTE–DA model was tested with different subdivisions of the RTE and DA sub-domains by changing the location of the interface Γ which separates the sub-domains. The interface Γ, which is marked in Figure 5.12 with dashed line, was located at the distance 2 mm from the boundary of the domain except close to the source where Γ was an arc with the centre at the source site and the radius varying between 2 mm and 30 mm. The tests and the source–interface distances of different subdivisions of the RTE and DA sub-domains are given in Table 5.3.

The coupled RTE–DA model was numerically solved using the FEM as described in Section 4.3. The sizes of the spatial FE-discretizations of different RTE and DA subdivisions are given in Table 5.3. The angular discretization of the RTE contained 16 angular directions. The forward problem was solved with the FEM using equation (4.50). As a solution of the forward problem, the radiance in the RTE sub-domain nodal points and the photon density in the DA sub-domain nodal points were obtained. The photon density in the RTE sub-domain nodal points was solved from the radiance using equation (3.9). The exitance was solved on the domain boundary. The boundary was included into the RTE sub-domain Ω_{rte} and therefore the exitance was solved using equation (3.8).

RTE: The RTE was solved in Ω with the FEM as described in Section 4.1.

The FE-mesh for the discretization of the RTE contained 15282 nodal points, 30198 triangular elements and 16 angular directions. As a solution of the forward problem, the radiance in nodal points of the FE-mesh was obtained. The photon density was computed from the radiance using equation (3.9). Moreover, the exitance was solved on the boundary locations using equation (3.8).

DA: The DA was solved in the whole domain Ω with the FEM as described in Section 4.2. The source was modelled as an isotropic point source which located at the depth $1/\mu_s'$ below the source site. The FE-mesh for the discretization of the DA contained 15134 nodal points and 29910 triangular elements. The exitance was solved from the photon density on the boundary using equation (3.38).

Hybrid model: The FE-solution of the hybrid model was computed similarly as described in Section 3.3. Thus, first the RTE was solved in a sub-domain close to the source. The RTE sub-domain was an arc with the centre at the source site and the radius of 20 mm. The FE-discretization contained 5143 nodal points, 10060 triangular elements, and 16 angular directions. Then, the RTE solution was used to construct a distributed source model on a fictitious interface $\tilde{\Gamma}$ within the domain. The fictitious interface $\tilde{\Gamma}$ was an arc with the centre at the source site and the radius of 10 mm. Note, that the location of the RTE boundary ($r = 20$ mm) was chosen further from the source than the location of the fictitious interface ($\tilde{r} = 10$ mm) since in the hybrid model approach the fictitious interface must be located within the RTE sub-domain. Finally, the DA was solved in the remaining domain using the RTE solution on the fictitious interface as a Dirichlet boundary condition. The FE-discretization for the DA contained 12825 nodal points and 25316 triangular elements. The exitance was solved on the boundary locations using equations (3.8) and (3.38) depending whether the measurement position located in the RTE or DA sub-domain.

Effect of the source–interface distance

The effect of the source–interface distance on the accuracy of the coupled RTE–DA model solution was investigated. The source–interface distances of the coupled model were as in Table 5.3. The coupled RTE–DA model solutions with different source–interface distances were compared with the FE-solution of the RTE. The norm of the difference between the photon densities obtained with the RTE and with the coupled RTE-DA model were computed in 60 points along the source direction through the domain. The norm of the difference between the RTE solution and the coupled RTE–DA model solution against the source–interface distance is shown in Figure 5.13.

As it can be seen from Figure 5.13, the norm is large if the interface Γ is located too close to the light source, and the norm decreases when the source–interface distance increases. The large differences between the RTE and coupled RTE–DA model with short source–interface distances are due to the fact that the DA is not a valid approximation close to the source. The results also reveal the source–interface distances in which the norm is small, and therefore, the interface Γ can be located. It should be noted, that this distance depends on the optical properties of the medium.

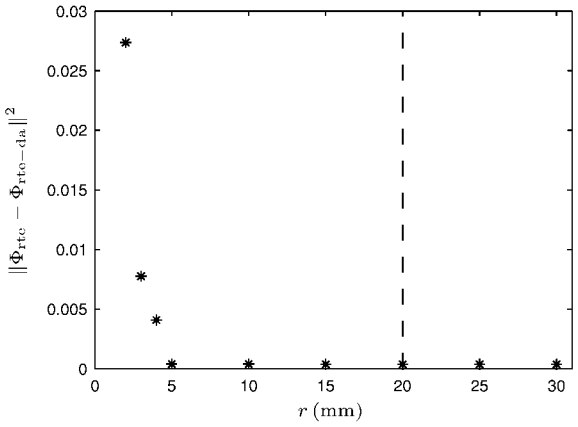

Figure 5.13: Norm of the difference between the photon densities obtained with the RTE and with the coupled RTE–DA model $\|\Phi_{\mathrm{rte}} - \Phi_{\mathrm{rte-da}}\|^2$ against the source–interface distance r. The dashed line indicates the distance that was used in the simulations.

Comparison and discussion

The coupled RTE–DA model solution with the source–interface distance $r = 20$ mm (test 7) was chosen for further investigation. The coupled model solution was compared with the solutions of the RTE, the DA, and the hybrid model. The photon densities that were calculated with the different approaches are shown in Figure 5.14. The logarithms of amplitudes along the source direction are shown on the top row and the phase shifts along the source direction are shown on the bottom row. All the results are in the same scale and they were scaled with respect to the source strength. The solutions of the coupled RTE–DA model, the DA, and the hybrid model were compared by computing the relative errors of photon densities with respect to the RTE solution. The obtained absolute values of relative errors of photon densities along the source direction are shown in Figure 5.15 in which the relative errors of amplitudes are shown on the left and the relative errors of phase shifts are shown on the right.

The exitances that were calculated with the different approaches are shown in Figure 5.16. The logarithms of amplitudes against the detection angle are shown on the top row and the phase shifts against the detection angle are shown on the bottom row. The results are in the same scale. The relative errors of exitances were also computed. The absolute values of relative errors of exitances against the detection angle are shown in Figure 5.17 in which the relative errors of amplitudes are shown on the left and the relative errors of the phase shifts are shown on the right.

The results show that the proposed coupled RTE–DA model gives almost the

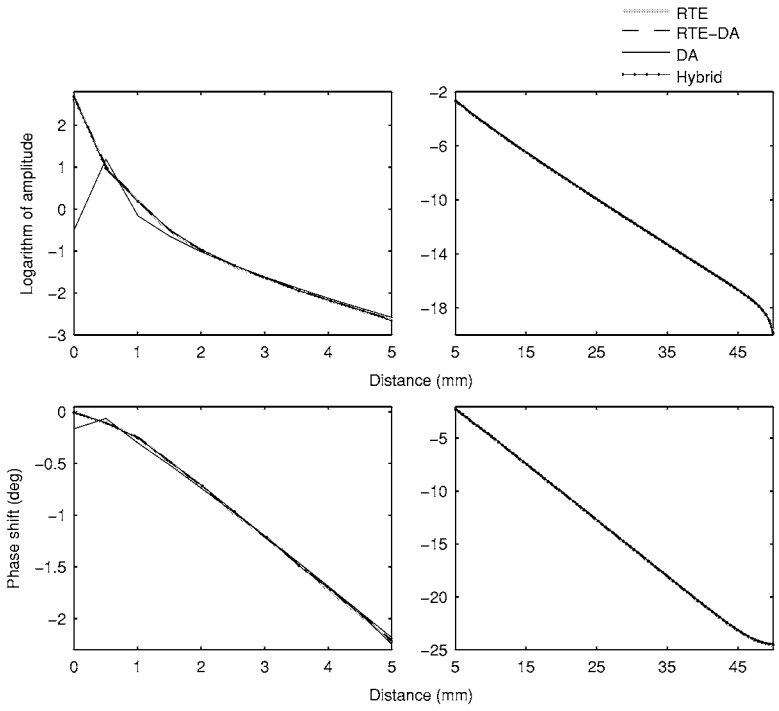

Figure 5.14: Logarithm of amplitude (top row) and phase shift (bottom row) of photon density against the distance from source in a highly scattering circular domain. On the left, there are the distances from the source site to 5 mm, and on the right, there are the distances from 5 mm to 50 mm.

same results as the RTE. The amplitudes and phase shifts of photon densities obtained with the two approaches are almost equal, which can be seen from Figure 5.14. Examining the relative errors supports the results. Thus, the coupled RTE–DA model has the smallest relative errors, which can be seen from Figure 5.15. The photon densities solved with the DA differ from the RTE solution close to the source where the largest relative errors can be found. The hybrid model approach gives better results than the DA but not as good as the coupled RTE–DA model. The weakness of the hybrid model approach is that, unlike the coupled RTE–DA model, it does not take into account the photons scattering between the RTE and DA sub-domains. This effect can be seen in Figure 5.15 in which the relative error of the hybrid model solution increases along the source direction when the location of the fictitious interface $\tilde{r} = 10\,\text{mm}$ is exceeded.

The amplitudes and phase shifts of exitances computed with the coupled RTE-DA model are almost equal to the RTE exitances, which can be seen from Figure

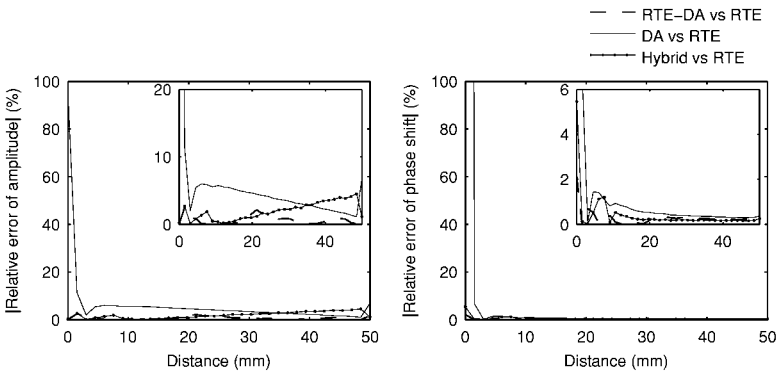

Figure 5.15: Absolute value of relative error of photon density amplitude (on the left) and phase shift (on the right) with respect to the RTE solution against the distance from the source. The right image vertical axis is cut at 100 %.

5.16. Furthermore, the exitances computed with the coupled RTE–DA model are closer to the RTE solution than the exitances computed with the DA. The relative errors of exitances obtained with the coupled RTE–DA model with respect to RTE solution are relatively small, which can be seen from Figure 5.17. The DA and the hybrid model have larger relative errors than the coupled model. Especially, the DA has large errors close to the source. The errors in the DA solution are due to the fact that the DA is not a good approximation close to the source and it can not accommodate realistic boundary conditions.

5.3.2 Coupled model in highly scattering medium with low-scattering and non-scattering regions

The performance of the coupled RTE–DA approach was tested with 2D simulations in a highly scattering circular domain which contained a low-scattering or a non-scattering inclusion. The type of domains are illustrated in Figure 5.18. Two types of inclusions were investigated: a ring-like gap close to the boundary (left image) and a hole at the centre (right image). The inclusions are marked with dark grey colour in the images of Figure 5.18. The radius of the circle was 25 mm and the centre was located at the origin. The collimated light source was located at $\begin{pmatrix} -25 & 0 \end{pmatrix}$ with direction perpendicular to $\partial\Omega$. The modulation frequency of the input signal was chosen as 50 MHz. The refractive indices of the background medium, inclusion, and the surrounding medium were chosen as $n_{\text{in}} = 1.4$. Different inclusion sizes were tested as well as different optical properties. The optical properties used in the simulations are given in Table 5.4.

The coupled RTE–DA model was solved using the FEM. The RTE was used as the forward model in the sub-domain Ω_{rte} which included the regions close to the source and boundaries and within the inclusion. The RTE sub-domain

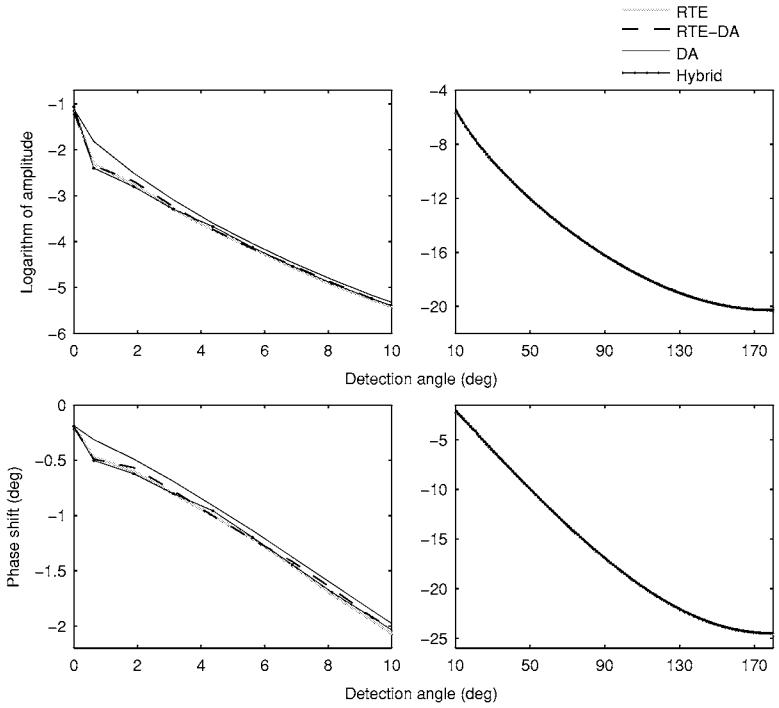

Figure 5.16: Logarithm of amplitude (top row) and phase shift (bottom row) of exitance against the detection angle in a highly scattering circular domain. On the left, there are the angles from 0° to 10°, and on the right, there are the angles from 10° to 180°.

Table 5.4: The absorption coefficient μ_a, the scattering coefficient μ_s, the scattering shape parameter g, and the reduced scattering coefficient μ_s' of the background medium and the inclusion used in the simulations.

	Background				Inclusion			
	$\mu_a(\text{mm}^{-1})$	$\mu_s(\text{mm}^{-1})$	g	$\mu_s'(\text{mm}^{-1})$	$\mu_a(\text{mm}^{-1})$	$\mu_s(\text{mm}^{-1})$	g	$\mu_s'(\text{mm}^{-1})$
A:	0.025	2	0	2	0.025	0.02	0	0.02
B:	0.025	2	0	2	0.025	0	–	0
C:	0.025	2	0.8	0.4	0.025	0.02	0.9	0.002

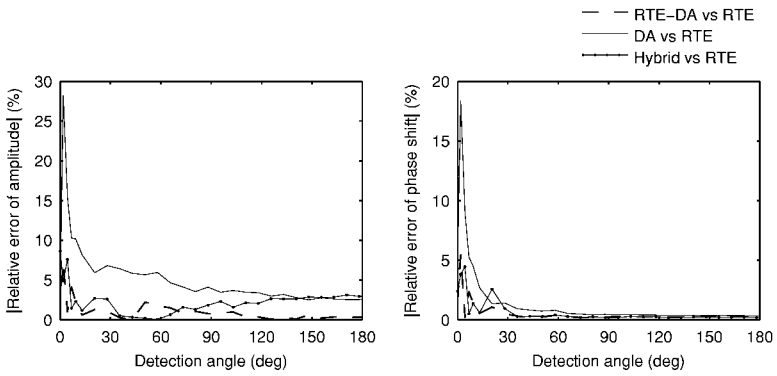

Figure 5.17: Absolute value of relative error of exitance amplitude (on the left) and phase shift (on the right) with respect to the RTE solution against the detection angle.

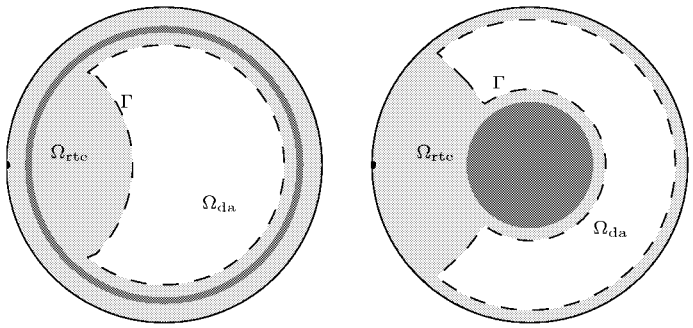

Figure 5.18: Two circular domains with a low-scattering or non-scattering inclusion (dark grey colour). On the left, the inclusion is a ring-like gap close to the boundary, and on the right, the inclusion is a hole at the centre. The source is located on the left. The RTE is used as the forward model in the sub-domain Ω_{rte} (light grey colour), the DA is used as the forward model in the sub-domain Ω_{da} (white colour), and the interface Γ separates the RTE and DA sub-domains (dashed line).

is illustrated in Figure 5.18 with light grey colour. The DA was used as the forward model in the sub-domain Ω_{da} which covered the remaining domain and is illustrated in Figure 5.18 with white colour. The interface Γ, which separates the RTE and DA sub-domains, was located at a distance 20 mm from the source and 2 mm from the external boundary and the boundary of the inclusion. The interface Γ is marked in Figure 5.18 with dashed line. The finite element calculations were

performed as described in Section 4.3. The streamline diffusion modification was utilized in the solution of the coupled model with $\delta = \min\{\frac{1}{2(\mu_a+\mu_s)}, \frac{5}{(\mu_a+\mu_s)r_j}\}$, where r_j is the distance from the source to the jth element. In the case of the ring-like gap, the spatial FE-discretization contained 3954 nodal points (2515 in the RTE sub-domain and 1559 in the DA sub-domain) and 7731 triangular elements (4735 in the RTE sub-domain and 2996 in the DA sub-domain). In the case of the hole at the centre, the FE-discretization contained 4134 nodal points (2732 in the RTE sub-domain and 1588 in the DA sub-domain) and 8046 triangular elements (5058 in the RTE sub-domain and 2988 in the DA sub-domain). The angular discretization for the RTE contained 16 (tests A and B) or 32 (test C) directions.

For comparison, the FE-solutions of the RTE and the DA in the whole domain Ω were computed. The FE-calculations were performed as described Sections 4.1 and 4.2. where the streamline diffusion modification was applied in the solution of the RTE. The FE-solutions of the RTE and the DA were computed in the same spatial mesh as the FE-solution of the coupled RTE–DA model. The FE-solutions were also compared with the results of Monte Carlo simulation. The Monte Carlo simulations were performed as described in Section 4.4.1 with weight of the photon packet saved on the boundary of the domain.

Case 1: ring-like gap

As the first case, a situation in which the domain contained a ring-like gap close to the boundary (left image of Figure 5.18) was investigated. Such a domain can be regarded as a simple example of modelling the cerebrospinal fluid layer which surrounds the brain. The width of the gap was 1 mm and its outer boundary located 3 mm from the boundary. The optical properties of the test cases are given in Table 5.4. In all of the tests, the background absorption and scattering coefficients were $\mu_a = 0.025\,\mathrm{mm}^{-1}$ and $\mu_s = 2\,\mathrm{mm}^{-1}$, respectively, and the absorption coefficient of the gap was $\mu_a = 0.025\,\mathrm{mm}^{-1}$. In the first test case (Case 1.A), the gap consisted of low-scattering medium with $\mu_s = 0.02\,\mathrm{mm}^{-1}$. The scattering probability was a uniform distribution, and thus the scattering shape parameters of the background medium and the gap were $g = 0$. In the second test case (Case 1.B), the gap consisted of non-scattering medium ($\mu_s = 0\,\mathrm{mm}^{-1}$) and the scattering probability of the background medium was a uniform distribution ($g = 0$). Further, in the third test case (Case 1.C), the gap consisted of low-scattering medium and the scattering probability was a forward peaked, non-uniform distribution. The scattering coefficient of the gap was $\mu_s = 0.02\,\mathrm{mm}^{-1}$ and the scattering shape parameters of the background medium and the gap were $g = 0.8$ and $g = 0.9$, respectively.

First, the photon densities inside the domain were investigated. The results of the low-scattering gap test (Case 1.A) are shown in Figure 5.19 which shows the photon densities within the domain solved with the RTE, the coupled RTE–DA model, and the DA (images from left to right in the respective order). The logarithms of amplitudes are shown on the top row and the phase shifts are shown on the bottom row. The photon densities along the source direction for all of the test cases are shown in Figure 5.20. The logarithms of amplitudes against

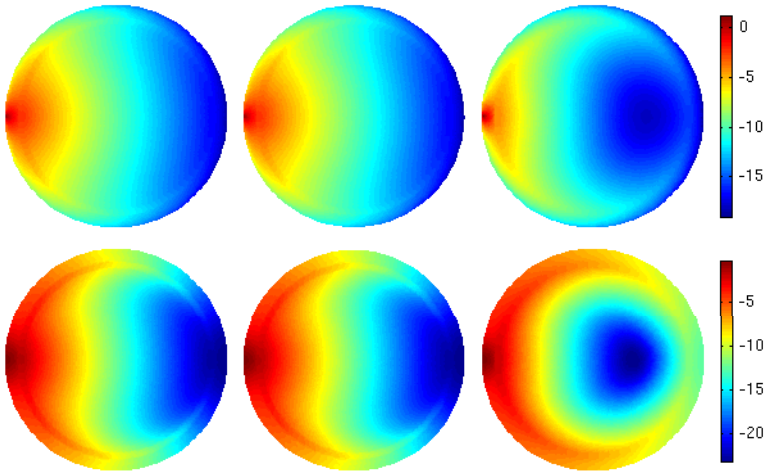

Figure 5.19: Logarithm of amplitude (top row) and phase shift (bottom row) of photon density within a domain with a 1 mm wide low-scattering gap (Case 1.A). From left to right: the RTE solution, the coupled RTE–DA model solution, and the DA solution.

the distance from the source are shown on the left and the phase shifts against the distance from the source are shown on the right. The images from top to bottom are from the following test cases: a low-scattering gap (Case 1.A), a non-scattering gap (Case 1.B), and forward peaked scattering (Case 1.C) where the optical properties are as in Table 5.4. The results in Figures 5.19 and 5.20 are in the same scale and they were scaled with respect to the source strength.

The exitances that were calculated with the coupled RTE–DA model, the RTE, the DA, and Monte Carlo are shown in Figure 5.21. The logarithms of amplitudes against the detection angle are shown on the left and the phase shifts against the detection angle are shown on the right. The images from top to bottom are from the following test cases: a low-scattering gap (Case 1.A), a non-scattering gap (Case 1.B), and forward peaked scattering (Case 1.C). The results in Figure 5.21 are in the same scale and they were scaled with respect to the amplitude of the measurement position closest to the source.

Examining the photon densities within the domain (Figures 5.19 and 5.20), shows that the proposed coupled RTE–DA model gives almost the same results as the RTE. The photon densities solved with the DA, however, differ clearly from the RTE solution. As it can be seen from Figure 5.19, the photon density within the gap is higher than the photon density within the surrounding background medium. Thus, the photons tend to propagate further within the gap. The amplitudes and phase shifts of photon densities obtained with the RTE and the coupled RTE–DA

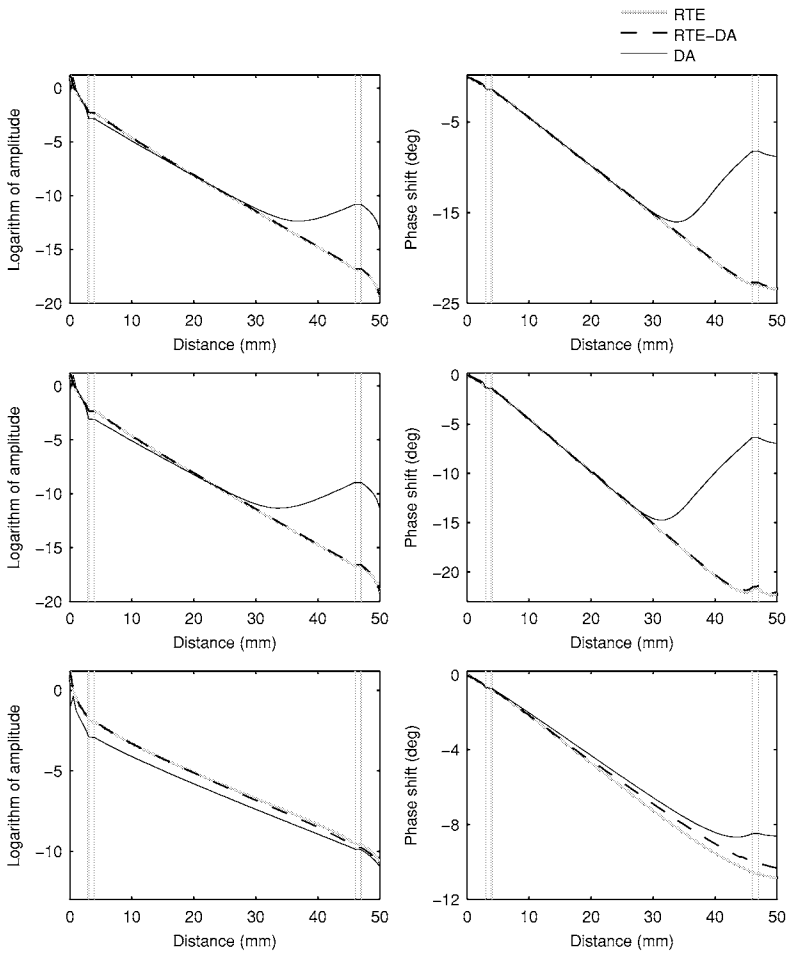

Figure 5.20: Logarithm of amplitude (left column) and phase shift (right column) of photon density against the distance from the source in a domain with a 1 mm wide gap. From top to bottom: a low-scattering gap (Case 1.A), a non-scattering gap (Case 1.B), and forward peaked scattering (Case 1.C). The locations of the gap are marked with vertical grey lines.

model are almost equal which can be seen from Figure 5.20. All the solutions show almost a flat region in the amplitude and phase data on the location of the gap. The shape of the DA solution, however, differs from the other approaches at this point. According to our tests, if the size of the gap is made wider, the flat region widens as well and the difference between the DA solution and other approaches increases. As it can be seen from Figure 5.20 the DA solution differs clearly from

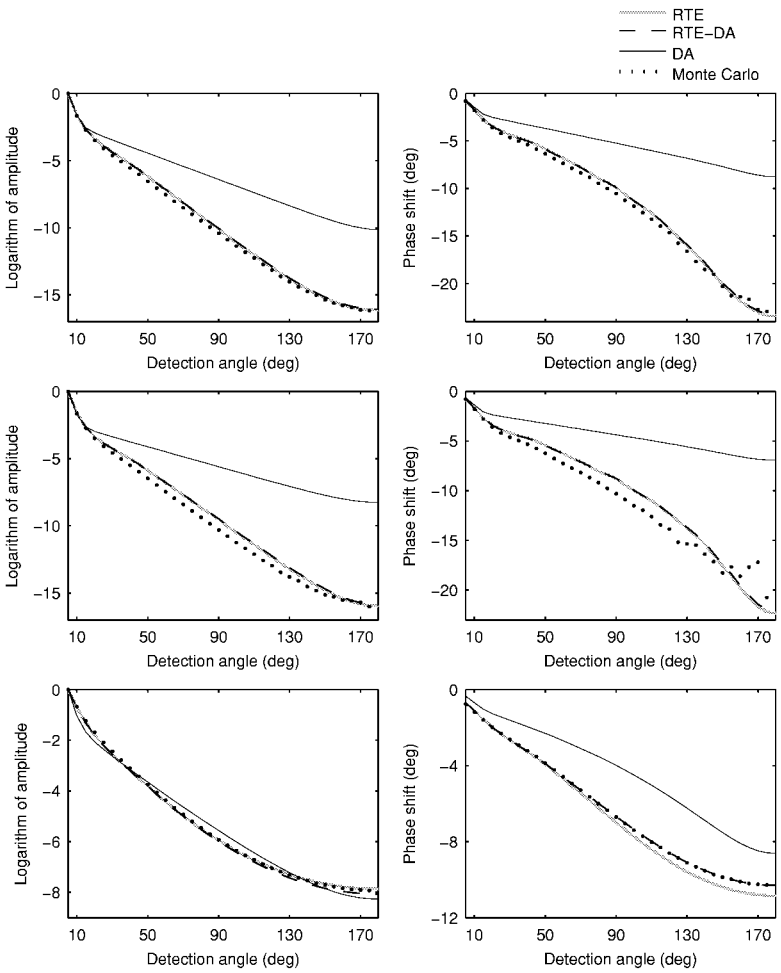

Figure 5.21: Logarithm of amplitude (left column) and phase shift (right column) of exitance against the detection angle in a domain with a 1 mm wide gap. From top to bottom: a low-scattering gap (Case 1.A), a non-scattering gap (Case 1.B), and forward peaked scattering (Case 1.C).

the other approaches especially farther from the source.

Examining the exitances on the boundary of the domain and comparing the FE-solutions with Monte Carlo simulations supports the results. The coupled RTE–DA model and the RTE give almost the same results as Monte Carlo. The DA, however, differs clearly from the Monte Carlo solution. This can be seen from Figure 5.21 in which the logarithms of amplitudes and phase shifts of exitances

Table 5.5: FE-matrix sizes, number of non-zero elements, and the forward solution computation times for the RTE, the coupled RTE–DA model, and the DA in the low-scattering gap test (Case 1.A). The number of angular directions in the RTE discretization was 16.

	Matrix size	Non-zeros	Time(s)
RTE:	63264×63264	6994432	1365.4
RTE–DA:	41799×41799	4381981	754.1
DA:	3954×3954	27322	6.4

against the detection angle are shown. The amplitudes and phase shifts solved with the RTE, the coupled RTE–DA, and Monte Carlo are almost the same whereas the DA solution differs clearly from the other solutions. The similar "kink" that was noticed by [13] can be seen both in amplitude and phase data of our results and it is located around the detection angle of 15°. It was noticed that as the width of the gap increases, the location of the "kink" is displaced.

Information about FE-matrix sizes and number of non-zero elements in them as well as the computation times for the low-scattering gap test (Case 1.A) are given in Table 5.5. All the FE-solutions were computed using the biconjugate gradient method with MATLAB® version 7.0 (R14), (The MathWorks, Inc.). The iterations were proceeded until they converged. As it can be seen from Table 5.5, the FE-discretization of the RTE is 16^2 times bigger than FE-discretization of the DA. The coupled RTE–DA model includes both the RTE and DA subdomains and the size of the FE-discretization depends on the amount and size of the low-scattering and non-scattering regions. As it can be seen from Table 5.5, the computation times for the RTE and the coupled RTE–DA model are both longer than for the whole domain DA. However, the coupled RTE–DA solution is obtained almost two times faster than the solution using the RTE in the whole domain.

Case 2: hole at the centre

As the second case, a situation in which the domain contained a hole at the centre (right image of Figure 5.18) was investigated. The radius of the hole was 10 mm. The optical properties of the test cases were the same as in the case of the gap and they are given in Table 5.4.

The photon densities inside the domain for the low-scattering hole test (Case 2.A) are shown in Figure 5.22. The FE-solutions from left to right are: the RTE solution, the coupled RTE–DA model solution, and the DA solution. The logarithms of amplitudes are shown on the top row and the phase shifts are shown on the bottom row. The photon densities along the source direction for all of the test cases are shown in Figure 5.23. The logarithms of amplitudes against the distance from the source are shown on the left and the phase shifts against the distance

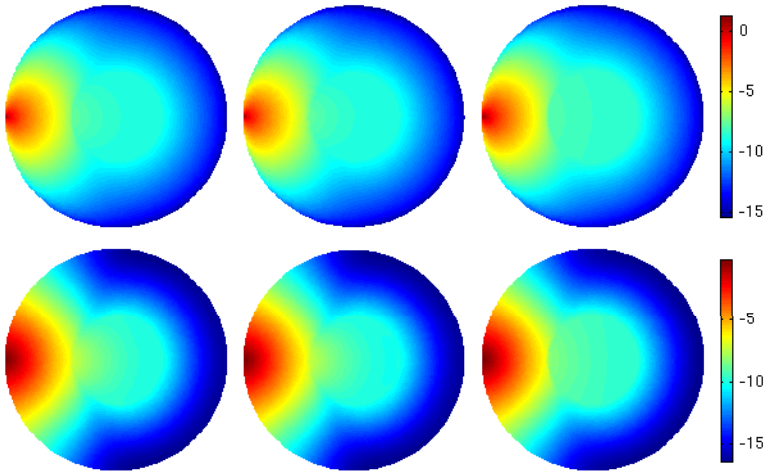

Figure 5.22: Logarithm of amplitude (top row) and phase shift (bottom row) of photon density within a domain with a 10 mm radius low-scattering hole at the centre (Case 2.A). From left to right: the RTE solution, the coupled RTE–DA model solution, and the DA solution.

from the source are shown on the right. The images from top to bottom are from the following test cases: a low-scattering hole (Case 2.A), a non-scattering hole (Case 2.B), and forward peaked scattering (Case 2.C) where the optical properties are as in Table 5.4.

The exitances on the boundary of the domain are shown in Figure 5.24. The logarithms of amplitudes against the detection angle are shown on the left and the phase shifts against the detection angle are shown on the right. The images from top to bottom are from the following test cases: a low-scattering hole (Case 2.A), a non-scattering hole (Case 2.B), and forward peaked scattering (Case 2.C).

Examining the photon densities inside the domain shows again that the photons tend to propagate further within the low-scattering or non-scattering hole. This can be seen from Figure 5.22 in which the photon densities within the domain with the low-scattering hole (Case 2.A) are shown. The amplitudes and phase shifts of photon densities obtained with the coupled RTE–DA model are almost equal to the RTE solution which can be seen from Figure 5.23. The photon densities solved with the DA, however, differ from the RTE solution especially on the location of the hole.

Examining the exitances on the boundary of the domain and comparing the FE-solutions with the Monte Carlo simulations supports the results. The coupled RTE–DA model and the RTE give almost the same results as Monte Carlo which can be seen from Figure 5.24. The DA solution does not show a clear difference

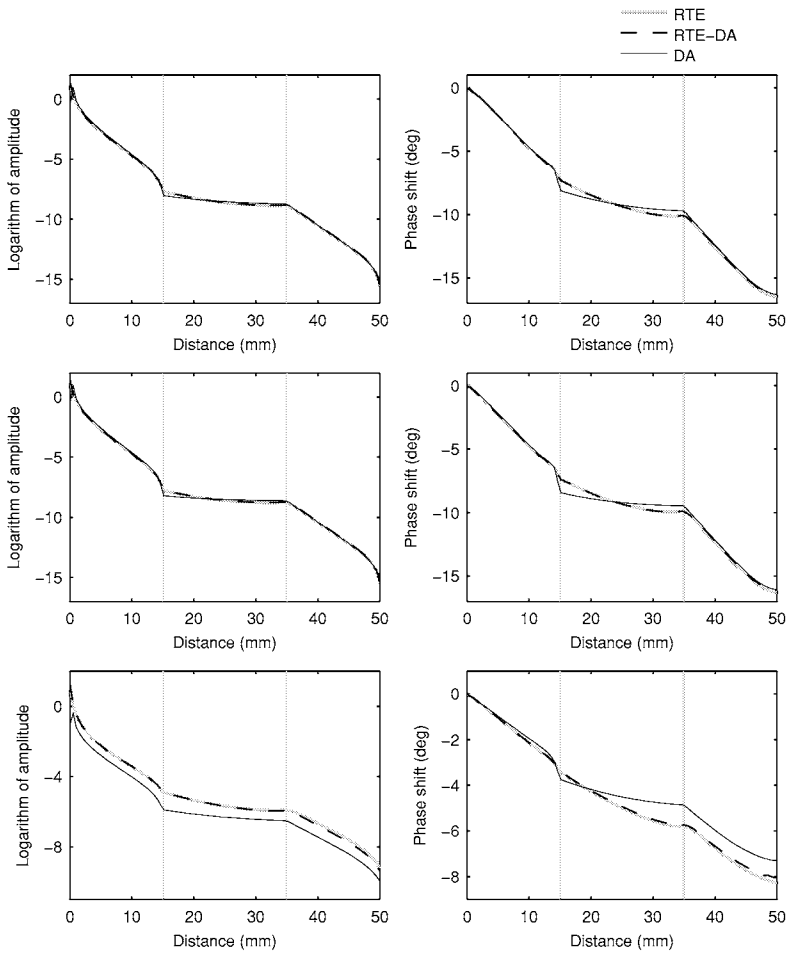

Figure 5.23: Logarithm of amplitude (left column) and phase shift (right column) of photon density against the distance from the source in a domain with a 10 mm radius hole at the centre. From top to bottom: a low-scattering hole (Case 2.A), a non-scattering hole (Case 2.B), and forward peaked scattering (Case 2.C). The location of the hole is marked with vertical grey lines.

from the other approaches when the scattering probability is a uniform distribution ($g = 0$ in Cases 2.A and 2.B). However, when $g = 0.8$ and $g = 0.9$ (Case 2.C) the DA solution differs from the other approaches.

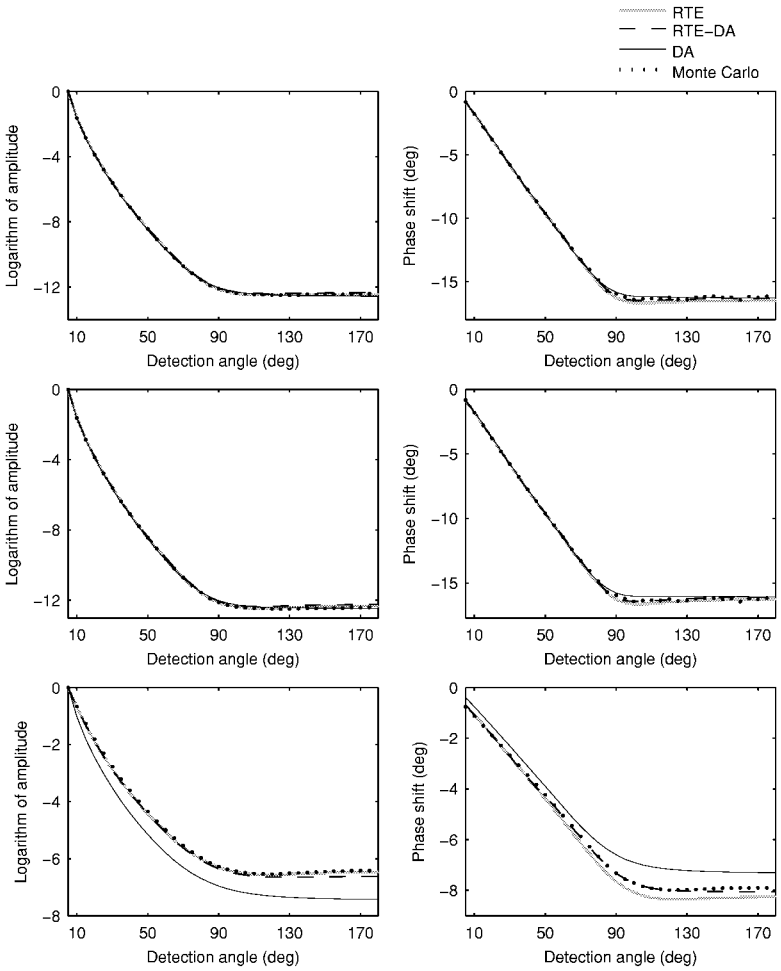

Figure 5.24: Logarithm of amplitude (left column) and phase shift (right column) of exitance against the detection angle in a domain with a 10 mm radius hole at the centre. From top to bottom: a low-scattering hole (Case 2.A), a non-scattering hole (Case 2.B), and forward peaked scattering (Case 2.C).

Discussion

The coupled RTE–DA model was tested with 2D simulations in circular highly scattering media with low-scattering and non-scattering regions. In the approach, the RTE was used as the model for light propagation in sub-domains in which the assumptions of the DA are not valid. These sub-domains included the regions close

to the source and boundary and the low-scattering and non-scattering regions. The DA was used as the forward model elsewhere in the domain. In simulations, two types of inclusions were investigated: a ring-like gap close to the boundary and a hole at the centre. Both geometries were tested with different optical properties. The results of the coupled RTE–DA model were compared with the FE-solutions of the RTE and the DA and with the results of Monte Carlo simulation.

The results show that in the case of the low-scattering or non-scattering gap close to the boundary, the coupled RTE–DA model gives almost the same results as the finite element solution of the RTE. Moreover, the FE-solutions of the coupled RTE–DA model and the RTE are similar to the results of Monte Carlo simulation. The DA solution, however, differs clearly from the other approaches. This is especially evident for the phase data. In the case of the hole at the centre, the coupled RTE–DA model gives almost the same results as the FE-solution of the RTE and the Monte Carlo simulation. The DA solution does not show a clear difference from the other approaches in cases in which the scattering probability is a uniform distribution. However, when the scattering probability is a non-uniform distribution, the DA solution differs from the other approaches clearly.

When comparing the memory requirements of the finite element solutions, it should be noted that the FE-discretization of the RTE includes both the spatial and angular discretizations. Thus, compared to the DA with the same spatial FE-discretization, the RTE problem is bigger than the DA problem. The coupled RTE–DA model includes both the RTE and DA sub-domains, and thus the angular discretization is needed in the RTE sub-domain only. This makes the coupled RTE–DA problem smaller than the RTE problem in the whole domain and the computation times are shorter as well. This difference in computational burden is even more significant in larger domains and in 3D case of optical tomography where the angular RTE discretization includes both azimuth and polar angles.

5.3.3 Coupled model in a realistic head geometry

The coupled RTE–DA model was tested with tissue-like optical properties in a realistic head geometry. The simulations were performed in a 2D segmented image that was done from a magnetic resonance image of a new-born infant head. The 2D head slice is shown in left image of Figure 5.25. The segmentation consisted of six domains which were: scalp, skull, grey matter, white matter, CSF around the brain, and CSF in ventricles. The optical parameters used the in simulations are given in Table 5.6. The modulation frequency of the input signal was 100 MHz, and the refractive index within the head and the surrounding medium was $n_{\text{in}} = 1.3$.

Models

The forward problem was solved with the coupled RTE–DA model in the head slice domain. The computation domain is illustrated in the right image of Figure 5.25 where the CSF regions are marked with dark grey colour. The domain was divided into the RTE and DA sub-domains, Ω_{rte} and Ω_{da}. The RTE sub-domain included the CSF region pixels and the two pixel layers in the neighbourhood of the CSF

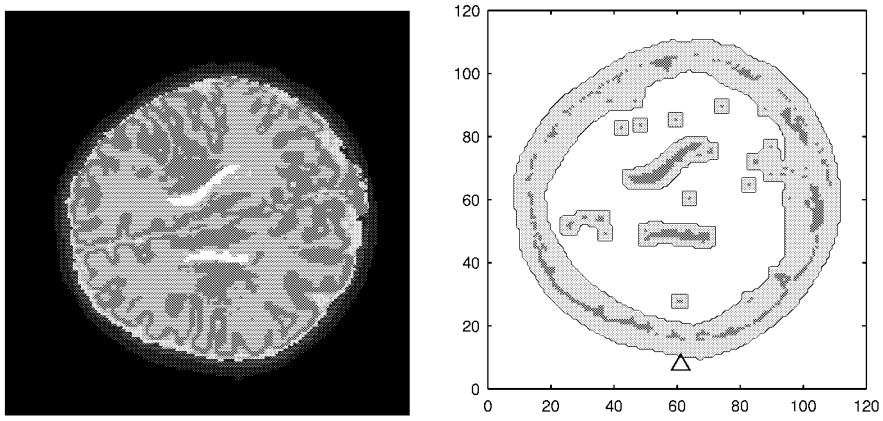

Figure 5.25: The left image: a segmented image from a new-born infant's head. The right image: the coupled RTE–DA model computation domain; the CSF regions (dark grey colour), the RTE sub-domain (light grey colour), and the DA sub-domain (white colour). The location of the light source is marked with a triangle.

Table 5.6: The absorption coefficient μ_a, the scattering coefficient μ_s, the scattering shape parameter g, and the reduced scattering coefficient μ_s' within the head slice.

	$\mu_a(\text{mm}^{-1})$	$\mu_s(\text{mm}^{-1})$	g	$\mu_s'(\text{mm}^{-1})$
Scalp:	0.018	4.75	0.6	1.9
Skull:	0.016	4	0.6	1.6
Grey matter:	0.048	1.25	0.6	0.5
White matter:	0.036	2.5	0.6	1
CSF around the brain:	0.0048	0.16	0.8	0.032
CSF in the ventricles:	0.0048	0.006	0.8	0.0012

regions as well as ten pixel layers in the neighbourhood of the boundary. The RTE sub-domain is illustrated in Figure 5.25 with light grey colour. The DA sub-domain covered the remaining domain. It is illustrated in Figure 5.25 with white colour. The FE-discretization was formed from the segmented image by splitting each image pixel into two triangular elements. The spatial FE-discretization consisted of 11631 nodal points (6141 in the RTE sub-domain and 5490 in the DA sub-domain) and 21607 triangular elements (11270 in the RTE sub-domain and 10337 in the DA sub-domain). In the angular discretization of the RTE, 32 angular

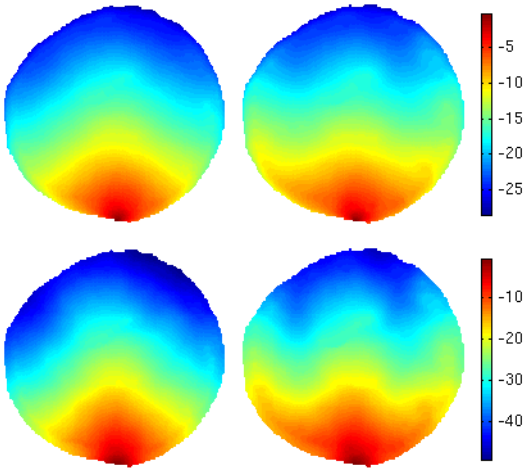

Figure 5.26: Logarithm of amplitude (top row) and phase shift (bottom row) of photon density within the head slice. The coupled RTE–DA model solution is on the left and the DA solution is on the right.

directions were used. In simulations, the source was located at the bottom of the computation domain. The location of the source is marked in Figure 5.25 with a small triangle. The coupled RTE–DA model was solved with the FEM as described in Section 4.3 with the streamline diffusion modification applied.

For comparison, the FE-solution of the DA was computed as described in Section 4.2 with the diffuse source model. The FE-solution of the DA was computed in the same spatial mesh as the FE-solution of the coupled RTE–DA model. The FE-solutions were compared with the results of Monte Carlo simulation. The Monte Carlo simulations were performed as in [109].

Results and discussion

The photon densities inside the head slice are shown in Figure 5.26. The coupled RTE–DA model solution is on the left and the DA solution is on the right. The logarithms of amplitudes are shown on the top row and the phase shifts are shown on the bottom row. The exitances on the boundary of the head slice are shown in Figure 5.27 which shows the exitances solved with the coupled RTE–DA model, the DA, and Monte Carlo. The logarithms of amplitudes are shown on the left and the phase shifts are shown on the right.

Examining the photon densities inside the domain shows that the photons tend to propagate further within the low-scattering CSF regions. This can be seen from Figure 5.26. The photon densities solved with the coupled RTE–DA model differ from the solutions of the DA. Based on the previous experience, it can expected

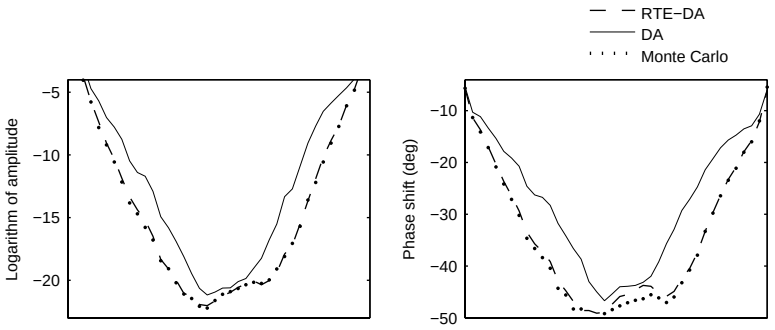

Figure 5.27: Logarithm of amplitude (on the left) and phase shift (on the right) of exitance on the boundary of the head slice.

that the coupled RTE–DA model describes light propagation more accurately than the DA.

Examining the exitances on the boundary of the domain and comparing the FE-solutions with the Monte Carlo simulations supports the results. The coupled RTE–DA model gives almost the same results as Monte Carlo. This can be seen from Figure 5.27 in which the logarithms of amplitudes and phase shifts of exitances on the boundary of the head slice are shown. The DA solution differs from the other approaches clearly.

5.4 Summary

In this chapter, light transport in various media was investigated with simulations. The validity of the FE-solutions of the RTE and the DA to describe light propagation in media with different optical properties were investigated. Further, the performance of the proposed hybrid approaches, namely the hybrid model and the coupled RTE–DA model were investigated. The FE-solutions of the DA and the proposed hybrid approaches were compared against the FE-solution of the RTE. In addition, the FE-solutions were compared with the results of the Monte Carlo simulations.

The FE-solutions of the RTE and the DA were investigated in homogeneous media with various optical properties. The results show that the FE-solution of the RTE gives almost the same results as the Monte Carlo simulation. Further, utilizing the streamline diffusion modification in the solution of the RTE, improves the FE-solution clearly. The results also show that the FE-solution of the DA differs from the solutions of the RTE and Monte Carlo in situations in which its approximations are not valid such as close to the source and within low-scattering medium. However, the DA gives almost the same results as the other approaches in highly scattering medium farther from the source. The two proposed hybrid approaches, the hybrid model and the coupled RTE–DA model, were solved with

the FEM in a homogeneous highly scattering medium. The simulations show that both of the hybrid approaches give almost the same results as the RTE and the Monte Carlo simulation within the whole domain. The DA solution, as mentioned earlier, differs from the other approaches close to the source. The performance of the coupled RTE–DA model was also investigated in highly scattering media with low-scattering and non-scattering regions and in a realistic head geometry with tissue-like optical properties. The results show that the FE-solution of the coupled RTE–DA model gives almost the same results as the RTE and Monte Carlo. In these situations, the DA solution differs from the other approaches clearly.

To conclude, the results show that the FE-solution of the RTE gives almost the same results as the Monte Carlo and it can be used to accurately describe light propagation in various media. The results also show that the DA can not describe light propagation accurately in situations in which the assumptions of the diffusion theory are not valid such as close to the source and within low-scattering medium. However, the DA can be regarded as a good approximative model for light transport in highly scattering medium farther from the source. In the situations in which the approximations of the DA are not valid, the hybrid approaches such as the hybrid model and the coupled RTE–DA model can be used as light transport models. The results show that these hybrid approaches describe light propagation almost as accurately as the RTE and Monte Carlo and with less computation cost than either of the methods.

Chapter VI

Computational calibration method

One of the key difficulties in optical tomography are the unknown amplitude losses and phase delays that are caused by the optic fibres and by the coupling effects between the object and the optic fibres. Unless these losses are efficiently calibrated or modelled, they can result in severe artefacts in the reconstructed images. Typically, the errors in optode modelling appear as absorption and scattering perturbations adjoint to the optodes.

One way to compensate for the optode losses is to use difference imaging. Difference imaging is known to produce images with few artefacts. However, it can not be used when absolute baseline optical properties are required, or when a reference measurement is not available [115]. Therefore, in order to obtain absolute images, an efficient calibration protocol is needed.

Methods for calibration of source and detector optode losses using calibration tools or other instrumentation based methods have been described for example in [115, 164, 169, 199]. However, accurate calibration of source and detector losses is difficult to implement on instrumentation level. Therefore, other model based methods have been developed. Methods, that use forward models and homogeneous phantom measurements for calibration have been described for example in [125, 158, 165] where the estimation of the optode losses is based on minimization of the least squares error between homogeneous phantom data and the diffusion approximation model. A method in which the amplitude losses were solved as part of the reconstruction problem was introduced in [43]. The method was further extended to correct small errors in optode positions [221] and phase delays [172]. The simultaneous image reconstruction and optode calibration is an efficient way to compensate optode losses but the method does not ensure absolute calibration and is computationally demanding. Further, the method may partially explain information in the data by the optode losses, leading to blurring of reconstructed targets that locate in the proximity of the optodes.

In this chapter, a computational method for calibration of frequency-domain optical tomography measurements is proposed. The model of the calibration scheme is based on the rotation symmetry of source and detector positions in the measurement setup. Rotation symmetric measurement setups are typically used in many applications of optical tomography, for example when a cylindrical

measurement cell is used. In the calibration model, the relative amplitude losses and phase shifts in the optic fibres are modelled by complex valued coupling coefficients. A similar type model for the calibration of continuous wave measurements has been presented previously in [201]. Here a model for the frequency-domain data is given and the calibration procedure is somewhat different from the method used in [201]. The proposed method has been utilized in [170] where a three-step method for the calibration of amplitude and phase measurements was described in order to define the absolute optical properties of the target.

In the proposed approach, the source and detector coupling coefficients are estimated using a calibration data which is measured from a homogeneous and isotropic material. Due to the simple calibration model, the estimation of the coupling coefficients is well-posed. Further, prior information about the optical properties of the calibration material or the strength of the light source are not needed in the estimation of the coupling coefficients. These facts make the estimation procedure simple, fast, and accurate. Once the coupling coefficients have been estimated from the calibration data, any data measured with the same measurement setup can be corrected for the relative variations in the data. That is, the coupling coefficients do not need to be redefined as long as the measurement setup remains unchanged.

This chapter is organized as follows. In Section 6.1, the calibration model is formulated and the estimation of the coupling coefficients is defined as a minimization problem. Then, the calibration of data by the estimated coupling coefficients and the initial estimation of the optical properties for reconstruction are discussed. In Section 6.2, an extended diffusion approximation model which includes the source and detector coupling coefficients and the corresponding FE-approximation are introduced. In Section 6.3, results of simulations and measurements are shown. In Section 6.4, conclusions are given.

6.1 Calibration method

6.1.1 Calibration model

Let $\Omega \subset \mathbb{R}^n$, $n = 2$ or 3 be a circular, cylindrical or spherical domain with boundary $\partial\Omega$. The medium Ω is assumed to be homogeneous and isotropic, i.e., the absorption and scattering coefficients are assumed to be constant within the medium and the scattering probability is assumed to depend only on the angle between incoming and outgoing directions. Furthermore, let m sources and m detectors be placed on circular symmetrical positions on the boundary of the domain. It should be noted that the number of the sources and the number of detectors does not need to be identical. However, that assumption is used here in order to simplify the notations. Further, in most applications of optical tomography the number of the sources and detectors is the same. In the sequel, the locations of the sources are denoted by ε_j, $j = 1, \ldots, m$ and the locations of the detectors are denoted by ζ_k, $k = 1, \ldots, m$.

Let us first assume that all sources and detectors are ideal in the sense that no amplitude losses or phase delays occur in the source and detector fibres. If light

is guided into the object via sources at $\varepsilon_1, \ldots, \varepsilon_m$ and is measured using detectors at $\zeta_1, \ldots, \zeta_m$, each time in that order, the measured frequency-domain data can be written in the form

$$Z = \begin{pmatrix} z_{1,1} & z_{2,1} & \cdots & z_{m,1} \\ z_{1,2} & z_{2,2} & & z_{m,2} \\ \vdots & & & \vdots \\ z_{1,m} & z_{2,m} & \cdots & z_{m,m} \end{pmatrix} = \begin{pmatrix} y_1 e^{\mathrm{i}\eta_1} & y_m e^{\mathrm{i}\eta_m} & \cdots & y_2 e^{\mathrm{i}\eta_2} \\ y_2 e^{\mathrm{i}\eta_2} & y_1 e^{\mathrm{i}\eta_1} & & y_3 e^{\mathrm{i}\eta_3} \\ \vdots & \vdots & & \vdots \\ y_m e^{\mathrm{i}\eta_m} & y_{m-1} e^{\mathrm{i}\eta_{m-1}} & \cdots & y_1 e^{\mathrm{i}\eta_1} \end{pmatrix} \tag{6.1}$$

where $z_{j,k}$ denotes measurement for source j and detector k. Thus, in the rotation symmetric setup, the measured amplitudes and phases are, in ideal case, equal when the angle between source and detector is equal. In the sequel we denote this ideal measurement vector by

$$\hat{y} = \left(y_1 e^{\mathrm{i}\eta_1}, \ldots, y_m e^{\mathrm{i}\eta_m}\right)^T \tag{6.2}$$

where y_i is the amplitude and η_i is the phase shift of the transmitted light with the source–detector angle index i.

In real measurements, unknown amount of amplitude loss and phase delay are caused by the source and detector fibres and by the coupling effects between the object and the optic fibres. In the following, these unknown losses are modelled by complex valued coupling coefficients. The model is written as

$$x_{j,k} = \hat{s}_j \hat{d}_k z_{j,k} = s_j e^{\mathrm{i}\sigma_j} d_k e^{\mathrm{i}\delta_k} z_{j,k} \tag{6.3}$$

where $x_{j,k}$ is the measurement for source–detector pair (j,k), $\hat{s}_j$ is the coupling coefficient of source (s_j is the source amplitude loss coefficient, σ_j is the source phase shift), $\hat{d}_k$ is the coupling coefficient of detector (d_k is the detector amplitude loss coefficient, δ_k is the detector phase shift), and $z_{j,k}$ is the ideal measurement as in equation (6.1).

Consider next the implementation of the model for the calibration data. In a typical optical tomography measurement, light is guided into the object via one of the source fibres at $\varepsilon_1, \ldots, \varepsilon_m$, and the transmitted light is measured using the detectors at $\zeta_1, \ldots, \zeta_m$. Let us concatenate the source coupling coefficients to a vector $\hat{s} = (s_1 e^{\mathrm{i}\sigma_1}, \ldots, s_m e^{\mathrm{i}\sigma_m})^T$, where $s = (s_1, \ldots, s_m)^T$ is the source amplitude loss coefficient and $\sigma = (\sigma_1, \ldots, \sigma_m)^T$ is the source phase shift. Similarly, let us concatenate the detector coupling coefficients to a vector $\hat{d} = (d_1 e^{\mathrm{i}\delta_1}, \ldots, d_m e^{\mathrm{i}\delta_m})^T$, where $d = (d_1, \ldots, d_m)^T$ is the detector amplitude loss coefficient and $\delta = (\delta_1, \ldots, \delta_m)^T$ is the detector phase shift. Exploiting the rotation symmetry of the ideal measurement $\hat{y}$, equation (6.2), the model for the calibration data can be written in

the form

$$
\begin{aligned}
X &= \begin{pmatrix} x_{1,1} & \dots & x_{m,1} \\ \vdots & \ddots & \vdots \\ x_{1,m} & \dots & x_{m,m} \end{pmatrix} \\
&= \begin{pmatrix} d_1 e^{\mathrm{i}\delta_1} & & \\ & \ddots & \\ & & d_m e^{\mathrm{i}\delta_m} \end{pmatrix} \begin{pmatrix} y_1 e^{\mathrm{i}\eta_1} & \dots & y_2 e^{\mathrm{i}\eta_2} \\ \vdots & \ddots & \vdots \\ y_m e^{\mathrm{i}\eta_m} & \dots & y_1 e^{\mathrm{i}\eta_1} \end{pmatrix} \begin{pmatrix} s_1 e^{\mathrm{i}\sigma_1} & & \\ & \ddots & \\ & & s_m e^{\mathrm{i}\sigma_m} \end{pmatrix} \\
&= DYS \qquad (6.4)
\end{aligned}
$$

where D and S are diagonal matrices that contain the detector and source coupling coefficients and Y is a matrix that contains the ideal measurements.

6.1.2 Estimation of the optode coupling coefficients

Given the model (6.4), the calibration problem is to estimate the unknown amplitude loss coefficients $(s_1, \dots, s_m)^T$ and $(d_1, \dots, d_m)^T$ and phase shifts $(\sigma_1, \dots, \sigma_m)^T$ and $(\delta_1, \dots, \delta_m)^T$ that occur in the source and detector fibres, and the amplitudes $(y_1, \dots, y_m)^T$ and the phase shifts $(\eta_1, \dots, \eta_m)^T$ of the transmitted light when a measured data from a homogeneous and isotropic object is given.

The problem is non-unique and therefore all calibration parameters describing amplitude losses and phase shifts can not be solved. To overcome the non-uniqueness problem, we form relative parameters as follows. We choose the coupling coefficients of the first source and the first detector as references and define the relative amplitude loss coefficients, $\tilde{s}_j$ and $\tilde{d}_j$, and the relative amplitudes $\tilde{y}_j$ of the transmitted light, as

$$\tilde{s}_j = \frac{s_j}{s_1}, \qquad j = 1, \dots, m \qquad (6.5)$$

$$\tilde{d}_j = \frac{d_j}{d_1}, \qquad j = 1, \dots, m \qquad (6.6)$$

$$\tilde{y}_j = y_j s_1 d_1 \qquad j = 1, \dots, m. \qquad (6.7)$$

Similarly, we define relative phase shifts, $\tilde{\sigma}_j$ and $\tilde{\delta}_j$, and relative phase shifts $\tilde{\eta}_j$ of the transmitted light as

$$\tilde{\sigma}_j = \sigma_j - \sigma_1, \qquad j = 1, \dots, m \qquad (6.8)$$

$$\tilde{\delta}_j = \delta_j - \delta_1, \qquad j = 1, \dots, m \qquad (6.9)$$

$$\tilde{\eta}_j = \eta_j + \sigma_1 + \delta_1, \qquad j = 1, \dots, m. \qquad (6.10)$$

Now, based on the definitions in (6.5)–(6.10), the relative amplitude loss coefficient and phase shift of the first source are $\tilde{s}_1 = 1$ and $\tilde{\sigma}_1 = 0$. Similarly, the relative amplitude loss coefficient and phase shift of the first detector are $\tilde{d}_1 = 1$ and $\tilde{\delta}_1 = 0$. Using the relative parameters defined in equations (6.5)–(6.10), the data

(6.4) can be written in the form

$$X = \begin{pmatrix} 1 & & & \\ & \tilde{d}_2 e^{\mathrm{i}\tilde{\delta}_2} & & \\ & & \ddots & \\ & & & \tilde{d}_m e^{\mathrm{i}\tilde{\delta}_m} \end{pmatrix} \begin{pmatrix} \tilde{y}_1 e^{\mathrm{i}\tilde{\eta}_1} & \dots & & \tilde{y}_2 e^{\mathrm{i}\tilde{\eta}_2} \\ \tilde{y}_2 e^{\mathrm{i}\tilde{\eta}_2} & \ddots & & \tilde{y}_3 e^{\mathrm{i}\tilde{\eta}_3} \\ \vdots & & \ddots & \vdots \\ \tilde{y}_m e^{\mathrm{i}\tilde{\eta}_m} & \dots & & \tilde{y}_1 e^{\mathrm{i}\tilde{\eta}_1} \end{pmatrix} \times \begin{pmatrix} 1 & & & \\ & \tilde{s}_2 e^{\mathrm{i}\tilde{\sigma}_2} & & \\ & & \ddots & \\ & & & \tilde{s}_m e^{\mathrm{i}\tilde{\sigma}_m} \end{pmatrix} = \tilde{D}\tilde{Y}\tilde{S}. \tag{6.11}$$

The calibration problem is now to estimate the relative source and detector amplitude loss coefficients $(\tilde{s}_2, \dots, \tilde{s}_m)^T$ and $(\tilde{d}_2, \dots, \tilde{d}_m)^T$, the relative source and detector phase shifts $(\tilde{\sigma}_2, \dots, \tilde{\sigma}_m)^T$ and $(\tilde{\delta}_2, \dots, \tilde{\delta}_m)^T$, the relative amplitudes $(\tilde{y}_1, \dots, \tilde{y}_m)^T$ and the relative phase shifts $(\tilde{\eta}_1, \dots, \tilde{\eta}_m)^T$ of the transmitted light when the measured data from a homogeneous and isotropic object is given.

The relative amplitude loss and phase shift parameters can be estimated in the least squares sense by minimizing the functional

$$\Psi = \left\| L \left(\begin{pmatrix} |\Gamma_0| \\ \arg(\Gamma_0) \end{pmatrix} - \begin{pmatrix} |X(\tilde{y}, \tilde{s}, \tilde{d})| \\ \arg(X(\tilde{\eta}, \tilde{\sigma}, \tilde{\delta})) \end{pmatrix} \right) \right\|_2^2 \tag{6.12}$$

where $|\Gamma_0|$ and $\arg(\Gamma_0)$ contain the amplitudes and phase shifts of the measured calibration data in vector form, respectively, and $|X(\tilde{y}, \tilde{s}, \tilde{d})|$ and $\arg(X(\tilde{\eta}, \tilde{\sigma}, \tilde{\delta}))$ are the amplitude and phase shift vectors that are obtained from the solution of the model (6.11). The matrix L is a weight matrix which basically corresponds to the Cholesky factor of the inverse of the noise covariance matrix. In optical tomography, where the dynamic range of the measured light intensities is often very large, scaling of the data may be needed in order to ensure numerical stability of the optimization algorithm. In such case, the weight matrix is often chosen as a diagonal matrix

$$L = \operatorname{diag} \begin{pmatrix} |\Gamma_0| \\ \arg(\Gamma_0) \end{pmatrix}^{-1}. \tag{6.13}$$

The minimization problem (6.12) can be solved, for example, with the Gauss–Newton method that can be written in the form

$$\theta_{i+1} = \theta_i + c_i (J_i^T W J_i)^{-1} J_i^T W \left(\begin{pmatrix} |\Gamma_0| \\ \arg(\Gamma_0) \end{pmatrix} - \begin{pmatrix} |X(\theta_i)| \\ \arg(X(\theta_i)) \end{pmatrix} \right) \tag{6.14}$$

where $\theta = (\tilde{y}_1, \dots, \tilde{y}_m, \tilde{s}_2, \dots, \tilde{s}_m, \tilde{d}_2, \dots, \tilde{d}_m, \tilde{\eta}_1, \dots, \tilde{\eta}_m, \tilde{\sigma}_2, \dots, \tilde{\sigma}_m, \tilde{\delta}_2, \dots, \tilde{\delta}_m)^T \in \mathbb{R}^{6m-4}$ is the vector of unknown parameters, $X(\theta_i)$ implements the calibration model (6.11) in vector form, c_i is a step length parameter, $W = L^T L$, and matrix J_i is the Jacobian for $|X(\theta_i)|$ and $\arg(X(\theta_i))$.

In some cases data can not be measured from all the detectors because of too large dynamic range of the light intensities, and thus the coupling coefficient estimation problem may become ill-posed. In such cases, one possibility is to solve the problem (6.12) using the Levenberg–Marquardt algorithm that can be written in the form

$$\theta_{i+1} = \theta_i + c_i(J_i^T W J_i + \lambda I)^{-1} J_i^T W \left(\begin{pmatrix} |\Gamma_0| \\ \arg(\Gamma_0) \end{pmatrix} - \begin{pmatrix} |X(\theta_i)| \\ \arg(X(\theta_i)) \end{pmatrix} \right) \tag{6.15}$$

where λ is a Levenberg–Marquardt stabilization parameter and I is an identity matrix [159, 235].

6.1.3 Calibration

Once the relative source and detector amplitude losses and phase shifts have been estimated, any data that has been measured using the same measurement setup can be calibrated for the relative variations in the data due to the source and detector losses. The calibration of the measurement data is based on equation (6.11) and it is obtained by dividing the measured data Γ by the estimated relative source and detector coupling coefficients. Assuming that the data Γ is arranged in matrix form as in equation (6.11), the calibrated data $\tilde{\Gamma}$ is obtained by

$$\tilde{\Gamma} = \tilde{D}^{-1} \Gamma \tilde{S}^{-1} \tag{6.16}$$

where $\tilde{D}$ is a diagonal matrix that contains the estimated relative detector coupling coefficients $\tilde{d}_k e^{\mathrm{i}\tilde{\delta}_k}$ and $\tilde{S}$ is a diagonal matrix that contains the estimated relative source coupling coefficients $\tilde{s}_j e^{\mathrm{i}\tilde{\sigma}_j}$.

6.1.4 Initialization for reconstruction

The calibration (6.16) corrects the data only for the relative variations in amplitude losses and phase shifts in the source and detector fibres. Thus, the calibrated data $\tilde{\Gamma}$ in equation (6.16) contain a constant multiplicative bias $s_1 d_1$ in amplitude and a constant additive bias $\sigma_1 + \delta_1$ in phase, that are due to using the relative amplitude loss and phase shift coefficients in the calibration. Furthermore, often in practical optical tomography experiments, the relation between the source model in the forward model and the strength and initial phase of the source in the experimental device is not known. These unknown biases in the amplitude and phase should be estimated and removed from the calibrated data $\tilde{\Gamma}$ before reconstruction. Let us denote the unknown bias in the amplitude by ϑ and the unknown bias in the phase by ξ. Further, let

$$|\tilde{\Gamma}| = \vartheta \mathcal{F}_{\mathrm{mod}}(\mu_a, \mu_s) \tag{6.17}$$

$$\arg(\tilde{\Gamma}) = \mathcal{F}_{\arg}(\mu_a, \mu_s) + \xi. \tag{6.18}$$

denote the forward models $\mathcal{F}$ that map the absorption and scattering parameters (μ_a, μ_s) to the vectors of amplitude and phase shift data $\tilde{\Gamma}$. The most often used forward models in optical tomography are the RTE and the DA, as described in

Chapter 3. The unknown biases in amplitude and phase data can be estimated, for example, by minimizing the least squares errors between the calibrated data and computed data obtained with the models (6.17) and (6.18).

Due to the ill-posed nature of the optical tomography problem, the initial values of the optical properties for the image reconstruction algorithm need to be reasonably close to the actual (heterogeneous) optical properties in order to guarantee fast convergence in image reconstruction. One possible solution for the initialization is to initialize the absorption and scattering images to global parameter values $(\mu_{a,0}, \mu_{s,0})$ that are obtained as a minimizer of the least squares error between the measured and computed data.

Using the models (6.17) and (6.18), the final calibration and the initial estimation can be defined as finding the parameter vector $(\mu_{a,0}, \mu_{s,0}, \vartheta, \xi)^{\mathrm{T}} \in \mathbb{R}^4$ that minimize the functional

$$\Psi = \left\| L\left(\begin{pmatrix} |\tilde{\Gamma}| \\ \arg(\tilde{\Gamma}) \end{pmatrix} - \begin{pmatrix} \vartheta \mathcal{F}_{\mathrm{mod}}(\mu_{a,0}, \mu_{s,0}) \\ \mathcal{F}_{\arg}(\mu_{a,0}, \mu_{s,0}) + \xi \end{pmatrix} \right) \right\|_2^2 \tag{6.19}$$

where vectors $|\tilde{\Gamma}|$ and $\arg(\tilde{\Gamma})$ contain the amplitudes and phase shifts of the calibrated data, respectively. Once the problem (6.19) has been solved, one can remove the estimated bias (ϑ, ξ) from the calibrated data by

$$|\tilde{\Gamma}_{\mathrm{c}}| = \vartheta^{-1} |\tilde{\Gamma}| \tag{6.20}$$

$$\arg(\tilde{\Gamma}_{\mathrm{c}}) = \arg(\tilde{\Gamma}) - \xi \tag{6.21}$$

and compute the reconstructions using the estimated parameters $(\mu_{a,0}, \mu_{s,0})$ as the starting point in the image reconstruction algorithm.

6.2 Extended diffusion approximation

The source and detector coupling coefficients can also be included in the diffusion approximation model for OT measurements. In this section, an extended DA model, that includes the source and detector coupling coefficients, and the finite element discretization of the model are discussed. The model is used to generate data for simulations in Section 6.3.

As explained in Section 3.2, the frequency-domain version of the DA assumes the form (3.29) with the Robin type boundary condition (3.37). The light sources at $\partial\Omega$ are usually modelled in the DA either by the collimated source model or the diffuse source model. In case of the collimated source model, the light source is modelled as an isotropic point source located at a depth $(1/\mu_s')$ below the source site. Including the source coupling coefficient, the collimated source model (3.39) assumes the form

$$q_0(r) = \hat{s}_j \delta(r - r_s) \tag{6.22}$$

where $\hat{s}_j = s_j e^{\mathrm{i}\sigma_j}$ is the coupling coefficient of the source at ε_j as described in Section 6.1. In case of the diffuse source model, the light source is modelled as

an inward directed diffuse boundary current I_s at the source site ε_j. The boundary condition (3.41) with the diffuse source model including the source coupling coefficient $\hat{s}_j$ can be written as

$$\Phi(r) + \frac{1}{2\gamma_n}\kappa A\frac{\partial\Phi(r)}{\partial\hat{n}} = \begin{cases} \frac{\hat{s}_j I_s}{\gamma_n}, & r \in \cup_j \varepsilon_j \\ 0, & r \in \partial\Omega \setminus \cup_j \varepsilon_j. \end{cases} \tag{6.23}$$

In case of the DA, the measurable quantity, the exitance $\Gamma(r)$, is as in equation (3.38). Including the detector coupling coefficient, the exitance can be written in the form

$$\Gamma(r) = -\hat{d}_k\kappa\frac{\partial\Phi(r)}{\partial\hat{n}} = \frac{2\hat{d}_k\gamma_n}{A}\Phi(r) \tag{6.24}$$

where $\hat{d}_k = d_k e^{\mathrm{i}\delta_k}$ is the coupling coefficient of the detector at ζ_k.

6.2.1 FE-approximation of the extended DA

The FE-approximation of the DA was presented in Section 4.2. Here, the FE-approximation for the extended DA is given. It can be derived similarly as the FE-approximation of the DA in Section 4.2. Accordingly, the solution $\Phi(r)$ of the variational formulation of the DA, is approximated in a piecewise linear basis (4.29). The FE-approximation of the extended DA can be written as

$$(K + C + R + Z)\,a = \tilde{G} + \tilde{E} \tag{6.25}$$

where K, C, R, and Z are as in equations (4.31)–(4.34). The source vectors on the right hand side of equation (6.25) depend on the source model that is used. In case of the collimated source model (6.22), the source vectors $\tilde{G}$ and $\tilde{E}$ are of the form

$$\tilde{G} = 0 \tag{6.26}$$

$$\tilde{E}(p) = s_j e^{\mathrm{i}\sigma_j}\int_\Omega \delta(r - r_s)\varphi_p(r)\mathrm{d}r \tag{6.27}$$

and in case of the diffuse source model,

$$\tilde{G}(p) = s_j e^{\mathrm{i}\sigma_j}\int_{\partial\Omega}\frac{2I_s}{A}\varphi_p(r)\mathrm{d}S \tag{6.28}$$

$$\tilde{E} = 0 \tag{6.29}$$

where $p = 1, \ldots, N$ and N is the number of the nodal points in the FE-discretization.

6.3 Results

The calibration method was tested with simulations and measurements. In simulations, the validity of the source and detector coupling coefficient estimation method was tested and the effect of the calibration on data and reconstructed images were inspected. With the measurements, the effect of the calibration on measured data and quality of reconstructed images were investigated.

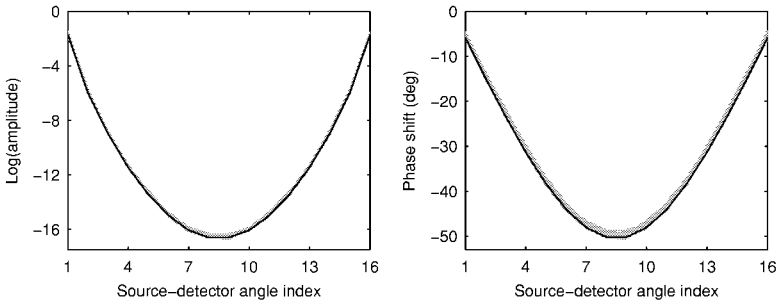

Figure 6.1: Logarithm of amplitude (left image) and phase shift (right image) of simulated data against the source–detector angle index. The uncalibrated data is plotted with grey lines and the calibrated data is plotted with black lines.

6.3.1 Simulation results

In simulations, a two-dimensional ($n = 2$) case was considered. The medium $\Omega \subset \mathbb{R}^2$ was a circular domain with radius $r = 25\,\text{mm}$. 16 equally spaced sources and 16 equally spaced detectors located on the boundary of the domain. The absorption coefficient and the (reduced) scattering coefficient were chosen as $\mu_a = 0.025\,\text{mm}^{-1}$ and $\mu_s' = 2\,\text{mm}^{-1}$. The modulation frequency of the input signal was $f = 100\,\text{MHz}$. The source and detector amplitude loss coefficients were generated randomly from uniform distribution [0.75 1], and the source and detector phase shifts were generated randomly from uniform distribution $[-1.5°\ 0°]$. The data was generated with the FE-model for the extended DA with the collimated source model, see equations (6.24)–(6.27). The FE-discretization contained 58238 triangular elements and 30704 nodal points. The amplitude and phase shift of the simulated data against the source–detector angle index are plotted in Figure 6.1 with grey curves.

Calibration

The relative source and detector coupling coefficients and transmitted light intensities were solved by minimizing the functional (6.12) with the choice $L = I$ where I is an identity matrix. The minimization problem was solved by the Gauss–Newton algorithm (6.14). The convergence was achieved in three iterations. The relative source and detector amplitude loss coefficients and phase shifts and the corresponding estimated values are shown in Figure 6.2. The data was calibrated using equation (6.16). The amplitudes and phase shifts of the data against the source–detector angle index before and after calibration are shown in Figure 6.1.

The results show that the relative source and detector coupling coefficients can be estimated with good accuracy. The simulated and estimated values are almost equal which can be seen from Figure 6.2. The maximum relative error

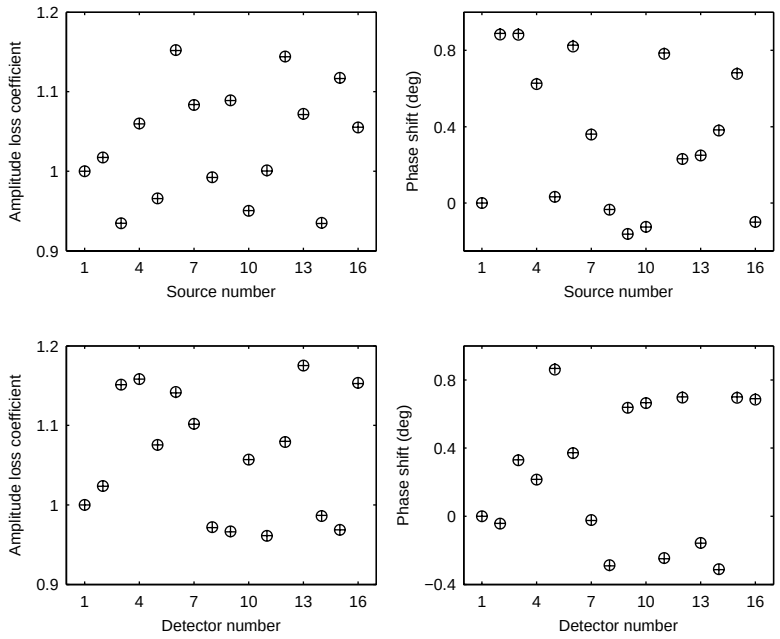

Figure 6.2: Top row: relative source amplitude loss coefficient (left image) and phase shift (right image) marked with (+) and the corresponding estimated values marked with (∘). Bottom row: relative detector amplitude loss coefficient (left image) and phase shift (right image) marked with (+) and the corresponding estimated values marked with (∘).

of the estimated coupling coefficients was approximately 1%. As explained in Section 6.1, in a rotation symmetric setup the measured amplitudes and phase shifts should be equal with the same source–detector angle index in an ideal case when there are no source and detector amplitude losses and phase delays. As it can be seen from Figure 6.1, the calibration compensates for the amplitude losses and phase delays in the data, and thus the calibrated data has much less variation between the sources and detectors compared with the uncalibrated data.

Reconstructions

To test the effect of the calibration on the quality of reconstructed images, another data was generated using the same measurement setup. Now, the medium contained two circular inclusions. The absorption and scattering coefficients of the inclusions were $(\mu_a, \mu_s') = (0.05, 2)\,\mathrm{mm}^{-1}$ and $(\mu_a, \mu_s') = (0.025, 5)\,\mathrm{mm}^{-1}$. The simulated absorption and scattering distributions are shown in the left column of Figure 6.3.

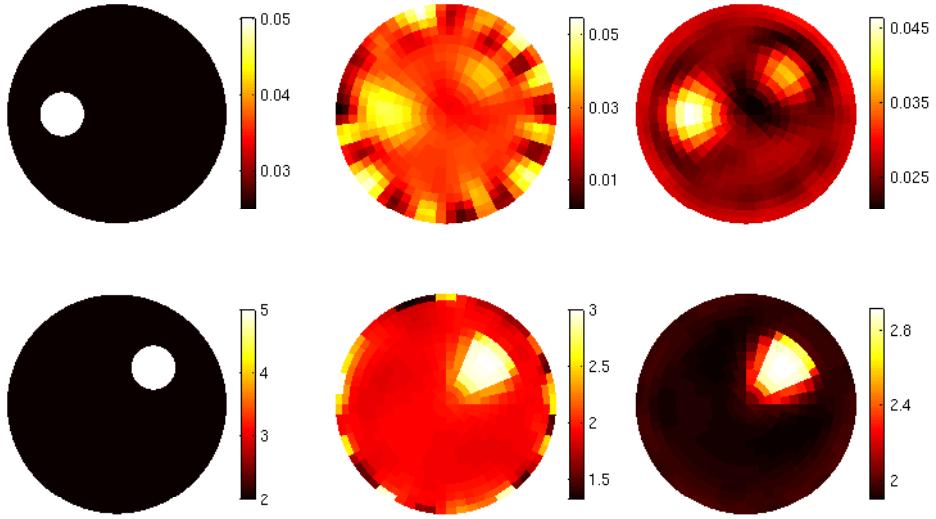

Figure 6.3: Absorption coefficients (top row) and scattering coefficients (bottom row). From left to right: simulated distributions, reconstructions from uncalibrated data, and reconstructions from calibrated data.

The data was calibrated with equation (6.16) using the previously estimated relative coupling coefficients. Then, the initial values of absorption and scattering coefficients $(\mu_{a,0}, \mu'_{s,0})$, and the systematic biases (ϑ, ξ) in the calibrated data were estimated by minimization of functional (6.19). In the minimization, the forward model $\mathcal{F}$ was based on the FE-approximation of the "conventional" diffusion approximation, see Section 4.2. The weight matrix was chosen similarly as in equation (6.13), thus $L = \mathrm{diag}(\tilde{\Gamma})^{-1}$. The functional (6.19) was minimized by a Gauss-Newton algorithm that was equipped with an explicit line search algorithm for the determination of the step length. The estimated biases (ϑ, ξ) were removed from the calibrated data $\tilde{\Gamma}$ using equations (6.20) and (6.21). Finally, the absorption and scattering reconstructions were computed with a total variation regularized output least squares scheme similar to the method described in [145] using the estimated $(\mu_{a,0}, \mu'_{s,0})$ as the starting point in the reconstruction algorithm. For comparison, absorption and scattering distributions were reconstructed from the uncalibrated data as well. The reconstructed absorption and scattering distributions are shown in Figure 6.3 where the middle column shows the reconstructions from uncalibrated data and the right column shows the reconstructions from calibrated data.

As it can be seen from Figure 6.3, the calibration improves the quality of the reconstructed images significantly. Whereas the reconstructions from the uncalibrated data are unclear with large perturbations near the boundary, the recon-

structions from the calibrated data are clear and the inclusions are well distinguished. Some crosstalk between the scattering and absorption appears in the reconstructions. This, however, is typical for optical tomography reconstructions.

6.3.2 Measurement results

Measurements were performed using MONSTIR (multichannel optoelectronic near-infrared system for time-resolved image reconstruction) imaging system of the Biomedical Optics Research Laboratory at the University College London. A detailed description of the system and data acquisition protocol can be found in [199].

Measurements with homogeneous cylindrical phantom were performed to obtain the data for the calibration. The height of the phantom was 14 cm and the diameter was 7 cm. The absorption coefficient of the phantom was approximately $\mu_a = 0.01\,\mathrm{mm}^{-1}$ and the (reduced) scattering coefficient was approximately $\mu_s' = 1\,\mathrm{mm}^{-1}$. The refractive index was $n_{\mathrm{in}} = 1.56$. A plastic ring was used to hold the 16 sources and 16 detectors in contact with the phantom. A data acquisition protocol, that ensured that the photon current did not exceed maximum value allowed in each channel, was performed. Therefore measurements were not made on detectors closest to each source. The frequency-domain data was obtained by Fourier transforming the measured time-domain data. Data corresponding to input signal modulation frequency $f = 100\,\mathrm{MHz}$ was chosen.

Calibration

The relative source and detector coupling coefficients and transmitted light intensities were estimated by minimizing functional (6.12) with the weight matrix L as in equation (6.13). The minimization problem was solved by the Levenberg–Marquardt algorithm (6.15) with the stabilization parameter $\lambda = 0.001$. The convergence was achieved in three iterations. The measured data was calibrated with equation (6.16) using the estimated coupling coefficients. The amplitudes and phase shifts of the measured data against the source–detector angle index for the uncalibrated data and the calibrated data are shown in Figure 6.4.

A clear difference in variation of the amplitudes of uncalibrated and calibrated data can be seen. This indicates that the calibration is correcting for the amplitude losses of sources and detectors. On the other hand, the calibration does not seem to have a significant impact on phase shifts. We expect that this is because the phase shifts of the sources and detectors are already efficiently treated by the data acquisition protocol of the MONSTIR system, and therefore the quality of the phase data is already good.

Reconstructions

The effect of the calibration on the quality of reconstructed images was investigated. Therefore, another measurement was carried out with the same measurement setup. Now, two small cylinders were placed inside the phantom. The absorption and scattering coefficients of the cylinders were approximately

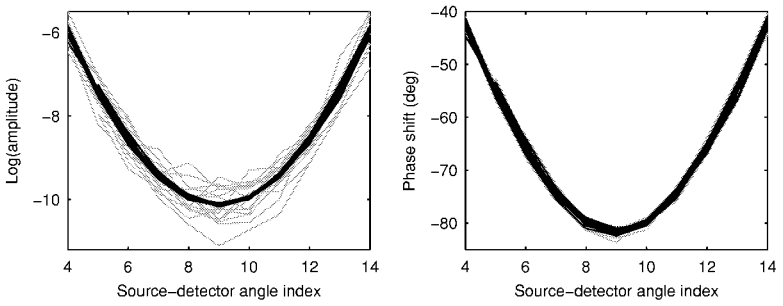

Figure 6.4: Logarithm of amplitude (left image) and phase shift (right image) of measured data against the source–detector angle index. The uncalibrated data is plotted with grey lines and the calibrated data is plotted with black lines.

$(\mu_a, \mu_s') = (0.05, 1)\,\mathrm{mm}^{-1}$ and $(\mu_a, \mu_s') = (0.01, 5)\,\mathrm{mm}^{-1}$. The cylinders located at the same height as the plastic ring holding the sources and detectors. The measurements were carried out similarly as for the homogeneous phantom. The measured data was calibrated with equation (6.16) using the previously estimated relative coupling coefficients, and the initialization was performed as explained in Section 6.1.4. The 3D reconstructions were carried out with the frequency-domain version of TOAST (time-resolved optical absorption and scattering tomography) software of the Biomedical Optics Research Laboratory at the University College London [23]. Three types of images were reconstructed: a difference image, an absolute image from uncalibrated data, and an absolute image from calibrated data. The difference image was obtained by using the data from the homogeneous phantom as a reference data and by adding the calculated difference to the reference values.

The reconstructed absorption and scattering distributions on the horizontal layer in which the sources and detectors were located are shown in Figure 6.5. The absolute reconstructions from the uncalibrated data contain severe perturbations near the boundaries of the domain, and the locations of the inclusions are not well distinguished. The absolute images from the calibrated data are better than those from uncalibrated data. The inclusions are distinguished more clearly and the amount of reconstruction artefacts has decreased significantly. Thus, calibration improves the quality of the absolute images.

6.4 Conclusions

A computational calibration method for optical tomography was proposed. The model of the calibration scheme is based on rotation symmetry of the source and detector positions in the measurement setup. The relative amplitude losses and phase shifts in the optic fibres are modelled by complex valued coupling coefficients. The relative coupling coefficients can be estimated when data from a homogeneous

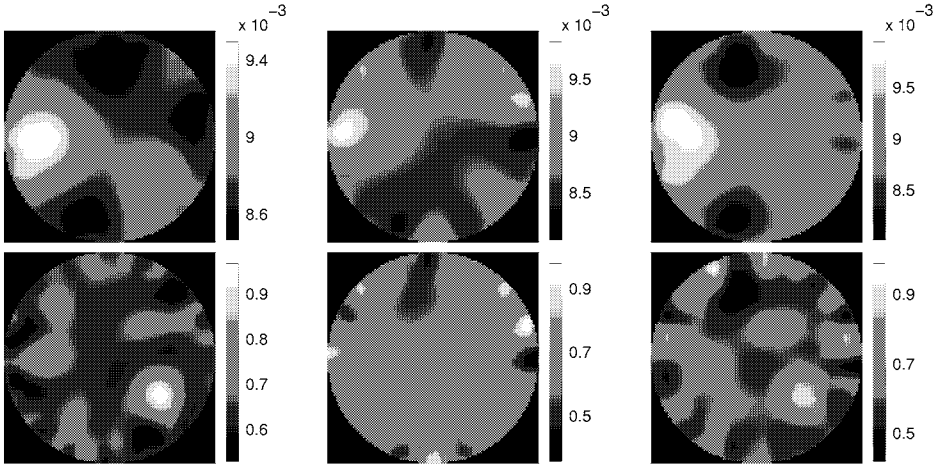

Figure 6.5: Absorption coefficients (top row) and scattering coefficients (bottom row). From left to right: difference images, absolute images from uncalibrated data, and absolute images from calibrated data.

and isotropic object is given. Once the relative coupling coefficients have been estimated, any data measured with the same measurement setup can be calibrated.

The method was tested with simulations and measurements. The results show that the calibration method can reduce the effects of the unknown amplitude losses and phase delays occurring in source and detector fibres. Thus, the method can improve the quality of reconstructed images significantly. Therefore, the proposed approach offers a simple and accurate method for calibration of optical tomography measurements.

Chapter VII

Conclusions

In this thesis, modelling approaches to the forward problem of optical tomography were investigated. Light transport within the object and in the optic fibres of OT measurements were described through two approaches. Firstly, modelling light propagation in tissues through transport theory was discussed and two new hybrid approaches to describe light transport in tissues were proposed in Chapter 3. The corresponding FE-implementations of the light transport models were given in Chapter 4 and they were tested with 2D simulations in Chapter 5. Secondly, a computational method for calibration of OT measurements was proposed in Chapter 6.

In optical tomography, two models, the radiative transfer equation and the diffusion approximation, have been used as the forward models to describe light propagation in tissues. The RTE is widely accepted as an accurate model to describe light transport in tissues. However, in many cases, the RTE is computationally too demanding to be used in practical applications and approximate models are applied. The most often used forward model in OT is the diffusion approximation. The DA describes light propagation accurately in the highly scattering medium. However, it does not describe light transport accurately in situations in which the assumptions of the diffusion theory are not valid such as close to the highly collimated light sources and within low-scattering and non-scattering medium such as the cerebrospinal fluid.

The purpose in the thesis was to develop new forward models which describe light propagation in tissues accurately and which are computationally less demanding than the RTE. In the thesis, two new hybrid approaches to describe light propagation in tissues were proposed. The approaches are the hybrid model and the coupled RTE–DA model and they utilize both the RTE and the DA in the solution of the forward problem.

The hybrid model can be utilized in highly scattering medium such as the breast tissue. It was developed to correct the inaccuracy of the diffusion theory close to the sources. In the hybrid model, light propagation is modelled with the RTE close to the light sources and the DA is used elsewhere in the domain. The solution of the RTE is used to construct a Dirichlet boundary condition for the DA on a fictitious interface within the object. This boundary condition constitutes a

distributed source model for the DA in the remaining area.

In the coupled RTE–DA model, light propagation is modelled with the RTE in sub-domains in which the assumptions of the DA are not valid and the DA is used elsewhere in the domain. The two equation are coupled through boundary conditions between the RTE and DA sub-domains. Compared to the hybrid model, the coupled RTE–DA model does not neglect the backscattering between the RTE and DA sub-domains. In addition, whereas the hybrid model was developed to eliminate the inaccuracy of the diffusion theory close to the sources, the coupled RTE–DA model can also be used in other situations in which the assumptions of the DA are not valid, that is within low-scattering regions and near the domain boundary.

The RTE, the DA, the hybrid model, and the coupled RTE–DA model were implemented with the finite element method. The methods were tested with 2D simulations in different domains with various optical properties. The results were compared with each other and with the results of Monte Carlo simulations. The results show that the FEM can be used to solve the RTE accurately. In addition, the FE-solution of the RTE can be stabilized if sophisticated numerical methods are applied. Furthermore, the results show that the DA can describe light propagation accurately in situations in which the assumptions of the diffusion theory are valid. However, in situations in which the approximations of the DA are not valid, the DA solution differs from the other approaches. Based on the results, the proposed hybrid model and coupled RTE–DA model seem promising light transport models. The results show that the hybrid approaches can be used to describe light propagation in various media accurately, and that they can be applied in situations in which the approximations of the DA are not valid. Further, according to the simulations, the hybrid approaches can be solved with significantly less computation costs than the RTE.

In addition to the target tissue, light propagation in OT measurements is also affected by the optic fibres and by the coupling effects between the object and the optic fibres. These coupling effects cause unknown amplitude losses and phase delays to the measurement signal. Unless these losses are efficiently calibrated or modelled, they can result in severe artefacts in the reconstructed images. In the thesis, a computational method for calibration of frequency-domain OT measurements was proposed. The model of the calibration scheme is based on the rotation symmetry of source and detector positions in the measurement setup. The relative amplitude losses and phase shifts at the optic fibres are modelled by complex valued coupling coefficients which can be estimated when data from a homogeneous and isotropic object is given. The calibration method was tested with simulations and measurements. According to results, the calibration method reduces the effects of the unknown amplitude losses and phase delays occurring in source and detector fibres. Furthermore, the method improves the quality of reconstructed images significantly.

In future, the developed approaches will be utilized in the inverse problem of optical tomography. The hybrid methods will be implemented in three-dimensional geometry and they will be utilized in the image reconstruction of OT. The de-

veloped hybrid approaches can be expected to lead to computationally feasible solutions. Furthermore, the methods can be expected to improve the quality of the reconstructed images when compared to the reconstructions based on the conventional diffusion model. The computational calibration method will be utilized in the calibration of OT measurements. The method has already been utilized in a three-step calibration method of amplitude and phase measurements [170] which was developed in order to define the absolute optical properties of the target through OT measurements.

[1] G.S. Abdoulaev and A.H. Hielscher. Three-dimensional optical tomography with the equation of radiative transfer. *J Electron Imaging*, 12(4):594–601, 2003.

[2] R.T. Ackroyd. *Finite Element Methods for Particle Transport: Applications to Reactor and Radiation Physics.* Research Studies Press, Taunton, 1997.

[3] G. Alexandrakis, D.R. Busch, G.W. Faris, and M.S. Patterson. Determination of the optical properties of two-layer turbid media by use of a frequency-domain hybrid Monte Carlo diffusion model. *Appl Opt*, 40(22):3810–3821, 2001.

[4] G. Alexandrakis, T.J. Farrrell, and M.S. Patterson. Accuracy of the diffusion approximation in determining the optical properties of a two-layer turbid medium. *Appl Opt*, 37(31):7401–7409, 1998.

[5] G. Alexandrakis, T.J. Farrrell, and M.S. Patterson. Monte Carlo diffusion hybrid model for photon migration in a two-layer turbid medium in the frequency domain. *Appl Opt*, 39(13):2235–2244, 2000.

[6] E. Amaldi. The production and slowing down of neutrons. In S. Flügge, editor, *Encyclopedia of Physics*, volume 38/2, pages 1–659, Springer-Verlag, Berlin, 1959.

[7] G. Arfken. *Mathemathical Methods for Physicists.* Academic Press, San Diego, 1985.

[8] R. Aronson. Boundary conditions for diffusion of light. *J Opt Soc Am A*, 12:2532–2539, 1995.

[9] R. Aronson and N. Corngold. Photon diffusion coefficient in an absorbing medium. *J Opt Soc Am A*, 16(5):1066–1071, 1999.

[10] S.R. Arridge. Photon measurement density functions. Part 1: Analytical forms. *Appl Opt*, 34(31):7395–7409, 1995.

[11] S.R. Arridge. Optical tomography in medical imaging. *Inv Probl*, 15:R41–R93, 1999.

[12] S.R. Arridge, M. Cope, and D.T. Delpy. The theoretical basis for the determination of optical pathlengths in tissue: temporal and frequency analysis. *Phys Med Biol*, 37(7):1531–1560, 1992.

[13] S.R. Arridge, H. Dehghani, M. Schweiger, and E. Okada. The finite element model for the propagation of light in scattering media: A direct method for domains with nonscattering regions. *Med Phys*, 27(1):252–264, 2000.

[14] S.R. Arridge and J.C. Hebden. Optical imaging in medicine: II. Modelling and reconstruction. *Phys Med Biol*, 42:841–853, 1997.

[15] S.R. Arridge, M. Hiraoka, and M. Schweiger. Statistical basis for the determination

of optical pathlength in tissue. *Phys Med Biol*, 40:1539–1558, 1995.

[16] S.R. Arridge and W.R.B. Lionheart. Nonuniqueness in diffusion-based optical tomography. *Opt Lett*, 23:882–884, 1998.

[17] S.R. Arridge and M. Schweiger. Direct calculation of the moments of the distribution of photon time of flight in tissue with a finite-element method. *Appl Opt*, 34(15):2683–2687, 1995.

[18] S.R. Arridge and M. Schweiger. Photon measurement density functions. Part 2: Finite-element-method calculations. *Appl Opt*, 34(34):8026–8037, 1995.

[19] S.R. Arridge and M. Schweiger. A general framework for iterative reconstruction algorithms in optical tomography, using a finite element method. In C. Borgers and F. Natterer, editors, *Computational Radiology and Imaging: Therapy and Diagnosis*, volume 110 of *IMA Volumes in Mathematics and its Applications*, pages 45–70, IMA, Springer-Verlag, 1998.

[20] S.R. Arridge and M. Schweiger. A gradient-based optimisation scheme for optical tomography. *Opt Express*, 2(6):213–226, 1998.

[21] S.R. Arridge, M. Schweiger, M. Hiraoka, and D.T. Delpy. A finite element approach for modeling photon transport in tissue. *Med Phys*, 20(2):299–309, 1993.

[22] S.R. Arridge, J.P. Kaipio, V. Kolehmainen, M. Schweiger, E. Somersalo, T. Tarvainen, and M. Vauhkonen. Approximation errors and model reduction with an application in optical diffusion tomography. *Inv Probl*, 22:175–195, 2006.

[23] S.R. Arridge and M. Schweiger. The UCL optical tomography software system (TOAST). available at http://www.medphys.ucl.ac.uk/∼ martins/toast/index.html, 2004.

[24] E.D. Aydin, C.R.E. de Oliveira, and A.J.H. Goddard. A comparison between transport and diffusion calculations using a finite element-spherical harmonics radiation transport method. *Med Phys*, 29(9):2013–2023, 2002.

[25] E.D. Aydin, C.R.E de Oliveira, and A.J.H. Goddard. A finite element-spherical harmonics radiation transport model for photon migration in turbid media. *J Quant Spectrosc Radiat Transf*, 84:247–260, 2004.

[26] G. Bal. Inverse problems for homogeneous transport equations: I. The one-dimensional case. *Inv Probl*, 16:997–1011, 2000.

[27] G. Bal. Inverse problems for homogeneous transport equations: II. The multidimensional case. *Inv Probl*, 16:1013–1028, 2000.

[28] G. Bal. Particle transport through scattering regions with clear layers and inclusions. *J Comput Phys*, 180(2):659–685, 2002.

[29] G. Bal. Transport through diffusive and nondiffusive regions, embedded objects, and clear layers. *SIAM J Appl Math*, 62(5):1677–1697, 2002.

[30] G. Bal and Y. Maday. Coupling of transport and diffusion models in linear transport theory. *Math Model Numer Anal*, 36(1):69–86, 2002.

[31] G. Bal and K. Ren. Generalized diffusion model in optical tomography with clear layers. *J Opt Soc Am A*, 20(12):2355–2364, 2003.

[32] D.A. Benaron, D.C. Ho, S. Spilman, J.P. VanHouten, and D.K. Stevenson. Tomographic time-of-flight optical imaging device. In M.C. Hogan, D.C. Poole O. Mathieu-Costello, and P.D. Wagner, editors, *Oxygen Transport to Tissue XIV*, pages 207–214, Plenum Press, New York, 1994.

[33] D.A. Benaron, J.P. VanHouten, W.-F. Cheong, E.L. Kermit, and R.A. King. Early clinical results of time-of-flight optical tomography in a neonatal intensive care unit. In B. Chance and R.R. Alfano, editors, *Optical Tomography, Photon Migration, and Spectroscopy of Tissue and Model Media: Theory, Human Studies, and*

Instrumentation, volume 2389 of *Proc of SPIE*, pages 582–596, 1995.

[34] A.V. Bluestone, G. Abdoulaev, C.H. Schmitz, R.L. Barbour, and A.H. Hielscher. Three-dimensional optical tomography of hemodynamics in the human head. *Opt Express*, 9(6):272–286, 2001.

[35] A.Y. Bluestone, M. Stewart, J. Lasker, G.S. Abdoulaev, and A.H. Hielscher. Three-dimensional optical tomographic brain imaging in small animals, part 1: hypercapnia. *J Biomed Opt*, 9(5):1046–1062, 2004.

[36] A.Y. Bluestone, M. Stewart, B. Lei, I.S. Kass, J. Lasker, G.S. Abdoulaev, and A.H. Hielscher. Three-dimensional optical tomographic brain imaging in small animals, part 2: Unilateral carotid occlusion. *J Biomed Opt*, 9(5):1063–1073, 2004.

[37] D.A. Boas. *Diffuse Photon Probes of Structural and Dynamical Properties of Turbid Media: Theory and Biomedical Applications*. PhD thesis, University of Pennsylvania, Philadelphia, 1996.

[38] D.A. Boas, D.H. Brooks, E.L. Miller, C.A. DiMarzio, M. Kilmer, R.J. Gaudette, and Q. Zhang. Imaging the body with diffuse optical tomography. *IEEE Signal Process Mag*, 18(6):57–75, 2001.

[39] D.A. Boas, J.P. Culver, J.J. Stott, and A.K. Dunn. Three dimensional Monte Carlo code for photon migration through complex heterogeneous media including the adult human head. *Opt Express*, 10(3):159–170, 2002.

[40] D.A. Boas and A.M. Dale. Simulation study of magnetic resonance imaging-guided cortically constrained diffuse optical tomography of human brain function. *Appl Opt*, 44(10):1957–1968, 2005.

[41] D.A. Boas, A.M. Dale, and M.A. Franceschini. Diffuse optical imaging of brain activation: approaches to optimizing image sensitivity, resolution, and accuracy. *NeuroImage*, 23:S275–S288, 2004.

[42] D.A. Boas, M.A. Franceschini, A.K. Dunn, and G. Strangman. Noninvasive imaging of cerebral activation with diffuse optical tomography. In R. Frostig, editor, *In Vivo Optical Imaging of Brain Function*, chapter 8, CRC Press, Boca Raton, 2002.

[43] D.A. Boas, T. Gaudette, and S.R. Arridge. Simultaneous imaging and optode calibration with diffuse optical tomography. *Opt Express*, 8(5):263–270, 2001.

[44] D.A. Boas, T. Gaudette, G. Strangman, X. Cheng, J.J.A. Marota, and J.B. Mandeville. The accuracy of near infrared spectroscopy and imaging during focal changes in cerebral hemodynamics. *NeuroImage*, 13(1):76–90, 2001.

[45] E. Boman, J. Tervo, and M. Vauhkonen. Modelling the transport of ionizing radiation using the finite element method. *Phys Med Biol*, 50:265–280, 2005.

[46] G. Boverman, E.L. Miller, A. Li, Q. Zhang, T. Chaves, D.H. Brooks, and D.A. Boas. Quantitative spectroscopic diffuse optical tomography of the breast guided by imperfect *a priori* structural information. *Phys Med Biol*, 50:3941–3956, 2005.

[47] B. Brooksby, S. Jiang, H. Dehghani, B.W. Pogue, K.D. Paulsen, J. Weaver, C. Kogel, and S.P. Poplack. Combining near-infrared tomography and magnetic resonance imaging to study *in vivo* breast tissue: implementation of a Laplacian-type regularization to incorporate magnetic resonance structure. *J Biomed Opt*, 10(5):051504, 2005.

[48] B. Brooksby, S. Srinivasan, S. Jiang, H. Dehghani, B.W. Pogue, K.D. Paulsen, J. Weaver, C. Kogel, and S.P. Poplack. Spectral priors improve near-infrared diffuse tomography more than spatial priors. *Opt Lett*, 30(15):1968–1970, 2005.

[49] B.A. Brooksby, H. Dehghani, B.W. Pogue, and K.D. Paulsen. Near-infrared (NIR)

tomography breast image reconstruction with *a priori* structural information from MRI: algorithm development for reconstructing heterogeneities. *IEEE J Sel Topics Quantum Electron*, 9(2):199–209, 2003.

[50] K.M. Case and P.F. Zweifel. *Linear Transport Theory*. Addison-Wesley, Reading, 1967.

[51] C. Cercignani. *The Boltzmann Equation and Its Applications*. Springer-Verlag, New York, 1988.

[52] B. Chance, M. Cope, E. Gratton, N. Ramanujam, and B. Tromberg. Phase measurement of light absorption and scatter in human tissue. *Rev Sci Instrum*, 69(10):3457–3481, 1998.

[53] S. Chandrasekhar. *Radiative Transfer*. Oxford University Press, London, 1950.

[54] J. Chang, H.L. Graber, R.L. Barbour, and R. Aronson. Recovery of optical cross-section perturbations in dense-scattering media by transport-theory-based imaging operators and steady-state simulated data. *Appl Opt*, 35(20):3963–3978, 1996.

[55] W.-F. Cheong, S.A. Prahl, and A.J. Welch. A review of the optical properties of biological tissues. *IEEE J Quantum Electron*, 26(12):2166–2185, 1990.

[56] C. Cheung, J.P. Culver, K. Takahashi, J.H. Greenberg, and A.G. Yodh. *In vivo* cerebrovascular measurement combining diffuse near-infrared absorption and correlation spectroscopies. *Phys Med Biol*, 46:2053–2065, 2001.

[57] R. Choe, A. Corlu, K. Lee, T. Durduran, S.R. Arridge, B.J. Czerniecki, D.L. Fraker, A. DiMichele, B. Chance, M.A. Rosen, and A.G. Yodh. Diffuse optical tomography of breast cancer during neoadjuvant chemotherapy: A case study with comparison to MRI. *Med Phys*, 32(4):1128–1139, 2005.

[58] J.H. Choi, M. Wolf, V. Toronov, U. Wolf, C. Polzonetti, D. Hueber, L.P. Safonova, R. Gupta, A. Michalos, W. Mantulin, and E. Gratton. Noninvasive determination of the optical properties of adult brain: near-infrared spectroscopy approach. *J Biomed Opt*, 9(1):221–229, 2004.

[59] S.B. Colak, M.B. van der Mark, G.W.'t Hooft, J.H. Hoogenraad, E.S. van der Linden, and F.A. Kuijpers. Clinical optical tomography and NIR spectroscopy for breast cancer detection. *IEEE J Sel Topics Quantum Electron*, 5(4):1143–1158, 1999.

[60] D. Contini, F. Martelli, and G. Zaccanti. Photon migration through a turbid slab described by a model based on diffusion approximation. I. Theory. *Appl Opt*, 36(19):4587–4599, 1997.

[61] A. Corlu, R. Choe, T. Durduran, K. Lee, M. Schweiger, S.R. Arridge, E.M.C. Hillman, and A.G. Yodh. Diffuse optical tomography with spectral constraints and wavelength optimization. *Appl Opt*, 44(11):2082–2093, 2005.

[62] A. Corlu, T. Durduran, R. Choe, M. Schweiger, E.M.C. Hillman, S.R. Arridge, and A.G. Yodh. Uniqueness and wavelength optimization in continuous-wave multispectral diffuse optical tomography. *Opt Lett*, 28(23):2339–2341, 2003.

[63] J.P. Culver, R. Choe, M.J. Holboke, L. Zubkov, T. Durduran, A. Slemp, V. Ntziachristos, B. Chance, and A.G. Yodh. Three-dimensional diffuse optical tomography in the parallel plane transmission geometry: Evaluation of a hybrid frequency domain/continuous wave clinical system for breast imaging. *Med Phys*, 30(2):235–247, 2003.

[64] J.P. Culver, A.M. Siegel, J.J. Stott, and D.A. Boas. Volumetric diffuse optical tomography of brain activity. *Opt Lett*, 28(21):2061–2063, 2003.

[65] H. Dehghani, S.R. Arridge, M. Schweiger, and D.T. Delpy. Optical tomography in the presence of void regions. *J Opt Soc Am A*, 17(9):1659–1670, 2000.

[66] H. Dehghani, B. Brooksby, K. Vishwanath, B.W. Pogue, and K.D. Paulsen. The effects of internal refractive index variation in near-infrared optical tomography: a finite element modelling approach. *Phys Med Biol*, 48:2713–2727, 2003.

[67] H. Dehghani and D.T. Delpy. Linear single-step image reconstruction in the presence of nonscattering regions. *J Opt Soc Am A*, 19(6):1162–1171, 2002.

[68] D.T. Delpy, M. Cope, P. van der Zee, S. Arridge, S. Wray, and J. Wyatt. Estimation of optical pathlength through fissue from direct time of flight measurement. *Phys Med Biol*, 33(12):1433–1442, 1988.

[69] S.G. Diamond, T.J. Huppert, V. Kolehmainen, M.A. Franceschini, J.P. Kaipio, S.R. Arridge, and D.A. Boas. Dynamic physiological modeling for functional diffuse optical tomography. *NeuroImage*, 30:88–101, 2006.

[70] T. Dierkes, D. Grosenick, K.T. Moesta, M. Möller, P.M. Schlag, H. Rinneberg, and S. Arridge. Reconstruction of optical properties of phantom and breast lesion *in vivo* from paraxial scanning data. *Phys Med Biol*, 50:2519–2542, 2005.

[71] O. Dorn. A transport-backtransport method for optical tomography. *Inv Probl*, 14(5):1107–1130, 1998.

[72] O. Dorn. Scattering and absorption transport sensitivity functions for optical tomography. *Opt Express*, 7(13):492–506, 2000.

[73] J.J. Duderstadt and W.R. Martin. *Transport Theory*. John Wiley & Sons, New York, 1979.

[74] T. Durduran, R. Choe, J.P. Culver, L. Zubkov, M.J. Holboke, J. Gimmarco, B. Chance, and A.G. Yodh. Bulk optical properties of healthy female breast tissue. *Phys Med Biol*, 47:2847–2861, 2002.

[75] H. Eda, I. Oda, Y. Ito, Y. Wada, Y. Oikawa, Y. Tsunazawa, M. Takada, Y. Tsuchiya, Y. Yamashita, M. Oda, A. Sassaroli, Y. Yamada, and M. Tamura. Multichannel time-resolved optical tomographic imaging system. *Rev Sci Instrum*, 70(9):3595–3602, 1999.

[76] R. Elaloufi, R. Carminati, and J.-J. Greffet. Definition of the diffusion coefficient in scattering and absorbing media. *J Opt Soc Am A*, 20(4):678–1437, 2003.

[77] L.C. Enfield, A.P. Gibson, N.L. Everdell, D.T. Delpy, J.C. Hebden, S.R. Arridge, M. Douek, and M.R.S. Keshtgar. Three-dimensional time-resolved optical mammography of the uncompressed breast. In *Biomedial Optics 2006 Technical Digest*, SC4, Optical Society of America, Washington, DC, 2006.

[78] N.L. Everdell, A.P. Gibson, I.D.C. Tullis, T. Vaithianathan, J.C. Hebden, and D.T. Delpy. A frequency multiplexed near-infrared topography system for imaging functional activation in the brain. *Rev Sci Instrum*, 76:093705, 2005.

[79] S. Fantini, M.A. Franceschini, and E. Gratton. Effective source term in the diffusion equation for photon transport in turbid media. *Appl Opt*, 36(1):156–163, 1997.

[80] S. Fantini, S.A. Walker, M.A. Franceschini, M. Kaschke, P.M. Schlag, and K.T. Moesta. Assessment of the size, position and optical properties of breast tumors *in vivo* by noninvasive optical methods. *Appl Opt*, 37(10):1982–1989, 1998.

[81] G.W. Faris. Diffusion equation boundary conditions for the interface between turbid media: a comment. *J Opt Soc Am A*, 19(3):519–520, 2002.

[82] T.J. Farrell and M.S. Patterson. A diffusion theory model of spatially resolved, steady-state diffuse reflectance for the noninvasive determination of tissue optical properties *in vivo*. *Med Phys*, 19(4):879–888, 1992.

[83] H.A. Ferwerda. The radiative transfer equation for scattering media with a spatially varying refractive index. *J Opt A: Pure Appl Opt*, 1(3):L1–L2, 1999.

[84] M. Firbank, S.R. Arridge, M. Schweiger, and D.T. Delpy. An investigation of light

transport through scattering bodies with non-scattering regions. *Phys Med Biol*, 41:767–783, 1996.

[85] M.A. Franceschini, K.T. Moesta, S. Fantini, G. Gaida, E. Gratton, H. Jess, W.W. Mantulin, M. Seeber, P.M. Schlag, and M. Kaschke. Frequency-domain techniques enhance optical mammography: Initial clinical results. *Proc Natl Acad Sci USA*, 94(12):6468–6473, 1997.

[86] K. Furutsu. Diffusion equation derived from space-time transport equation. *J Opt Soc Am*, 70(4):360–366, 1980.

[87] A. Garofalakis, G. Zacharakis, G. Filippidis, E. Sanidas, D.D. Tsiftsis, V. Ntziachristos, T.G. Papazoglou, and J. Ripoll. Characterization of the reduced scattering coefficient for optically thin samples: theory and experiments. *J Opt A: Pure Appl Opt*, 6:725–735, 2004.

[88] R.J. Gaudette, D.H. Brooks, C.A. DiMarzio, M.E. Kilmer, E.L. Miller, T. Gaudette, and D.A. Boas. A comparison study of linear reconstruction techniques for diffuse optical tomographic imaging of absorption coefficient. *Phys Med Biol*, 45:1051–1070, 2000.

[89] A.P. Gibson, J.C. Hebden, and S.R. Arridge. Recent advances in diffuse optical imaging. *Phys Med Biol*, 50:R1–R43, 2005.

[90] A.P. Gibson, T. Austin, N.L. Everdell, M. Schweiger, S.R. Arridge, J.H. Meek, J.S. Wyatt, D.T. Delpy, and J.C. Hebden. Three-dimensional whole-head optical tomography of passive motor evoked responses in the neonate. *NeuroImage*, 30(2):521–528, 2006.

[91] A.P. Gibson, J. Riley, M. Schweiger, J.C. Hebden, S.R. Arridge, and D.T. Delpy. A method for generating patient-specific finite element meshes for head modelling. *Phys Med Biol*, 48:481–495, 2003.

[92] R.A.J. Groenhuis, H.A. Ferwerda, and J.J. Ten Bosch. Scattering and absorption of turbid materials determined from reflection measurements. part 1: Theory. *Appl Opt*, 22(16):2456–2462, 1983.

[93] D. Grosenick, K.T. Moesta, H. Wabnitz, J. Mucke, C. Stroszczynski, R. Macdonald, P.M. Schlag, and H. Rinneberg. Time-domain optical mammography: initial clinical results on detection and characterization of breast tumors. *Appl Opt*, 42(16):3170–3186, 2003.

[94] D. Grosenick, H. Wabnitz, K.T. Moesta, J. Mucke, M. Möller, C. Stroszczynski, J. Stößel, B. Wasserman, P.M. Schlag, and H. Rinneberg. Consentration and oxygen saturation of haemoglobin of 50 breast tumours determined by time-domain optical mammography. *Phys Med Biol*, 49:1165–1181, 2004.

[95] D. Grosenick, H. Wabnitz, H.H. Rinneberg, K.T. Moesta, and P.M. Schlag. Development of a time-domain optical mammograph and first *in vivo* applications. *Appl Opt*, 38(13):2927–2943, 1999.

[96] M. Guven, B. Yazici, X. Intes, and B. Chance. Diffuse optical tomography with *a priori* anatomical information. *Phys Med Biol*, 50:2837–2858, 2005.

[97] R.C. Haskell, L.O. Svaasand, T.-T. Tsay, T.-C. Feng, M.S. McAdams, and B.J. Tromberg. Boundary conditions for the diffusion equation in radiative transfer. *J Opt Soc Am A*, 11(10):2727–2741, 1994.

[98] T. Hayashi, Y. Kashio, and E. Okada. Hybrid Monte Carlo-diffusion method for light propagation in tissue with a low-scattering region. *Appl Opt*, 42(16):2888–2896, 2003.

[99] J.C. Hebden, S.R. Arridge, and D.T. Delpy. Optical imaging in medicine: I. Experimental techniques. *Phys Med Biol*, 42:825–840, 1997.

[100] J.C. Hebden, R.A. Kruger, and K.S. Wong. Time resolved imaging through a highly scattering medium. *Appl Opt*, 30(7):788–794, 1991.

[101] J.C. Hebden, T.D. Yates, A. Gibson, N. Everdell, S.R. Arridge, D.W. Chicken, M. Douek, and M.R.S. Keshtgar. Monitoring recovery after laser surgery of the breast with optical tomography: a case study. *Appl Opt*, 44(10):1898–1904, 2005.

[102] J.C. Hebden. Advances in optical imaging of the newborn infant brain. *Psychophysiology*, 40:501–510, 2003.

[103] J.C. Hebden, A. Gibson, T. Austin, R. Md Yusof, N. Everdell, D.T. Delpy, S.R. Arridge, J.H. Meek, and J.S. Wyatt. Imaging changes in blood volume and oxygenation in the newborn infant brain using three-dimensional optical tomography. *Phys Med Biol*, 49:1117–1130, 2004.

[104] J.C. Hebden, A. Gibson, R. Md Yusof, N. Everdell, E.M.C. Hillman, D.T. Delpy, S.R. Arridge, T. Austin, J.H. Meek, and J.S. Wyatt. Three-dimensional optical tomography of the premature infant brain. *Phys Med Biol*, 47:4155–4166, 2002.

[105] J. Heino, S. Arridge, J. Sikora, and E. Somersalo. Anisotropic effects in highly scattering media. *Phys Rev E*, 68:031908, 2003.

[106] J. Heino and E. Somersalo. Estimation of optical absorption in anisotropic background. *Inv Probl*, 18:559–573, 2002.

[107] J. Heino and E. Somersalo. A modelling error approach for the estimation of optical absorption in the presence of anisotropies. *Phys Med Biol*, 49:4785–4798, 2004.

[108] J. Heino, E. Somersalo, and J.P. Kaipio. Compensation for geometric mismodelling by anisotropies in optical tomography. *Opt Express*, 13(1):296–308, 2005.

[109] J. Heiskala, I. Nissilä, T. Neuvonen, S. Järvenpää, and E. Somersalo. Modeling anisotropic light propagation in a realistic model of the human head. *Appl Opt*, 44(11):2049–2057, 2005.

[110] L.G. Henyey and J.L. Greenstein. Diffuse radiation in the galaxy. *AstroPhys J*, 93:70–83, 1941.

[111] A.H. Hielscher, R.E. Alcouffe, and R.L. Barbour. Comparison of finite-difference transport and diffusion calculations for photon migration in homogeneous and heterogeneous tissues. *Phys Med Biol*, 43:1285–1302, 1998.

[112] A.H. Hielscher, S.L. Jacques, L. Wang, and F.K. Tittel. The influence of boundary conditions on the accuracy of diffusion theory in time resolved reflectance spectroscopy of biological tissues. *Phys Med Biol*, 40:1957–1975, 1995.

[113] A.H. Hielscher, A.D. Klose, and K.M. Hanson. Gradient-based iterative image reconstruction scheme for time-resolved optical tomography. *IEEE Trans Med Imaging*, 18(3):262–271, 1999.

[114] A.H. Hielscher, A.D. Klose, A.K. Scheel, B. Moa-Anderson, M. Backhaus, U. Netz, and J. Beuthan. Sagittal laser optical tomography for imaging of rheumatoid finger joints. *Phys Med Biol*, 49:1147–1163.

[115] E.M.C. Hillman, J.C. Hebden, F.E.W. Schmidt, S.R. Arridge, M. Schweiger, H. Dehghani, and D.T. Delpy. Calibration techniques and datatype extraction for time-resolved optical tomography. *Rev Sci Instrum*, 71(9):3415–3427, 2000.

[116] E.M.C. Hillman, J.C. Hebden, M. Schweiger, H. Dehghani, F.E.W. Schmidt, D.T. Delpy, and S.R. Arridge. Time resolved optical tomography of the human forearm. *Phys Med Biol*, 46:1117–1130, 2001.

[117] S.R. Hintz, D.A. Benaron, A.M. Siegel, A. Zourabian, D.K. Stevenson, and D.A. Boas. Bedside functional imaging of premature infant brain during passive motor activation. *J Perinat Med*, 29:335–343, 2001.

[118] M. Hiraoka, M. Firbank, M. Essenpreis, M. Cope, S.R. Arridge, P van der Zee, and D.T. Delpy. A Monte Carlo investigation of optical pathlength in inhomogeneous tissue and its application to near-infrared spectroscopy. *Phys Med Biol*, 38:1859–1876, 1993.

[119] Y. Hoshi. Functional near-infrared optical imaging: Utility and limitations in human brain mapping. *Psychophysiology*, 40:511–520, 2003.

[120] T.J. Huppert, S.G. Diamond, and D.A. Boas. Quantitative estimation of cerebral hemodynamic changes through the multimodality fusion of BOLD and diffuse optical tomography. In *Biomedial Optics 2006 Technical Digest*, SC8, Optical Society of America, Washington, DC, 2006.

[121] N. Hyvönen. Analysis of optical tomography with non-scattering regions. *Proceedings of the Edinburgh Mathematical Society*, 45:257–276, 2002.

[122] X. Intes, C. Maloux, M. Guven, B. Yazici, and B. Chance. Diffuse optical tomography with physiological and spatial *a priori* constraints. *Phys Med Biol*, 49:N155–N163, 2004.

[123] A. Ishimaru. *Wave Propagation and Scattering in Random Media*, volume 1. Academic Press, New York, 1978.

[124] H. Jiang. Optical image reconstruction based on the third-order diffusion equations. *Opt Express*, 4(8):241–246, 2001.

[125] S. Jiang, B.W. Pogue, T.O. McBride, M.M. Doyley, S.P. Poplack, and K.D. Paulsen. Near-infrared breast tomography calibration with optoelastic tissue simulating phantoms. *J Electron Imaging*, 12(4):613–620, 2003.

[126] S. Jiang, P.W. Pogue, K.D. Paulsen, C. Kogel, and S.P. Poplack. *In vivo* near-infrared spectral detection of pressure-induced changes in breast tissue. *Opt Lett*, 28(14):1212–1214, 2003.

[127] J. Kaipio and E. Somersalo. *Statistical and Computational Inverse Problems.* Springer, New York, 2005.

[128] J. Kaipio and E. Somersalo. Statistical inverse problems: discretization, model reduction and inverse crimes. *J Comput Appl Math*, In Press.

[129] M.H. Kalos and P.H. Whitlock. *Monte Carlo Methods.* John Wiley & Sons, New York, 1986.

[130] J.P. Kaltenbach and M. Kaschke. Frequency- and time-domain modelling of light transport in random media. In G. Muller, B. Chance, R. Alfano, S. Arridge, J. Beuthan, E. Gratton, M. Kaschke, B. Masters, S. Svanberg, and P. van der Zee, editors, *Medical Optical Tomography: Functional Imaging and Monitoring*, pages 65–86. SPIE, Bellingham, WA, 1993.

[131] G. Kanschat. A robust finite element discretization for radiative transfer problems with scattering. *East-West J Numer Math*, 6(4):265–272, 1998.

[132] M. Kataja, editor. *Multiphase Flows in Process Industry (ProMoni).* VTT research notes. VTT, Finland, 2005.

[133] M. Keijzer, W.M. Star, and P.R.M. Storchi. Optical diffusion in layered media. *Appl Opt*, 27(9):1820–1824, 1988.

[134] T. Khan and H. Jiang. A new diffusion approximation to the radiative transfer equation for scattering media with spatially varying refractive indices. *J Opt A: Pure Appl Opt*, 5:137–141, 2003.

[135] M.E. Kilmer, E.L. Miller, A. Barbaro, and D. Boas. Three-dimensional shape-based imaging of absorption perturbation for diffuse optical tomography. *Appl Opt*, 42(16):3129–3144, 2003.

[136] A.D. Kim and A. Ishimaru. Optical diffusion of continuos-wave, pulsed, and density

waves in scattering media and comparisons with radiative transfer. *Appl Opt*, 37(22):5313–5319, 1998.

[137] A.D. Kim. Light propagation in biological tissues containing an absorbing plate. *Appl Opt*, 43(3):555–563, 2004.

[138] A.D. Kim. Transport theory for light propagation in biological tissue. *J Opt Soc Am A*, 21(5):820–827, 2004.

[139] A.D. Kim and J.B. Keller. Light propagation in biological tissue. *J Opt Soc Am A*, 20(1):92–98, 2003.

[140] A.D. Klose and A.H. Hielscher. Iterative reconstruction scheme for optical tomography based on the equation of radiative transfer. *Med Phys*, 26(8):1698–1707, 1999.

[141] A.D. Klose and A. Hielscher. Optical tomography using the time-independent equation of radiative transfer – Part 2: inverse model. *J Quant Spectrosc Radiat Transf*, 72:715–732, 2002.

[142] A.D. Klose and A.H. Hielscher. Quasi-Newton methods in optical tomographic image reconstruction. *Inv Probl*, 19:387–409, 2003.

[143] A.D. Klose and E.W. Larsen. Simplified spherical harmonics methods for modeling light transport in biological tissue. In *Biomedial Optics 2006 Technical Digest*, MH3, Optical Society of America, Washington, DC, 2006.

[144] A.D. Klose, U. Netz, J. Beuthan, and A. Hielscher. Optical tomography using the time-independent equation of radiative transfer – Part 1: forward model. *J Quant Spectrosc Radiat Transf*, 72:691–713, 2002.

[145] V. Kolehmainen. *Novel Approaches to Image Reconstruction in Diffusion Tomography*. PhD thesis, University of Kuopio, Kuopio, Finland, 2001.

[146] V. Kolehmainen, S.R. Arridge, W.R.B. Lionheart, M. Vauhkonen, and J.P. Kaipio. Recovery of region boundaries of piecewise constant coefficients of an elliptic PDE from boundary data. *Inv Probl*, 15:1375–1391, 1999.

[147] V. Kolehmainen, S.R. Arridge, M. Vauhkonen, and J.P. Kaipio. Simultaneous reconstruction of internal tissue region boundaries and coefficients in optical diffusion tomography. *Phys Med Biol*, 45:3267–3283, 2000.

[148] V. Kolehmainen, S. Prince, S.R. Arridge, and J.P. Kaipio. State-estimation approach to the nonstationary optical tomography problem. *J Opt Soc Am A*, 20(5):876–889, 2003.

[149] V. Kolehmainen, M. Vauhkonen, J.P. Kaipio, and S.R. Arridge. Recovery of piecewise constant coefficients in optical diffusion tomography. *Opt Express*, 7(13):468–480, 2000.

[150] I.W. Kwee. *Towards a Bayesian Framework for Optical Tomography*. PhD thesis, University College London, London, UK, 1999.

[151] K.D. Lathrop. Ray effects in discrete ordinates equations. *Nucl Sci Eng*, 32:357–369, 1968.

[152] K.D. Lathrop. Remedies for ray effects. *Nucl Sci Eng*, 45:255–268, 1971.

[153] J.H. Lee, S. Kim, and Y.T. Kim. Finite element method for diffusive light propagations in index-mismatched media. *Opt Express*, 12(8):1727–1740, 2004.

[154] E.E. Lewis and W.F. Miller, Jr. *Computational Methods of Neutron Transport*. Wiley, New York, 1984.

[155] A. Li, G. Boverman, Y. Zhang, D. Brooks, E.L. Miller, M.E. Kilmer, Q. Zhang, E.M.C. Hillman, and D.A. Boas. Optimal linear inverse solution with multiple priors in diffuse optical tomography. *Appl Opt*, 44(10):1948–1956, 2005.

[156] A. Li, E.L. Miller, M.E. Kilmer, T.J. Brukilacchio, T. Chaves, J. Stott, Q. Zhang,

T. Wu, M. Chorlton, R.H. Moore, D.B. Kopans, and D.A. Boas. Tomographic optical breast imaging guided by three-dimensional mammography. *Appl Opt*, 42(25):5181–5190, 2003.

[157] A. Li, Q. Zhang, J.P. Culver, E.L. Miller, and D.A. Boas. Reconstructing chromosphere concentration images directly by continuous-wave diffuse optical tomography. *Opt Lett*, 29(3):256–258, 2004.

[158] C. Li and H. Jiang. A calibration method in diffuse optical tomography. *J Opt A: Pure Appl Opt*, 6:844–852, 2004.

[159] D.W. Marquardt. An algorithm for least-squares estimation of nonlinear parameters. *J SIAM*, 11(2):431–441, 1963.

[160] F. Martelli, A. Sassaroli, Y. Yamada, and G. Zaccanti. Analytical approximate solutions of the time-domain diffusion equation in layered slabs. *J Opt Soc Am A*, 19(1):71–80, 2002.

[161] L. Marti-Lopez, J. Bouza-Dominguez, J.C. Hebden, S.R. Arridge, and R.A. Martinez-Celorio. Validity conditions for the radiative transfer equation. *J Opt Soc Am A*, 20(11):2046–2056, 2003.

[162] S.J. Matcher. Nonuniqueness in optical tomography: relevance of the P1 approximation. *Opt Lett*, 24(23):1729–1731, 1999.

[163] T.O. McBride, B.W. Pogue, E.D. Gerety, S.B. Poplack, U.L. Österberg, and K.D. Paulsen. Spectroscopic diffuse optical tomography for the quantitative assesment of hemoglobin concentration and oxygen saturation in breast tissue. *Appl Opt*, 38(25):5480–5490, 1999.

[164] T.O. McBride, B.W. Pogue, S. Jiang, U.L. Österberg, and K.D. Paulsen. A parallel-detection frequency-domain near-infrared tomography system for hemoglobin imaging of the breast *in vivo*. *Rev Sci Instrum*, 72(3):1817–1824, 2001.

[165] T.O. McBride, B.W. Pogue, U.L. Österberg, and K.D. Paulsen. Strategies for absolute calibration of near infrared tomographic tissue imaging. In J.F. Dunn and H.M. Swartz, editors, *Oxygen Transport to Tissue XXIV*, pages 85–99, Kluwer Academic / Plenum Publishers, New York, 2003.

[166] A.B. Milstein, S. Oh, J.S. Reynolds, K.J. Webb, C.A. Bouman, and R.P. Millane. Three-dimensional Bayesian optical diffusion tomography with experimental data. *Opt Lett*, 27(2):95–97, 2002.

[167] J.E. Morel and J.M. McGhee. A self-adjoint angular flux equation. *Nucl Sci Eng*, 132(3):312–325, 1999.

[168] I. Nissilä, J.C. Hebden, D. Jennions, J. Heino, M. Schweiger, K. Kotilahti, T. Noponen, A. Gibson, S. Järvenpää, L. Lipiäinen, and T. Katila. A comparison between a time-domain and a frequency-domain system for optical tomography. *J Biomed Opt*, Accepted for publication.

[169] I. Nissilä, K. Kotilahti, K. Fallström, and T. Katila. Instrumentation for the accurate measurement of phase and amplitude in optical tomography. *Rev Sci Instrum*, 73(9):3306–3312, 2002.

[170] I. Nissilä, T. Noponen, K. Kotilahti, T. Tarvainen, M. Schweiger, L. Lipiäinen, S. Arridge, and T. Katila. Instrumentation and calibration methods for the multichannel measurement of phase and amplitude in optical tomography. *Rev Sci Instrum*, 76:044302, 2005.

[171] V. Ntziachristos, X. Ma, and B. Chance. Time-correlated single photon counting imager for simultaneous magnetic resonance and near-infrared mammography. *Rev Sci Instrum*, 69(12):4221–4233, 1998.

[172] S. Oh, A.B. Milstein, R.P. Millane, C.A. Bouman, and K.J. Webb. Source-detector

calibration in three-dimensional Bayesian optical diffusion tomography. *J Opt Soc Am A*, 19(10):1983–1993, 2002.

[173] E. Okada and D.T. Delpy. Near-infrared light propagation in an adult head model. I. Modeling of low-level scattering in the cerebrospinal fluid layer. *Appl Opt*, 42(16):2906–2914, 2003.

[174] E. Okada, M. Firbank, M. Schweiger, S.R. Arridge, M. Cope, and D.T. Delpy. Theoretical and experimental investigation of near-infrared light propagation in a model of the adult head. *Appl Opt*, 36(1):21–31, 1997.

[175] E. Okada, M. Schweiger, S.R. Arridge, M. Firbank, and D.T. Delpy. Experimental validation of Monte Carlo and finite-element methods for the estimation of the optical path length in inhomogeneous tissue. *Appl Opt*, 35(19):3362–3371, 1996.

[176] M.S. Patterson, B. Chance, and B.C. Wilson. Time resolved reflectance and transmittance for the non-invasive measurement of tissue optical properties. *Appl Opt*, 28(12):2331–2336, 1989.

[177] M.S. Patterson, B.C. Wilson, and D.R. Wyman. The propagation of optical radiation in tissue I. Models of radiation transport and their application. *Lasers Med Sci*, 6:155–168, 1991.

[178] M.S. Patterson, B.C. Wilson, and D.R. Wyman. The propagation of optical radiation in tissue. II: Optical properties of tissues and resulting fluence distributions. *Lasers Med Sci*, 6:379–390, 1991.

[179] K.D. Paulsen and H. Jiang. Spatially varying optical property reconstruction using a finite element diffusion equation approximation. *Med Phys*, 22(6):691–701, 1995.

[180] K.D. Paulsen and H. Jiang. Enhanced frequency-domain optical image reconstruction in tissues through total-variation minimization. *Appl Opt*, 35(19):3447–3458, 1996.

[181] Y. Pei, H.L. Graber, and R.L. Barbour. Influence of systematic errors in reference states on image quality and on stability of derived information for dc optical imaging. *Appl Opt*, 40(31):5755–5769, 2001.

[182] D. Piao, H. Dehghani, S. Jiang, S. Srinivasan, and B.W. Pogue. Instrumentation for video-rate near-infrared diffuse optical tomography. *Rev Sci Instrum*, 76:124301, 2005.

[183] A. Pifferi, P. Taroni, A. Torricelli, F. Messina, R. Cubeddu, and G. Danesini. Four-wavelength time-resolved optical mammography in the 680-980-nm range. *Opt Lett*, 28(13):1138–1140, 2003.

[184] A. Pifferi, A. Torricelli, A. Bassi, P. Taroni, R. Cubeddu, H. Wabnitz, D. Grosenick, M. Möller, R. Macdonald, J. Swartling, T. Svensson, S. Andersson-Engels, R.L.P. van Veen, H.J.C.M. Sterenborg, J.-M. Tualle, H. Lien Nghiem, S. Avrillier, M. Whelan, and H. Stamm. Performance assessment of photon migration instruments: MEDPHOT protocol. *Appl Opt*, 44(11):2104–2114, 2005.

[185] B.W. Pogue and K.D. Paulsen. High resolution near-infrared tomographic imaging simulations of the rat cranium by use of *a priori* magnetic resonance imaging structural information. *Opt Lett*, 23(21):1716–1718, 1998.

[186] B.W. Pogue, M. Testorf, T. McBride, U. Osterberg, and K.D. Paulsen. Instrumentation and design of a frequency-domain diffuse optical tomography imager for breast cancer detection. *Opt Express*, 1(13):391–403, 1997.

[187] B.W. Pogue, S. Jiang, H. Dehghani, C. Kogel, S. Soho, S. Srinivasan, X. Song, T.D. Tosteson, S.P. Poplack, and K.D. Paulsen. Characterization of hemoglobin, water, and NIR scattering in breast tissue: analysis of intersubject variability and menstrual cycle changes. *J Biomed Opt*, 9(3):541–552, 2004.

[188] S.A. Prahl, M. Keijzer, S.L. Jacques, and A.J. Welch. A Monte Carlo model of light propagation in tissue. In G.J. Müller and D.H. Sliney, editors, *SPIE Proceedings of Dosimetry of Laser Radiation in Medicine and Biology*, volume IS 5, pages 102–111, 1989.

[189] M. Premaratne, E. Premaratne, and A.J. Lowery. The photon transport equation for turbid biological media with spatially varying isotropic refractive index. *Opt Express*, 13(2):389–399, 2005.

[190] S. Prince, V. Kolehmainen, J.P. Kaipio, M.A. Franceschini, D. Boas, and S.R. Arridge. Time-series estimation of biological factors in optical diffusion tomography. *Phys Med Biol*, 48:1491–1504, 2003.

[191] K. Ren, G.S. Abdoulaev, G. Bal, and A.H. Hielscher. Algorithm for solving the equation of radiative transfer in the frequency domain. *Opt Lett*, 29(6):578–580, 2004.

[192] S. Richling, E. Meinköhn, N. Kryzhevoi, and G. Kanschat. Radiative transfer with finite elements I. Basic method and tests. *Astronomy & Astrophysics*, 380(2):776–788, 2001.

[193] J. Riley, H. Dehghani, M. Schweiger, S.R. Arridge, J. Ripoll, and M. Nieto-Vesperinas. 3D optical tomography in the presence of void regions. *Opt Express*, 7(13):462–467, 2000.

[194] J. Ripoll and M. Nieto-Vesperinas. Index mismatch for diffuse photon density waves at both flat and rough diffuse–diffuse interfaces. *J Opt Soc Am A*, 16(8):1947–1957, 1999.

[195] J. Ripoll, M. Nieto-Vesperinas, and S.R. Arridge. Effect of roughness in nondiffusive regions within diffusive media. *J Opt Soc Am A*, 18(4):940–947, 2001.

[196] J. Ripoll, M. Nieto-Vesperinas, S.R. Arridge, and H. Dehghani. Boundary conditions for light propagation in diffusive media with nonscattering regions. *J Opt Soc Am A*, 17(9):1671–1681, 2000.

[197] V.G. Romanov and S. He. Some uniqueness theorems for mammography-related time-domain inverse problems for the diffusion equation. *Inv Probl*, 16:447–459, 2000.

[198] A.K. Scheel, M. Backhaus, A.D. Klose, B. Moa-Anderson, U.J. Netz, K.-G.A. Hermann, J. Beuthan, G.A. Müller, G.R. Burmester, and A.H. Hielscher. First clinical evaluation of sagittal laser optical tomography for detection of synovitis in arthritic finger joints. *Ann Rheum Dis*, 64:239–245, 2005.

[199] F.E.W. Schmidt, M.E. Fry, E.M.C. Hillman, J.C. Hebden, and D.T. Delby. A 32-channel time-resolved instrument for medical optical tomography. *Rev Sci Instrum*, 71:256–265, 2000.

[200] J.M. Schmitt, G.X. Zhou, E.C. Walker, and R.T. Wall. Multilayer model of photon diffusion in skin. *J Opt Soc Am A*, 7(11):2141–2153, 1990.

[201] C.H. Schmitz, H.L. Graber, H. Luo, I. Arif, J. Hira, Y. Pei, A. Bluestone, S. Zhong, R. Andronica, I. Soller, N. Ramirez, S-L.S. Barbour, and R.L. Barbour. Instrumentation and calibration protocol for imaging dynamic features in dense-scattering media by optical tomography. *Appl Opt*, 39(34):6466–6486, 2000.

[202] C.H. Schmitz, D.P. Klemer, R. Hardin, M.S. Katz, Y. Pei, H.L. Graber, M.B. Levin, R.D. Levina, N.A. Franco, W.B. Solomon, and R.L. Barbour. Design and implementation of dynamic near-infrared optical tomographic imaging instrumentation for simultaneous dual-breast measurements. *Appl Opt*, 44(11):2140–2153, 2005.

[203] C.H. Schmitz, M. Löcker, J.M. Lasker, A.H. Hielscher, and R.L. Barbour. Instru-

mentation for fast functional optical tomography. *Rev Sci Instrum*, 73(2):429–439, 2002.

[204] M. Schweiger and S.R. Arridge. Direct calculation with a finite-element method of the Laplace transform of the distribution of photon time of flight in tissue. *Appl Opt*, 36(34):9042–9049, 1997.

[205] M. Schweiger and S.R. Arridge. Optimal data types in optical tomography. In *Information Processing in Medical Imaging (IPMI'97 Proceedings), Lecture Notes in Computer Science*, volume 1230, pages 71–84, Springer, 1997.

[206] M. Schweiger and S.R. Arridge. Application of temporal filters to time resolved data in optical tomography. *Phys Med Biol*, 44:1699–1717, 1999.

[207] M. Schweiger and S.R. Arridge. Optical tomographic reconstruction in a complex head model using *a priori* region boundary information. *Phys Med Biol*, 44:2703–2721, 1999.

[208] M. Schweiger, S.R. Arridge, and I. Nissilä. Gauss-Newton method for image reconstruction in diffuse optical tomography. *Phys Med Biol*, 50:2365–2386, 2005.

[209] M. Schweiger and S.R. Arridge. The finite-element method for the propagation of light in scattering media: Frequency domain case. *Med Phys*, 24(6):895–902, 1997.

[210] M. Schweiger, S.R. Arridge, O. Dorn, A. Zacharopoulos, and V. Kolehmainen. Reconstructing absorption and diffusion shape profiles in optical tomography by a level set technique. *Opt Lett*, 31(4):471–473, 2006.

[211] M. Schweiger, S.R. Arridge, M. Hiraoka, and D.T. Delpy. The finite element method for the propagation of light in scattering media: Boundary and source conditions. *Med Phys*, 22(11):1779–1792, 1995.

[212] M. Schweiger, A. Gibson, and S.R. Arridge. Computational aspects of diffuse optical tomography. *IEEE Comput Sci Eng*, 5(6):33–41, 2003.

[213] A.M. Siegel, J.P. Culver, J.B. Mandeville, and D.A. Boas. Temporal comparison of functional brain imaging with diffuse optical tomography and fMRI during rat forepaw stumulation. *Phys Med Biol*, 48:1391–1403, 2003.

[214] A.M. Siegel, J.J.A. Marota, and D.A. Boas. Design and evaluation of a continuous-wave diffuse optical tomography system. *Opt Express*, 4(8):287–298, 1999.

[215] L. Spinelli, A. Torricelli, A. Pifferi, P. Taroni, G. Danesini, and R. Cubeddu. Characterization of female breast lesions from multi-wavelength time-resolved optical mammography. *Phys Med Biol*, 50:2489–2502, 2005.

[216] T. Spott and L.O. Svaasand. Collimated light sources in the diffusion approximation. *Appl Opt*, 39(34):6453–6465, 2000.

[217] S. Srinivasan, B.W. Pogue, B. Brooksby, S. Jiang, H. Dehghani, C. Kogel, W.A. Wells, S.P. Poplack, and K.D. Paulsen. Near-infrared characterization of breast tumors *in vivo* using spectrally-constrained reconstrucion. *Technology in Cancer Research & Treatment*, 4(5):513–526, 2005.

[218] S. Srinivasan, B.W. Pogue, S. Jiang, H. Dehghani, C. Kogel, S. Soho, J.J. Gibson, T.D. Tosteson, S.P. Poplack, and K.D. Paulsen. Interpreting hemoglobin and water concentration, oxygen saturation, and scattering measured *in vivo* by near-infrared breast tomography. *Proc Natl Acad Sci USA*, 100(21):12349–12354, 2003.

[219] S. Srinivasan, B.W. Pogue, S. Jiang, H. Dehghani, C. Kogel, S. Soho, J.J. Gibson, T.D. Tosteson, S.P. Poplack, and K.D. Paulsen. In vivo hemoglobin and water concentrations, oxygen saturation, and scattering estimates from near-infrared breast tomography using spectral reconstrucion. *Acad Radiology*, 13(2):195–202, 2006.

[220] S. Srinivasan, B.W. Pogue, S. Jiang, H. Dehghani, and K.D. Paulsen. Spectrally constrained chromophore and scattering near-infrared tomography provides quan-

titative and robust reconstruction. *Appl Opt*, 44(10):1858–1869, 2005.

[221] J.J. Stott, J.P. Culver, S.R. Arridge, and D.A. Boas. Optode positional calibration in diffuse optical tomography. *Appl Opt*, 42(16):3154–3162, 2003.

[222] G. Strangman, D.A. Boas, and J.P. Sutton. Non-invasive neuroimaging using near-infrared light. *Biol Psychiatry*, 52:679–693, 2002.

[223] P. Taroni, A. Torricelli, L. Spinelli, A. Pifferi, F. Arpaia, G. Danesini, and R. Cubeddu. Time-resolved optical mammography between 637 and 685 nm: clinical study on the detection and identification of breast lesions. *Phys Med Biol*, 50:2469–2488, 2005.

[224] T. Tarvainen, V. Kolehmainen, M. Vauhkonen, A. Vanne, A.P. Gibson, M. Schweiger, S.R. Arridge, and J.P. Kaipio. Computational calibration method for optical tomography. *Appl Opt*, 44(10):1879–1888, 2005.

[225] T. Tarvainen, M. Vauhkonen, V. Kolehmainen, S.R. Arridge, and J.P. Kaipio. Coupled radiative transfer equation and diffusion approximation model for photon migration in turbid medium with low-scattering and non-scattering regions. *Phys Med Biol*, 50:4913–4930, 2005.

[226] T. Tarvainen, M. Vauhkonen, V. Kolehmainen, J. Heiskala, S.R. Arridge, and J.P. Kaipio. Modeling photon migration in tissues with the coupled radiative transfer equation and diffusion approximation. In *Biomedial Optics 2006 Technical Digest*, SH49, Optical Society of America, Washington, DC, 2006.

[227] T. Tarvainen, M. Vauhkonen, V. Kolehmainen, and J.P. Kaipio. Hybrid radiative–transfer–diffusion model for optical tomography. *Appl Opt*, 44(6):876–886, 2005.

[228] T. Tarvainen, M. Vauhkonen, V. Kolehmainen, and J.P. Kaipio. Finite element model for the coupled radiative transfer equation and diffusion approximation. *Int J Numer Meth Engng*, 65(3):383–405, 2006.

[229] J. Tervo, P. Kolmonen, M. Vauhkonen, L.M. Heikkinen, and J.P. Kaipio. A finite-element model of electron transport in radiation therapy and a related inverse problem. *Inv Probl*, 15:1345–1361, 1999.

[230] M. Testorf, U. Österberg, B. Pogue, and K. Paulsen. Sampling of time- and frequency-domain signals in Monte Carlo simulations of photon migration. *Appl Opt*, 38(1):236–245, 1999.

[231] M.D. Tidriri. An alternative model to boundary layers correctors in transport theory and radiative transfer. *C R Acad Sci Paris Série I*, 333:195–200, 2001.

[232] M.D. Tidriri. Analysis of the approximation of the coupling of transport equations and their diffusion approximations by the transmission time marching algorithm. *C R Acad Sci Paris Série I*, 333:301–306, 2001.

[233] H.C. van de Hulst. *Multiple Light Scattering: Tables, Formulas, and Applications.* Academic Press, New York, 1980.

[234] M. Vauhkonen, T. Tarvainen, V. Kolehmainen, and J.P. Kaipio. Finite element approximations for the radiative transfer equation. In *Biomedial Optics 2006 Technical Digest*, SH47, Optical Society of America, Washington, DC, 2006.

[235] P.J. Vauhkonen. *Image Reconstruction in Three-Dimensional Electrical Impedance Tomography.* PhD thesis, University of Kuopio, Kuopio, Finland, 2004.

[236] L. Wang and S.L. Jacques. Hybrid model of Monte Carlo simulation and diffusion theory for light reflectance by turbid media. *J Opt Soc Am A*, 10(8):1746–1752, 1993.

[237] L. Wang, S.L. Jacques, and L. Zheng. MCML – Monte Carlo modeling of light transport in multi-layered tissues. *Computer Methods and Programs in Biomedicine*, 47:131–146, 1995.

[238] L.V. Wang. Rapid modeling of diffuse reflectance of light in turbid slabs. *J Opt Soc Am A*, 15(4):936–944, 1998.

[239] R.A. Williams and M.S. Beck, editors. *Process Tomography, Principles, Techniques and Applications*. Butterworth-Heinemann Ltd, Oxford, 1995.

[240] S. Wright, M. Schweiger, and S.R. Arridge. Solutions to the transport equation using variable order angular basis. In K. Licha and R. Cubeddu, editors, *Photon Migration and Diffuse-Light Imaging II*, volume 5859 of *Proc of SPIE*, pages 160–167, 2005.

[241] Y. Xu, N. Iftimia, H. Jiang, L.L. Key, and M.B. Bolster. Imaging of in vitro and in vivo bones and joints with continous-wave diffuse optical tomography. *Opt Express*, 8(7):447–451, 2001.

[242] T. Yates, J.C. Habden, A. Gibson, N. Everdell, S.R. Arridge, and M. Douek. Optical tomography of the breast using a multi-channel time-resolved imager. *Phys Med Biol*, 50:2503–2517, 2005.

[243] T.D. Yates. *Time-resolved Optical Tomography for the Detection and Specification of Breast Disease*. PhD thesis, University College London, London, UK, 2005.

[244] T.D. Yates, J.C. Hebden, A.P. Gibson, L. Enfield, N.L. Everdell, S.R. Arridge, and D.T. Delpy. Time-resolved optical mammography using liquid coupled interface. *J Biomed Opt*, 10(5):054011, 2005.

[245] J.C. Ye, K.J. Webb, C.A. Bouman, and R.P. Millane. Optical diffusion tomography by iterative-coordinate-descent optimization in a Bayesian framework. *J Opt Soc Am A*, 16(10):2400–2412, 1999.

[246] J.C. Ye, C.A. Bouman, K.J. Webb, and R.P. Millane. Nonlinear multigrid algorithms for Bayesian optical diffusion tomography. *IEEE Trans Image Processing*, 10(5):909–922, 2001.

[247] X. Zhang, V.Y. Toronov, and A.G. Webb. Simultaneous integrated diffuse optical tomography and functional magnetic resonance imaging of the human brain. *Opt Express*, 13(14):5513–5521, 2005.

Kuopio University Publications C. Natural and Environmental Sciences

C 185. Luomala, Eeva-Maria. Photosynthesis, chemical composition and anatomy of Scots pine and Norway spruce needles under elevated atmospheric CO2 concentration and temperature.
2005. 137 p. Acad. Diss.

C 186. Heikkinen, Lasse M. Statistical estimation methods for electrical pricess tomography.
2005. 147 p. Acad. Diss.

C 187. Riihinen, Kaisu. Phenolic compounds in berries.
2005. 97 p. Acad. Diss.

C 188. Virkutyte, Jurate. Heavy metal bonding and remediation conditions in electrokinetically treated waste medias.
2005. 133 p. Acad. Diss.

C 189. Koistinen, Kaisa. Birch PR-10c: multifunctional binding protein.
2006. 79 p. Acad. Diss.

C 190. Airaksinen, Sanna. Bedding and manure management in horse stables: its effect on stable air quality, paddock hygiene and the compostability and utilization of manure.
2006. 91 p. Acad. Diss.

C 191. Asikainen, Arja. Use of computational tools for rapid sorting and prioritising of organic compounds causing environmental risk with estrogenic and cytochrome P450 activity.
2006. 51 p. Acad. Diss.

C 192. Ålander, Timo. Carbon composition and volatility characteristics of the aerosol particles formed in internal combustion engines.
2006. 54 p. Acad. Diss.

C 193. Molnár, Ferdinand. Structural analysis of the ligand-binding domains of human and mouse CAR, human VDR and human PPARs.
2006. 115 p. Acad. Diss.

C 194. Kasurinen, Anne. Soil-related processes of young silver birch trees grown under elevated CO_2 and O_3 .
2006. 64 p. Acad. Diss.

C 195. Metsärinne, Sirpa. Degradiation of Novel and Conventional Complexing Agents.
2006. 138 p. Acad. Diss.

C 196. Heijari, Juha. Seed origin, forest fertilization and chemical elicitor influencing wood characteristics and biotic resistance of scots pine.
2006. 39 p. Acad. Diss.

C 197. Hakulinen, Mikko. Prediction of density, structure and mechanical properties of trabecular bone using ultrasound and X-ray techniques.
2006. 84 p. Acad. Diss.

C 198. Al Natsheh, Anas. Quantum Mechanics Study of Molecular Clusters Composed of Atmospheric Nucleation Precursors.
2006. 55 p. Acad. Diss.